AMERICAN UNIVERSITY OF BEIRUT

Tuning the Size, Morphology, and Composition of ZIF-8 and Co-doped ZIF-8 Crystals Through the Application of an Electric Field in a Reaction-Diffusion Framework

by
NOURA GEORGES RAHBANI

A thesis
submitted in partial fulfillment of the requirements
for the degree of Master of Science
to the Department of Chemistry
of the Faculty of Arts and Sciences
at the American University of Beirut

Beirut, Lebanon
October 2019

AMERICAN UNIVERSITY OF BEIRUT

Tuning the Size, Morphology, and Composition of ZIF-8 and Co-doped ZIF-8 Crystals Through the Application of an Electric Field in a Reaction-Diffusion Framework

by

NOURA GEORGES RAHBANI

Approved by:

On behalf of Dr. Ghoul

Dr. Mazen Al-Ghoul, Professor — Advisor

Chemistry

Dr. Houssam El-Rassy, Associate Professor — Member of Committee

Chemistry

Digambara Patra

Dr. Digambara Patra, Associate Professor — Member of Committee

Chemistry

Date of thesis defense: October 8, 2019

AMERICAN UNIVERSITY OF BEIRUT

THESIS, DISSERTATION, PROJECT RELEASE FORM

Student Name: Rahbani Noura Georges
Last First Middle

● Master's Thesis ○ Master's Project ○ Doctoral Dissertation

☐ I authorize the American University of Beirut to: (a) reproduce hard or electronic copies of my thesis, dissertation, or project; (b) include such copies in the archives and digital repositories of the University; and (c) make freely available such copies to third parties for research or educational purposes.

☑ I authorize the American University of Beirut, to: (a) reproduce hard or electronic copies of it; (b) include such copies in the archives and digital repositories of the University; and (c) make freely available such copies to third parties for research or educational purposes after:

One ___ year from the date of submission of my thesis , dissertation or project.
Two ___ years from the date of submission of my thesis , dissertation or project.
Three ✓__ years from the date of submission of my thesis , dissertation or project.

Nour Rahbani 10-10-2019
Signature Date

Acknowledgements

I would like to express my sincere gratitude to my supervisor, Dr. Mazen Al-Ghoul, for the support and guidance throughout this work, and for the much-needed humor since I joined the lab.

I would also like to extend my gratitude to my thesis committee members Dr. Houssam El-Rassy and Dr. Digambara Patra, for their helpful input and discussions during the pre-defense stage, and for their feedback.

I thank the Central Research Science Laboratory (CRSL) manager Ms. Rania Shatila for the training and never-ending help, and the staff at the chemistry department at AUB.

A big thank you to Ms. Manal Ammar for her assistance from day one, and for adding a particular element of fun to every job that must be done. I also thank my lab-mates, Rita, Salah, Mohammad, Fayrouz, Antranik, Razan, and Mahmoud for the helpful discussions and for their company, and all my friends in and out of AUB that shared these past years with me, creating great memories.

Last but not least, I am grateful for my parents and sister, who give me strength through their unconditional love and support.

An Abstract of the Thesis of

Noura Georges Rahbani for Master of Science
Major: Chemistry

Title: Tuning the Size, Morphology, and Composition of ZIF-8 and Co-doped ZIF-8 Crystals Through the Application of an Electric Field in a Reaction-Diffusion Framework.

Recently in our lab, some metal-organic frameworks (MOFs) and zeolitic imidazolate frameworks (ZIFs) were successfully synthesized at room temperature through the reaction-diffusion framework (RDF) in a hydrogel medium. We propose a development of this technique through the application of an electric field during ZIF crystal formation to further control size, morphology, and dopant incorporation. We use a 2-D circular reactor and circular tungsten electrodes to apply potential differences in the range of ± 2.0 V to a ZIF-8 system in agar gel throughout the course of precipitation. All solids are collected and characterized using scanning electron microscopy (SEM) and powder X-ray diffraction (PXRD). Doped samples are also characterized using energy-dispersive X-ray (EDX) analysis. Our study shows that the effect of the external electric field on the size and morphology of the ZIF-8 particles depends on the nature of the metal salts used. Applying a positive field reduces the size of the particles in the sulfate salt system, and leaves the nitrate system unaffected while applying a negative field increases the size and enhances the morphology of the particles in the nitrate system, while leaving the sulfate system unaffected. In both systems, the application of a negative filed induces the formation of an unidentified spherical co-precipitate in areas close to the diffusion front. Similar trends are observed in a Zn-Co mixed-metal ZIF-8 system. The application of an external field also affects the extent of cobalt incorporation into the ZIF-8 framework in both sulfate and nitrate salt systems; the application of a negative field encourages the cobalt incorporation, and the positive field drives cobalt out of the framework.

Contents

List of Figures

List of Tables

Chapter 1

Introduction

1.1 Reaction-Diffusion Frameworks (RDF)

1.1.1 Introduction

Chemical reactions with nonlinear dynamics are known to display spatiotemporal phenomena, like chaotic changes in concentration, traveling chemical waves, and stationary precipitation patterns [1]. Such dynamical phenomena usually occur in open systems that are far from equilibrium and are thus governed by the laws of non-equilibrium thermodynamics [2]. Although such happenings were met with skepticism from the scientific community when they first appeared at the end of the 19^{th} century, several nonlinear phenomena in chemical systems provide analogs of behaviors found in biological systems. The non-trivial behaviors of nonlinear systems include multistability - when two stable steady states coexist over a range of operating conditions, oscillatory reactions - the most famous of which is the Belousov-Zhabotinsky reaction, chemical chaos, chemical waves and propagating fronts - like reaction-diffusion systems, and pattern formation.

Reaction-diffusion systems are the result of the spatial coupling of local reaction processes with the diffusion transport of the reactants [2]. In a typical experiment, one chemical reactant is dissolved in a gel matrix (inner electrolyte), and the second reactant (outer electrolyte) is poured over the gel in the form of a highly concentrated electrolyte. The imposed concentration gradient drives the diffusion of the outer electrolyte into the gel medium, where it will react with the inner electrolyte. The propagating front in a reaction-diffusion system often results in the formation of spatiotemporal patterns [3]. The patterns form only over a narrow range of concentrations; the concentration of the outer electrolyte should be higher than that of the inner by several magnitudes. If the inner to outer ratio is too high the diffusion of the outer is hindered, and if the ratio is

too low the precipitation becomes continuous [4].

The first precipitation patterns were observed by R.E. Liesegang in 1896 [5] during his research on chemical reactions in gelatin when he accidentally dropped a solution of silver nitrate on a thin layer of gelatin that contains potassium dichromate. The silver dichromate that formed did not precipitate continuously but in a series of concentric rings separated by clear areas of gel, Figure 1.1. Liesegang also noted that the precipitation pattern forms as separated disks, or bands, that are perpendicular to the axis of the diffusion if the same reaction is performed in a test tube instead of a dish. The spacial periodicity could not be explained using the mechanism of a chemical reaction, and Liesegang was unable to explain the origin of the banding. These patterns were termed "Liesegang bands" by Ostwald [6], who was the first to offer a theory explaining the phenomenon shortly after Liesegang's initial publication, see section 1.1.3.

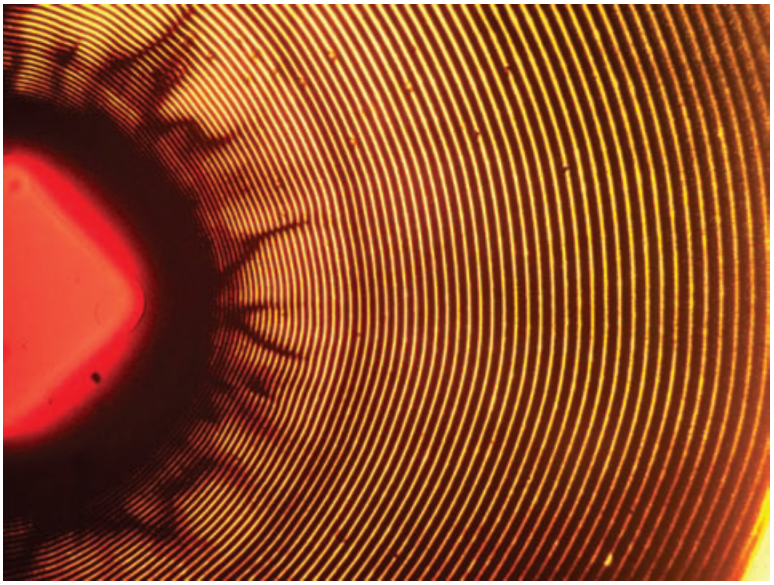

Figure 1.1: Concentric rings of silver dichromate in gelatin from a typical Liesegang system. From [7]

Since its discovery, periodic precipitation has been observed in a vast number of chemical systems, and it has been postulated that the spatiotemporal patterns could appear in any precipitation reaction under the proper conditions [4]. As early as 1910 the first record of reactions that form precipitation patterns was published by Le Duc [8]. The formation of these patterns aroused the interest of scientists across the fields of chemistry, physics, biology, mathematics, and engineering due to their ability to recreate patterns found in nature [9], like patterns on animal coats, seashells, limestone, agate rocks, bacterial colony growth, and others, Figure 1.2. The structure of the precipitation patterns varies from microscopic to macro-sale, and could occur in modified forms like microbanding,

Saturn-rings, and spirals [4].

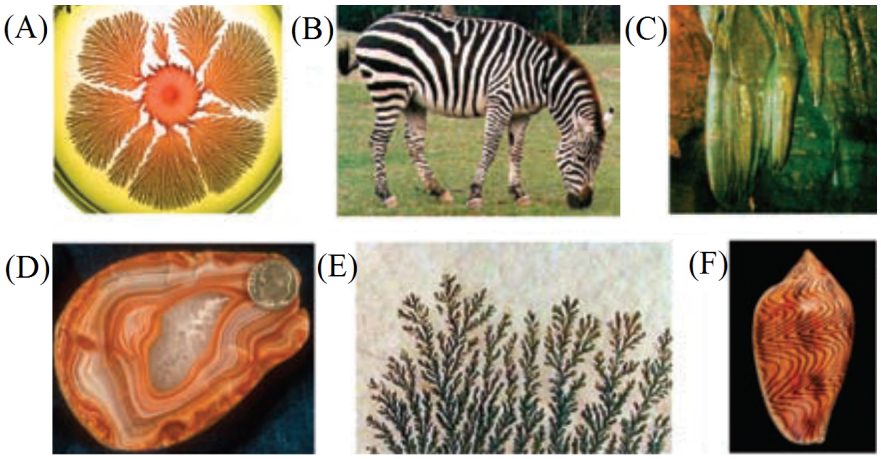

Figure 1.2: Examples of reaction-diffusion systems found in nature include: (A) bacterial colony growth, (B) patterns on a zebra's coat, (C) cave stalactites, (D) patterns in a polished cross section of agate, (E) dendridic formations in limestone, and (F) patterns on sea shells. Adapted from [7]

Although Liesegang patterns have been known for over a century, they are only currently starting to get incorporated into modern technology, as previous studies focused on characterizing and explaining the phenomena [7]. Moreover, there is still disagreement around the mechanism that governs the phenomenon. Many different theories have been proposed but none could be applied to all the observed non-conventional pattern phenomena [3]. However, it has been empirically established that all periodic precipitation phenomena follow a restricted set of generic laws known as scaling laws.

1.1.2 Scaling Laws of Periodic Precipitation

The Liesegang banding phenomenon has been found to follow empirical laws that govern the spatiotemporal patterns, known as scaling laws. The four main laws are the spacing law, Matalon-Pacter law, width law, and time law.

Spacing Law

The spacing law was first described by Jablczynski in 1923 [10] and states that the ratio of the positions of two adjacent bands is always constant. The band positions form a geometrical series of the form:

$$\frac{x_{n+1}}{x_n} = r \tag{1.1}$$

Where x_{n+1} and x_n are the positions of two consecutive bands, and the constant $r = 1 + p$. p is defined as the spacing coefficient and ranges from 0.05 to 0.4 [3]. This is the simplest form of the spacing law and only applies to systems with direct or normal spacing, meaning that the spacing between the bands increases as the bands get further from the diffusion interface. The law was later modified by Mathur in the 1960s [11] to include the systems with revert spacing, where the bands get closer as their distance from the interface increases.

Matalon-Packter Law

In the 1950s Matalon and Packter [12] noted that the spacing coefficient, p, for a given system depends on the concentrations of the inner and outer electrolytes as follows:

$$p = F(b_0) + \frac{G(b_0)}{a_0} \tag{1.2}$$

where a_0 and b_0 are the outer and inner electrolyte concentrations, respectively, and F and G are functions of b_0.

Width Law

The third scaling law that is generally observed in experiments with direct spacing is the width law [13]. It states that the width w_n of the bands increases with their distance from the interface x_n as a power law:

$$w_n \sim x_n^{\alpha} \tag{1.3}$$

which could be rearranged into:

$$ln(w_n) = \alpha ln(x_n) \tag{1.4}$$

where α is defined as the width exponent and is greater than one. The width law is not as popular as the other scaling laws and has been largely ignored in quantitative discussions due to the errors in measurements of w_n and the debate on its exact definition [3].

Time Law

The fourth empirical law was first described by Morse and Pierce [14] in the early 1990s and relates the position of a band to the time of its formation:

$$x_n = \alpha t_n^{1/2} + \beta \tag{1.5}$$

where α and β are constants. This mathematical statement follows directly from the diffusion-controlled nature of the phenomenon, which is evident in the dependence on $t^{1/2}$.

1.1.3 Theories Explaining Liesegang Phenomena

Many theories were proposed to describe the periodic precipitation phenomenon, but a comprehensive model that could explain all possible occurrences is yet to be presented. The theories could be pooled into two main groups: pre-nucleation theories explain the patterns as a result of a supersaturation wave that leads to precipitation, and are based on Ostwald's supersaturation theory, and post-nucleation theories based on Ostwald ripening and growth. The three most basic theories are the supersaturation theory, the competitive particle growth model, and the nucleation and growth model.

Pre-Nucleation Theory

The first theory investigating periodic precipitation was proposed by Ostwald [6] shortly after the publication of Liesegang's initial paper [5]. It is based on Ostwald's supersaturation theory and describes the banding as spatially discontinuous nucleation. Assuming a reaction ($A+B \rightarrow C$) where the outer electrolyte (A) diffuses into the gel containing the inner electrolyte (B), Ostwald's theory proposes that the product (C) does not directly form a precipitate but remains in supersaturated solution. At a certain position (x), the nucleation of the precipitate is only initiated when the local concentration product of the reactants is greater than the solubility product (K_{sp}), also known as the nucleation threshold of precipitation (q^*):

$$a(x,t) \cdot b(x,t) > q^* \tag{1.6}$$

The nucleation and aggregation will deplete the electrolytes A and B from the surroundings, which leads to a drop in the local concentration product and suppresses the nucleation. This results in the formation of a precipitate-free zone around the precipitated area. The diffusion of A continues until the concentration product surpasses the threshold value and the process is repeated. As diffusion proceeds, the outer electrolyte A becomes more dilute, and the repetition of the Ostwald supersaturation-nucleation-depletion cycle leads to the formation of rings of precipitate with direct spacing.

The first calculations supporting Ostwald's supersaturation theory were presented in 1950 by Wagner [15], who was able to reproduce the spacing law, eq. (1.1). The first mathematical formulation accompanied by semi-analytical investigations were performed by Prager [16] later in the decade, and were reformulated by Zeldovich [17] and more recently by Antal and Rácz [3].

Irrespective of the theory used, the development of Liesegang rings can be

described by a set of equations which combine Fick's second law of diffusion with the rate law [18], with the form:

$$\frac{\partial c_i(x,y,z)}{\partial t} = D_i \nabla^2 c_i + R(c_i) \tag{1.7}$$

where c_i is the concentration of species i with constant diffusion coefficient D_i, and $\mathrm{R}(c_i)$ describes the local reaction kinetics. The simplest evolution formulas describing reaction-diffusion use the supersaturation assumption in 1-dimension, and are given by:

$$\frac{\partial a}{\partial t} = D_a \frac{\partial^2 u}{\partial x^2} - k\theta\left(ab - q^*\right) - \lambda abd \tag{1.8}$$

$$\frac{\partial b}{\partial t} = D_b \frac{\partial^2 u}{\partial x^2} - k\theta\left(ab - q^*\right) - \lambda abd \tag{1.9}$$

$$\frac{\partial p}{\partial t} = k\theta\left(ab - q^*\right) + \lambda abd \tag{1.10}$$

where D_a and D_b are the diffusion constants of A and B that are assumed to be independent of concentration, θ is the step function describing an infinitely sharp threshold for precipitation, and k is the rate constant of precipitation. The last terms on the right describe the aggregation onto existing precipitate, where λ is the rate constant of aggregation, and $d(x,t)$ the concentration of the precipitate.

This results in the following concentration profiles:

$$a(x,t) = a_0\left(1 - \frac{x}{\sqrt{2D_a t}}\right) \tag{1.11}$$

$$b(x,t) = \frac{b_0}{\sqrt{2D_b\left(t - t_n\right)}}\left(x - x_n\right) \tag{1.12}$$

where x_n is the position of the band n, and t_n is the time required for its appearance. Figure 1.3 represents a simulation of the concentration profiles of a and b, and their concentration product after the appearance of a band n.

While the supersaturation model seems to describe the periodic precipitation process and explains the spacing law, it is unable to account for anomalies like secondary banding [19] or revert spacing [20].

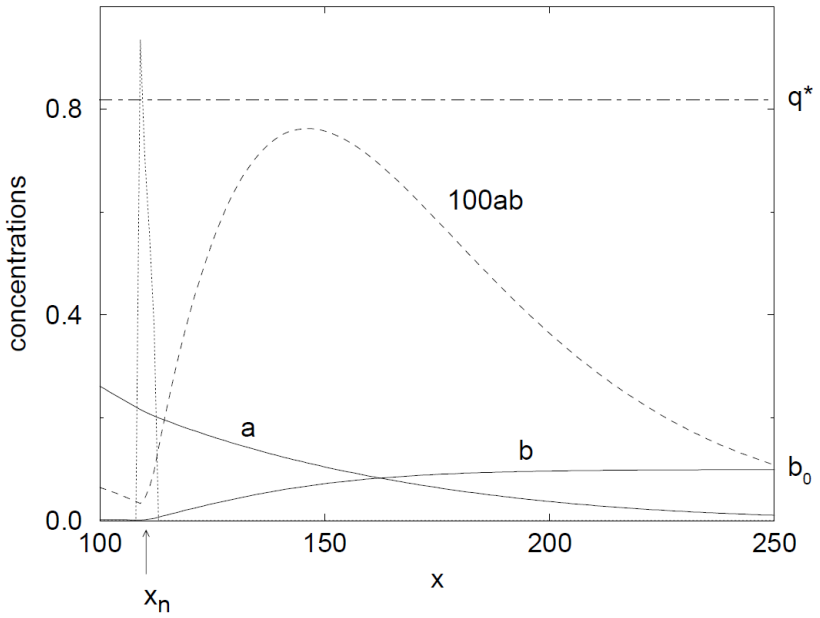

Figure 1.3: Computational simulation of the concentration profiles of the reactants and their concentration product after the formation of band n and before the formation of band $n+1$, calculated using the supersaturation model [3].

Post-Nucleation Theories

The common ground in all post-nucleation mechanisms is the assumption that the first step in a reaction-diffusion process is the formation of a homogeneous sol of solid particles. When the stability of the sol is disturbed, a visible precipitate emerges and a focusing mechanism forms a regular pattern. This could explain experimental findings where precipitation patterns occur in the absence of a concentration gradient [21, 22].

The first model based on chemical instability is the Competitive Particle Growth (CPG) model [23]. This model suggests that the sol that forms during the RD process evolves through Ostwald ripening, where large particles grow at the expense of smaller ones. The non-homogeneous size distribution of the sol particles causes a thermodynamic instability in the system since smaller particles have higher surface energy which increases their solubility. The small particles dissolve and diffuse towards the larger ones; this will result in a final system of fewer but larger particles. When the smaller particles completely dissolve, the large particles aggregate *via* a focusing mechanism forming bands with clear regions in between [24].

The second post-nucleation model is the theory of Nucleation and Growth [3, 7, 25], which combines the supersaturation theory with the CPG model. *A*

diffuses into the gel containing the inner electrolyte B and accumulates until the concentration product of the two reactants $a(x,t).b(x,t)$ exceeds the precipitation product K_{sp} at a location x, at which point homogeneous colloidal particles C start to form. This intermediate is free to move by diffusion until nucleation starts when the local concentration reaches a nucleation threshold value c^*. The formation of C nuclei will deplete the region from both A and B and nucleation will stop as their concentration product drops below c^*. The C product will grow on the present nuclei and their size will increase, aggregating into an immobile precipitate P as long as the concentration product is greater than the threshold for droplet growth p^*. When the local concentration product drops below p^*, the precipitate will start to dissolve.

Diffusion continues during this process, and both A and B are being transported towards or away from x. If their influx towards x is insufficient to maintain a steady-state, the concentration product will drop to become less than p^*. When C starts to dissolve, the concentration product will rise again, and growth continues. However, this process will not only deplete A and B from x but from neighboring locations as well. These starved regions will have a lower chance of nucleation and may become free of precipitate. At some distance from x, local concentrations could become large enough again to re-initiate precipitation, forming Liesegang rings. The rings could be widely spaced or unresolved, as the case with continuous precipitation.

Polezhaev and Müller [26, 27] built on this model and were able to use it in 1-D and 2-D systems to explain the formation of experimental patterns like radial dislocations in a petri dish [28], spirals [29], and Saturn-rings in test tubes [16].

1.1.4 Effect of External Electric Fields on RD Frameworks

It is known that experimental conditions like the gel used, the gel concentration, electrolyte concentrations, and temperature could be used to affect the patterns that form in a given RD system [4, 30, 31]. For example, the concentrations and the temperature affect the shape of the pattern [32, 12, 33], and changing the gel medium could enhance or hinder the formation of the precipitation pattern [31, 34]. Studies have also shown that the application of an external electric field affects the motion of the propagating fronts and spatial distribution of the precipitation pattern [35, 36, 37, 38, 39]. RD systems usually consist of reactions of ionic species, and when an electric field is imposed on the system both migration and diffusion play a role in mass transport.

Bena et. *al* [40] established that the distance between the bands in the pattern is influenced by both the intensity and the direction of the applied field. They found that the width of consecutive bands increases when the electric field drives

the reagents towards the reaction zone and might reach a stage of continuous precipitation. They also found that the separation between the bands becomes finer with the application of a reversed field. Sultan and Halabieh [41] showed that a positive field applied to the $Co(OH)_2$ system accelerates the front and increases the band spacing. A computational study performed by Al-Ghoul et *al.* [42] showed that, in line with the experimental results, the electric field causes faster propagation and greater spacing between the bands in a $Co(OH)_2$ system. The simulations also showed that the magnitude of the electric field could play a role in the observed trend, as two opposing effects were observed for the $Cr(OH)_3$ system: slower propagation with increasing field strength at high fields, and faster propagation with increasing field strength at sufficiently low fields. An external electric field could also affect the formation of the precipitate and not just the precipitation pattern. For examplem the application of a reverse electric field to the HgI_2 system decreases the velocity of propagation and hinders the formation of the yellow precipitate [43].

As previously mentioned, the reaction-diffusion equation is a combination of Fick‘s second law and the rate law. When an external electric field is imposed, and c_i carries a charge $z_i e$, a total current density equal to the sum of the diffusion and field components would be created [25]:

$$J_i = J_{D_i} + J_{EF} \tag{1.13}$$

$$J_i = z_i e D_i \nabla c_i + z_i e \mu_i c_i \cdot E \tag{1.14}$$

where μ_i is the electrical mobility of species i. As we are interested in particle flux, the reaction-diffusion equation in the presence of an electric field becomes:

$$\frac{\partial c_i}{\partial t} = D_i \nabla^2 c_i + z_i e \mu_i c_i \nabla E + z_i e \mu_i E \nabla c_i + R(c_i) \tag{1.15}$$

The electric field has two components: the first is due to the varying local concentrations of the species which change the local charge density, the second is due to the imposed potential difference applied to the system through the two ring electrodes. If the second component outweighs the first, E is considered constant and the second term in the above equation could be removed. If the two components are comparable, E is a variable that could be found through relating the local charge density to the local field gradient by solving Poisson‘s equation: [44]:

$$\nabla^2 \varphi = -\nabla \cdot E = \frac{-\rho}{\varepsilon_0 \varepsilon_r} \tag{1.16}$$

where φ is the electric potential, ρ is the charge density, and ε_r is the relative permittivity of the gel. Poisson‘s equation implies that the condition of electroneutrality must be globally satisfied in the gel matrix, and is given by:

$$\Sigma_i \left(z_i e c_i \right) = 0 \tag{1.17}$$

where species i of concentration c_i carries a charge of $z_i e$.

1.2 Zeolitic Imidazolate Frameworks (ZIF)

1.2.1 Introduction

Synthetic porous materials have been widely used in practical applications like gas adsorption, storage, separation, catalysis, and sensing, due to their versatile properties like high surface areas and tunable pore volumes [45, 46, 47]. They are defined as solid structures containing pores and voids [48] and traditionally fall into three categories: microporous, having pores with dimensions less than 2 nm, mesoporous, having a pore size from 2 to 50 nm, and macroporous, having pore size greater than 50 nm. Metal-organic frameworks (MOFs) are a relatively new subclass of porous materials that were introduced in the late 1990s by Robson [49, 50], Kitagawa [51, 52], Yaghi [53], Lee and Moore [54] and Férey [55]. MOF lattices are built of inorganic secondary building units (SBU) bridged by organic ligands, or linkers. The inorganic SBUs could be transition metal cations, rare-earth metals, p-block metals, or hybrids of metals and inorganic anions [56]. The wide range of inorganic and organic starting materials and the ability to use building units with well-defined geometries lend themselves to the versatility of MOF architecture. MOFs are known for their high thermal stability, uniform structure and high surface area [57, 58, 59, 60].

Zeolitic imidazolate frameworks (ZIFs) are a subclass of MOFs that are composed of tetrahedral (Td) transition metal ions linked by imidazolate ligands through their nitrogen atoms. The resulting metal-imidazolate-metal angle (M-Im-M) is close to 145°, which is similar to the Si-O-Si angle in zeolites [61], Figure 1.4.

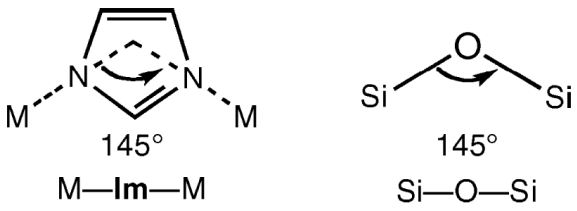

Figure 1.4: Metal- imidazolate-metal angle in ZIFs compared to the Si-O-Si bond in zeolites [61]. Copyright 2010 American Chemical Society

As a result, ZIFs form a range of structures similar to those found in zeolites [61, 62, 63, 64, 65]. The flexibility of the M-Im-M bond also allows for topologies that have not been observed in traditional zeolites [63, 62, 61]. The bridging imidazole units are suspected to play a secondary role of directing topology through link-link interactions [61]. New structures could be obtained by changing the

metal, the imidazolate linker, or the solvent used [61, 66, 67, 68, 63]. The diversity in the choice of building blocks, Figure 1.5, leads to a wide family of ZIFs with different structures. Figure 1.6 includes some representative ZIF structures.

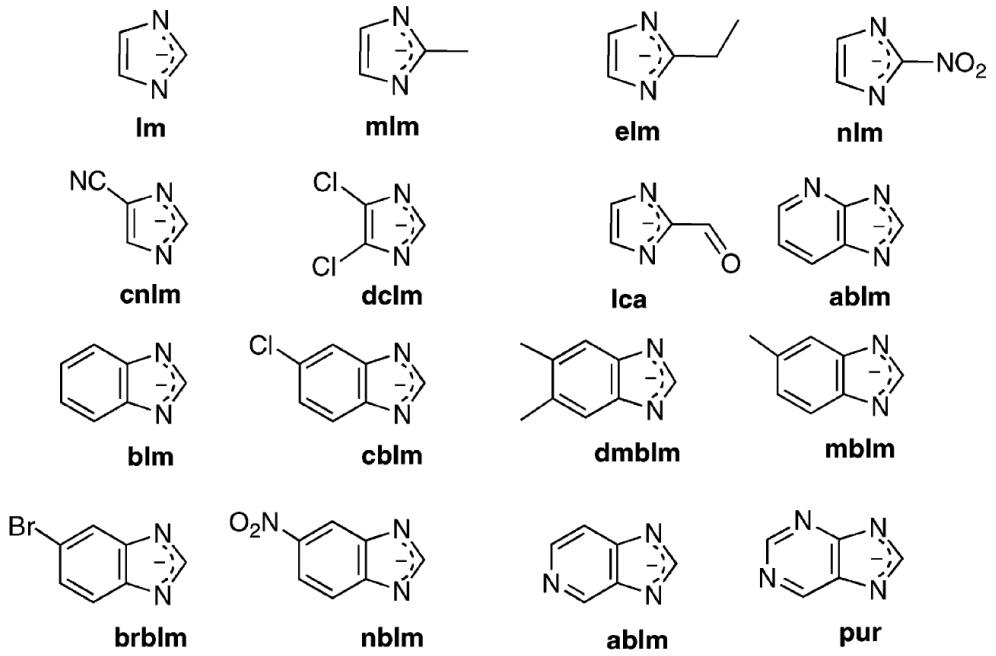

Figure 1.5: Different imidazole ligands used in ZIF synthesis [61]. Copyright 2010 American Chemical Society

The general properties of ZIFs combine those of MOFs and zeolites and include intrinsic porous characteristics, unimodal pores, high surface areas, high crystallinity, and exceptional thermal, mechanical, and chemical stabilities [62, 69, 70, 71, 72]. These desirable properties of ZIFs have attracted considerable interest as they lend themselves to a variety of applications.

1.2.2 ZIF Synthesis

Traditionally, ZIF structures are prepared by solvothermal or hydrothermal synthesis methods, and in the past years, new solvent-based methods have been developed. However, the ZIF yield is usually small; this makes the synthesis costly [73] and has led to the emergence of new non-solvent-based methods as well.

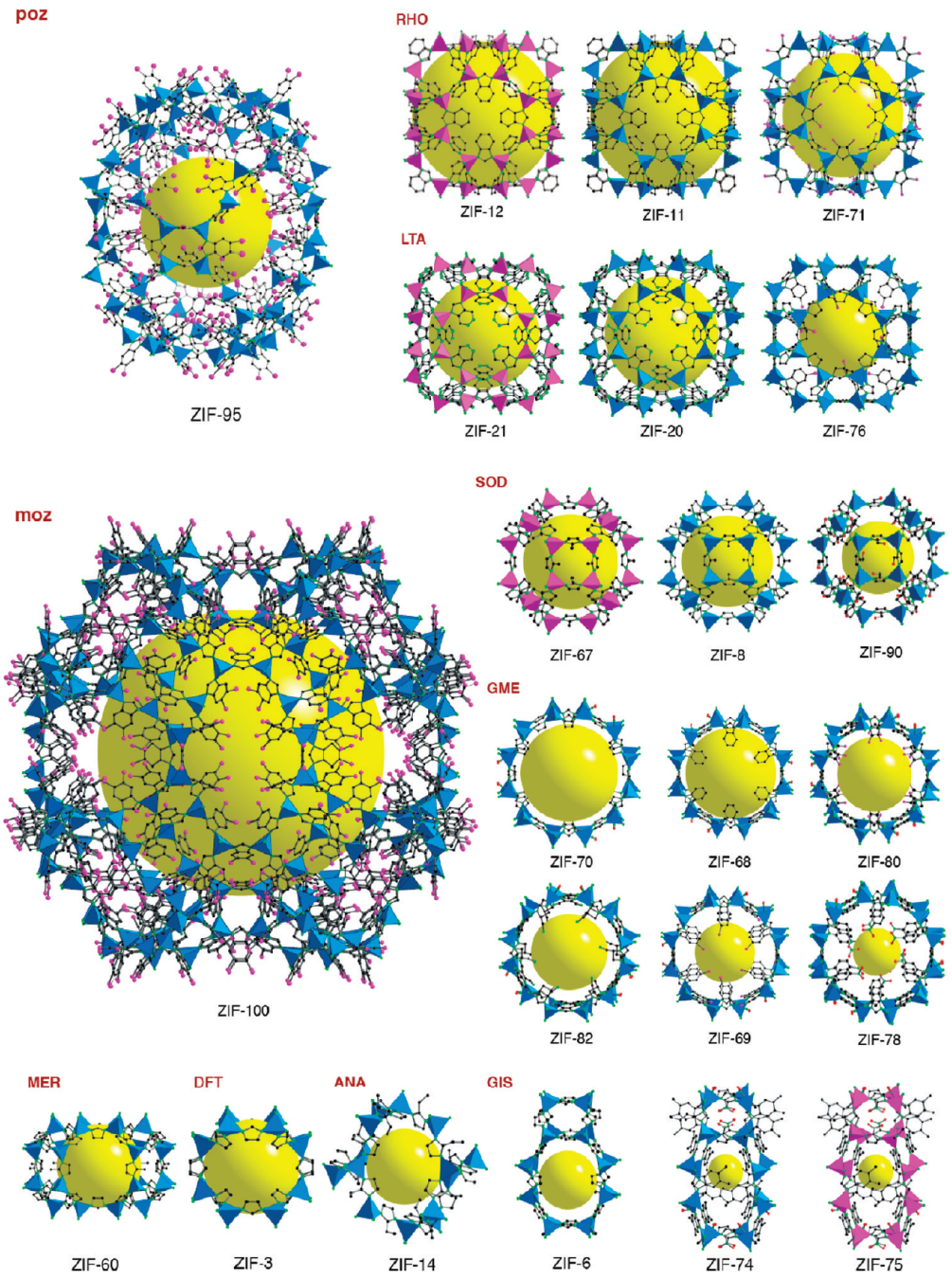

Figure 1.6: Different ZIF structures grouped by similar topologies [61]. The blue and pink tetrahedra represent the Td coordinated metal ion. The yellow spheres represent the pore in the cage. Blue is for Zn^{2+} and pink for Co^{2+}. Copyright 2010 American Chemical Society.

Solvothermal, Hydrothermal, and Ionothermal Synthesis

In a solvothermal or hydrothermal synthesis, the organic linker and the metal salt are dissolved in the appropriate solvent, usually in a tightly-capped vessel, and then heated in an oven to generate pressure [56]. MOF materials are conventionally prepared through this method, and ZIFs were first introduced by Yaghi et *al.* [62] using solvothermal synthesis in 2006. Modifications to the original method by changing the solvent or using additives have been used to control particle size and facilitate material formation. Organic amines such as pyridine and triethylamine are used as deprotonating agents to favor the reaction [74, 75, 76]. Synthesizing ZIF-8 in methanol leads to smaller particles than in N,N-dimethylformamide (DMF) [77], and synthesis using methanol was later improved by using high molecular weight poly(diallyldimethylammonium chloride) additive as a stabilizer [78] and by using modulating ligands such as sodium formate/1-methylimidazole and n-butylamine to tune the crystal size between 10 and 65 nm [79].

Hydrothermal synthesis is a chemical preparation that replaces the organic solvent with water and was first used in the synthesis of zeolites [80, 81]. It usually occurs at temperatures below or above 100 °C, and pressures greater than ambient pressure [82]. Similar to the solvothermal synthesis, the crystal growth depends on the selection of reaction conditions like concentration and metal salt/ligand ratio, temperature, and pH value of the solution [83]. Pan et *al.* [84] were the first to synthesize ZIFs using the hydrothermal method at room temperature via a simple procedure which relied on the high excess of the organic linker. The water-based system was also modified using additives to allow for decreasing the amount of organic linker used [85, 86], and eventually lead to synthesis from stoichiometric ratios [87, 88]. Aqueous ammonia solution has been used to synthesis ZIF-8 from stoichiometric ratios and also allowed for controlling particle size and texture by changing the concentration of ammonia in the synthesis mixture [88].

The Ionothermal method is an extension of the solvothermal synthesis that uses non-aqueous ionic solvents. For the synthesis of ZIFs, ionic solvents are made of salts that are fluid at temperatures used in the synthesis of ZIFs, or eutectic mixtures of an organic salt mixed with other species to depress the melting point to a suitable temperature[89]. The ionic liquid acts as both the solvent and the template provider. They are usually polar, and thus are good solvents for the ionic precursors, and also remove the competition between template-framework and solvent-framework interactions that takes place in hydrothermal synthesis [90]. Because of their low vapor pressure, the synthesis takes place at ambient pressure. The ionic liquid could also be reused. The ionothermal synthesis was introduced for zeolites by Morris and co-workers [89] in 2004, and then for ZIFs

and MOFs in 2007 [90].

Microwave and Sonochemical Synthesis

Conventional heating methods used in the solvothermal synthesis result in temperature and concentration gradients within the reaction vessel, which could influence the growth mechanism of the crystals and lead to broad particle size ranges [91, 92]. Alternative energy sources for ZIF synthesis include ultrasound and microwave irradiation. Both supply the system with the needed energy differently from conventional heating. Heating through microwave irradiation occurs through dipole rotation and ionic conduction: the microwave energy interacts with ionic molecules or those bearing a dipole, which then transfer the energy to surrounding molecules by collision. This results in an efficient energy transfer with high heating rates and a decrease in gradients [93]. This technique allows for narrower size distributions, and Park et *al.* observed a decrease in ZIF-8 particle size and synthesis time in comparison to solvothermal electric heating [94].

In sonochemical synthesis, the ultrasound radiation does not directly interact with the molecules because of its higher wavelengths but cause the formation, growth, and collapse of bubbles in the solution. The collapse of the bubbles formed by "acoustic cavitation" produces high local temperatures and pressures, that leads to rapid heating and cooling rates greater than 1010 K/s [95, 96], which encourages nucleation and hinders growth. ZIF-8 was synthesized using the sonochemical method in shorter synthesis time and lower temperatures than in the solvothermal method, leading to particles that are smaller and monodisperse [97].

The high nucleation rate in microwave and ultrasound heated synthesis results in the depletion of reactants from the reaction mixture, preventing further growth and resulting in narrower size distributions. The general size trend observed for the same ZIF synthesis is: conventional heating $>$ microwave heating $>$ sonochemical heating, with narrower particle size distributions with the last two methods [93].

Microfluidic Synthesis

In microfluidic systems, minute amounts of fluids containing either the metal precursor or the organic linker are pumped through channels with micro-scale diameters into a T-junction, where the aqueous solution forms droplets in the organic phase [98]. As the droplets pass through hydrophobic tubing, the capsule shell of ZIF is formed [99]. The flow rate of either solution could be adjusted independently to control the mixing conditions. In an alternative set up, the

two liquids co-flow side by side, forming a liquid-liquid interface where MOF nanofibers form [100]. This system was further adjusted to trap the synthesized nanofibers in the reactor to control the position of the nanowire bundles and be able to perform post-synthesis modifications on the trapped structures [101].

In general, the rapid mixing in a microreactor leads to homogeneous reaction conditions [102], and the synthesis times are short, in the range of a few minutes [103, 102]. The ZIF shape could be altered by tuning the liquid-liquid interface parameters [100, 101, 99], and factors like temperature and residence time could also be used to control particle size [103]. Yamamoto et *al.* [104] reported the rapid microfluidic synthesis of ZIF-8 nanoparticles in excess 2-methylimidazole. The solutions were mixed in a T-junction at different flow rates, temperatures, and linker concentrations. They concluded that lower temperatures and higher linker:metal ion ratios lead to the formation of smaller ZIF-8 particles, as the temperature affects the nucleation process and the reactant ratio affects the growth process.

Electrochemical Synthesis

The electrochemical synthesis of MOFs was introduced by researchers at BASF [105] in 2004. In the electrochemical preparation of MOFs, the metal ion is provided to the reaction solution by anionic oxidation of a solid metal electrode. The metal electrode is immersed in a solution of the organic linker, and a biased electrical voltage is applied to initiate the electrochemical oxidation of the metal atoms which leads to the dissolution of the metal ions. The solution is stirred, and MOF crystallites form in the vicinity of the electrode. The growth of the crystals is driven by the continuous supply of the metal ions. This method was later modified by Ameloot et al. [106] for the production of MOF films that grow on and coat the metal electrode by careful optimization of the reaction conditions in the absence of stirring. Moreover, the thickness of the MOF film could be adjusted from 4 to 20 nm depending on the voltage used and the composition of the solvent.

The electrochemical method provides control over the metal cation concentration through the regulation of the current density. Other advantages of this method include faster synthesis at lower temperatures, the use of metal electrodes which avoids the introduction of anions from metal salts, and the total utilization of the linker [107]. However, organic media is needed to dissolve the linker, and the electrochemistry of such media is not thoroughly explored. ZIF-8 was prepared electrochemically using a variety of solvents and electrolytes and in temperatures as low as 0 °C [107]. Under all the tested conditions, the BET surface area of the synthesized ZIFs was in the range of 1400-1700 m^2/g, and the particles were smaller than 1 μm with a narrow size distribution. Changes

in temperature did not affect the morphology of the formed particles, but higher yields were observed at lower temperatures. The productivity was also found to increase linearly with current.

Mechanochemical Synthesis

Mechanochemical synthesis is a solvent-free method that uses ball milling to grind the metal salt with an excess of the organic linker at room temperature. The milling provides the mechanical energy needed to break intramolecular bonds in the precursor and for the chemical reaction to take place [108]. The mechanochemical synthesis of MOFs was reported by James et *al.* [109] in 2006 using a neat grinding method that avoids the use of any solvent in the reaction. Copper(II) acetate monohydrate and isonicotinic acid were milled for 10 minutes before the byproducts of water and acetic acid were driven off by heating. The advantages of this approach include being able to use metal oxide precursors and the formation of water as the by-product which removes the need for purification steps. This method was used to convert zinc oxide and 2-methylimidazole into ZIF-8 powder, with a BET surface area of 1480 m^2/g [110]. The presence of small amounts of solvent (liquid-assisted grinding, LAG), or both inorganic salt and solvent (ion-and-liquid-assisted grinding, ILAG) could enhance the reaction rate and crystallization of MOFs from oxides. ILAG was used to convert stoichiometric ratios of zinc oxide and different imidazolate ligands into ZIFs with different topologies depending on the chosen inorganic salt [111].

Diffusive Synthesis Methods

The most common diffusion procedure used for synthesis is the liquid-liquid or free interface diffusion, where two or more reagent solutions form distinct layers in a reaction vessel [93]. The slow diffusion that occurs between the immiscible solutions leads to a reaction between the reagents, creating crystal nuclei in the interface region, favoring the formation of large crystals with well-defined morphologies. The crystal growth is time-dependent and can be affected by concentration changes as the reaction proceeds. The miscibility grade of the solvents used also affects the crystallization kinetics and influences the size and morphology of the crystals. For example, ZIF-90 synthesized by slow diffusion of a solution of triethylamine in hexane into a dimethylformamide solution containing imidazole2-carboxaldehyde and Zn^{2+} at room temperature results in well-defined nanopolyhedra, while the diffusion of pure triethylamine into the same second solution leads to a superstructure formed from irregular nanospheres [112].

Synthesis *via* Reaction-Diffusion Frameworks in Gel Media:

Recently, the synthesis of MOF-199, ZIF-8, ZIF-67, and ZIF-7 *via* liquid-gel reaction-diffusion frameworks was reported by our lab group [113, 114, 31]. The method allows for tuning particle size by changing reaction parameters like the metal ion concentration in the gel medium, the concentration of the organic linker in the solution, the gel concentration, and the ambient temperature. Furthermore, within the same reactor, the particle size gradually increases with an increase in distance from the diffusion interface. The particle morphology is affected by the type of gel used and by the chosen metal salt precursor [113]. For example, MOF-199 synthesized in agar gel is cubic, while that in agarose is polyhedral. This method was also used to successfully synthesize mixed-metal ZIFs [114, 31] and mixed-linker MOFs [113]. This method is also scalable and allows for a reduction in the amount of organic solvent used.

Factors that Affect Size and Morphology

For the same ZIF and the same synthesis method, the synthesis conditions could affect the morphology and size of the resultant particles. Understanding MOF crystallization is crucial for later being able to set synthetic protocols in controlling crystal morphology [115]. A typical mechanism for the formation of MOFs includes the self-assembly of metal clusters and linkers that forms primary nuclei that grow into larger crystallites either by agglomeration or by the addition of solution species. However, the characteristics of the nucleation and growth periods not only depend on the reaction conditions but also differ from one MOF to another [93].

The morphology of a given MOF is usually correlated with the internal structure and depends on factors like the symmetry element of the unit cell, the crystal system, or space group [116, 117] For example, crystals belonging to cubic systems grow in an equidimensional way. The symmetry elements allowed in the I-43m space group result in the rhombic dodecahedral shape of ZIF-8 crystals often observed at equilibrium [62]. The final morphology of the particles is also affected by the specific growth rates for each crystal plane, and the way building units arrange on a growing crystal‘s surface. These two factors could, to some extent, be manipulated using external factors like the metal to linker ratio, solvent composition, external or internal modulators, surface blocking and capping agents, and temperature [93]. Finally, the surface growth mechanism also plays a role in determining the final morphology of the crystals. The surface growth mechanism changes according to the supersaturation level: spiral growth occurs at lower supersaturation levels, adhesive growth at high supersaturation, and two-dimensional “birth and spread” growth in the middle range [118].

Generally, for a given synthesis method, the synthesis conditions that could affect the final morphology include the solvent used, the presence of impurities or surfactants, the reactant concentrations, the nature of the metal precursor, stirring conditions, and temperature.

The Nature of the Solvent: The nature of the solvent plays a role in the final particle shape and morphology because it determines the solubility of the reagents and thus affects the supersaturation and kinetics of crystal formation [119, 120]. For example, Guo et *al.* [121] showed that changing the ratio of DMF to water affects both the morphology and the size of NH_2-MIL-53(Al), and were able to use this to tune the particle size in a range from 76±20 nm in pure DMF up to 520±120 nm in pure water. The shape also evolved from spherical aggregates in the smaller particles to rhombic particles in the bigger sizes. The higher concentrations of DMF lead to the higher supersaturation of the linker, which accelerates the nucleation process and results in smaller particles. The choice of solvent could also affect the stability of intermediate nanoparticles [122, 121], or play a role as a stabilizing agent in the self-assembly process of the MOFs and affect the size distribution [123, 124]. The solvent purity could also play a role in size distribution and morphology [125, 126]. However, even though the effect of the solvent has been documented in many works, the reasons are not always fully understood [93].

Reactant Concentration Ratios: Dilution conditions and the metal to linker ratios affect the supersaturation of the solution and affect the size and shape of MOF particles. Changing the concentration of the precursor solutions has been used to change the morphology of MOFs from rod-like to truncated cubes [127] and from thin to thick nanorods [128, 129]. In mixed-linker ZIFs, changing the ratio of linkers could inhibit growth in a certain direction [74], affect both size and morphology, or only affect the size of the crystals [130], depending on the used ZIF system.

Nature of the Metal Precursor: The metal precursor used could affect the crystal shape and proportions, and could also lead to different growth mechanisms [131, 132].

Stirring Conditions: Stirring conditions play a strong role in direct precipitation synthesis methods, and going from static to rigorous stirring while keeping all other variable constant could lead to a transformation in morphology [128, 129]. For example, nanospheres of [SnT(4-Py)PCl_2:Pt] form in the reaction mixture under static conditions, while well-defined nanorods were observed under vigorous stirring [133].

Temperature: The temperature affects the solubility of the reagents and the supersaturation of the solution. The choice of an appropriate reaction temperature can result in bigger and better-defined particles [120, 130], and could also

allow for control over the evolution of the colloidal solutions. For example, Chen et *al.* [134] showed that adjusting the reaction temperature and cooling rates results in different morphologies of MOF-177. Cubic microcrystals were precipitated at low temperatures and short reaction times, while slow cooling rates encouraged the formation of cubic prisms.

1.2.3 ZIF Applications

The intrinsic properties of ZIFs lend themselves to a diverse array of applications, the most studied of which include gas separation and storage, water purification, and catalysis. Other applications include using ZIFs as sensors for chemical vapors [135], as *in vivo* glucose biosensors [136], for detecting metal ions in small molecules [137], for DNA detection [138], or as potential semiconductors in electronic devices [139, 140]. The possibility of using ZIFs as controlled-release anticancer drug vehicles has also been studied [141, 142, 143] due to their thermal and chemical stability and pH sensitivity.

Gas Separation and Storage

In light of current global issues, research on gas separation for natural gas purification, carbon dioxide capture and storage, and hydrogen storage is gaining importance. The three gas adsorption processes of industrial significance are: (1) CO_2/N_2 or CO_2/CH_4 separation for carbon capture and sequestration (CCS) or natural gas or biogas purification, (2) CH_4 and H_2 storage as an alternative to petroleum-based fuels for automobiles, and (3) alkene/alkane separation in the petrochemical industry [144]. Due to their tunable pore size and variable structures, both the powder and membrane forms of ZIFs have been considered for these applications, with H_2 and CO_2 capture being the most investigated topics. The selectivity and efficiency depend on the chosen ZIF‘s properties like pore size, pore charge, and hydrophobicity, the nature and content of the target gas, and the operating conditions like temperature and pressure.

Studies comparing CO_2 adsorption performance of ZIF-8 to zeolite 13X revealed that even though ZIF-8 is hydrophobic, stable in water, and has total reversibility in adsorption, it shows lower selectivity and significantly less CO_2 uptake than zeolite 13X [145, 146]. Efforts to improve CO_2 capture by ZIF powders have focused on using linker functionalization, as experimental [147, 148] and computational [149, 150, 151, 152] works have shown that the sites near the imidazolate bridging compounds are the primary adsorption sites for hydrogen, methane, and carbon dioxide.

The CO_2 uptake performance of functionalized ZIFs at 0.1 MPa and 25 °C

rated in decreasing order is as follows: NO_2 functionalized ZIF-78 > CN, Br, and Cl functionalized ZIF-82,81,69 > C_6H_6 and CH_3 functionalized ZIF-68 and 79 > ZIF-70 > BPL activated carbon; the trend suggests that a greater attraction between polar functional groups and CO_2 helps improve ZIF performance [153]. The modified ZIF-8 captured approximately 3 times as much as the BPL carbon. This trend is in agreement with another study on ligand functionalization in SOD topology ZIFs that showed that modifying the linker dipole moment can lead to 5 to 7 fold improvement in the CO_2 selectivity for CO_2/CH_4, CO_2/N_2, and CO_2/CO mixtures [154]. Using mixed-linker ZIFs is another approach to increasing performance in CO_2 capture and storage. Thompson et *al.* [155] found that both ZIF-8 made of 2-methylimidazole and 2-aminobenzimidazole linkers and another mixed-linker ZIF of 50:50 mole ratio of 2-methylimidazole and carboxaldehyde-2-imidazole that was followed by post-synthesis functionalization with ethylenediamine showed improved performance.

ZIF-95 and ZIF-100 have shown an impressive performance in CO_2 adsorption and capture. Both structures have very large cavities of 2.4 and 3.6 nm, respectively, highly restricted windows of 3.65 and 3.35 Å, respectively, see Figure 1.6, and strong quadrupolar interactions with CO_2 *via* the N atoms in the imidazolate linkers, which result in high performance in CO_2 capture with high CO_2/N_2 selectivity and high capture capacity at 0.1 MPa, with complete reversibility in adsorption [63]. One liter of ZIF-100 can store 28.2 L of CO_2 at 273 K and 15.9 L at 298 K under ambient pressures.

The potential of using ZIF-8 in hydrogen gas storage was also explored. Park et *al.* [62] reported an excess adsorption capacity of 3.1 wt% for evacuated ZIF-8 at 77 K and 55 bar. Wu et *al.* [147] showed that unmodified ZIF-8 has an absolute hydrogen storage capacity of 4.2 wt% at 30 K, which, unfortunately, is lower than the storage target of 6 wt% suggested by U.S. DOE for on-board hydrogen storage [156].

The possibility of using ZIF-8 as a coating material in silica capillary columns for gas chromatography has been investigated by Chang et *al.* [157], who were successful in separating mixtures of linear alkanes and sieving branched isomers from the linear ones, a valuable process in petroleum refining.

Water Purification

ZIFs have also been used as adsorbents for waste-water treatment. The greatest number of studies are on ZIF-8, and it has shown a high selectivity in the adsorption of: arsenic and p-arsenate [158, 159, 160], chromium(VI) ions [161], humic acid [162], phtalic acid [163, 164], diethyl phthalate [163], benzotriazoles [165]. Sann et *al.* [166] demonstrated the potential of using ZIF-8 for cleaning

oil spills by placing ZIF-8 in tea bags. Their "spill pouches" successfully and selectively removed the oils from the water; the oil could be readily removed from the surfaces of particles by heating combined with reduced pressure treatment, and the pouched could be reused for twenty cycles.

ZIF-8 has also been used for the removal of organic dyes like rhodamine B, methylene blue, and methyl orange [167]. ZIF-8 is reported to be the most efficient in the adsorption of methylene blue and outperformed both activated charcoal and graphene oxide [168]. An approach to enhancing adsorptive performance in ZIFs is using mixed-metal structures. Saliba et *al.* [114] showed that using ZIF-8 doped with cobalt enhances methylene blue adsorption, Tanh et *al.* [169] showed that using a zinc-iron mixed metal ZIF-8 enhances the adsorption of remazol deep black dye, and Abdi et *al.* [170] found that modifying ZIF-8 with amine increased adsorptive capacity for acid blue 92 dye by 62% and that for direct red 80 dye by 60%.

Catalysis

ZIFs are expected to have good potential in catalytic applications since they have accessible pores and could be easily functionalized. The large range of pore and aperture sizes in the different ZIF structures allows for high affinity and selectivity with diverse target material [171]. Both the metal ion and organic linker play a role in catalytic reactions, so functionalization of the imidazolate bridges could enhance catalytic activity by changing the electronic and steric properties of the metal sites [62]. For example, for Lewis acid, Lewis base and Brønsted base-catalyzed reactions, the ZIF-8 framework already contains the Lewis acid Zn^{2+} and nitrogen base moieties, and the Brønsted base sites can be created through functionalization. ZIF-8 and functionalized ZIF-8 were used as acid or base catalysts in different organic reactions like the Knoevenagel condensation [172, 69, 173, 174], cycloaddition of CO_2 to alkene oxide [175, 176, 177], Friedel-Craft acylation of anisole and benzoyl chloride under open-air atmosphere conditions [178], and for the transesterification of vegetable oil using a range of alcohols (methanol, ethanol, 1-propanol, 1-butanol, isopropanol and tertbutanol) [179].

Another approach is using ZIFs as good carriers of an active mass such as metal particles. For example, a mixture of ZIF-8 nanocrystals with a small amount of gold nanoparticles and cobalt oxide was used to convert carbon monoxide into carbon dioxide at temperatures lower than 250 °C [180, 181], while ZIF-8 on its own does not exhibit such catalytic activity. It was also reported that ZIF-8 with encapsulated gold nanoparticles could be used for the catalytic oxidation of benzyl alcohol to methyl benzoate [182]. Loading platinum-coated titania nanotubes with ZIF-8 was found to narrow the bandgap of the material and enhance its photocatalytic degradation of organic pollutants [183].

Importance of Morphology and Size

Control over the size and morphology of ZIFs during synthesis also affects their use in applications, as appropriate size and morphology could lead to a better interaction with targeted molecules [184, 185, 186]. The morphology of a crystal results from its crystal structure, attachment energy, and the rates of attachment during the crystallization. This means that ZIFs of the same chemical composition and crystal structure may have different morphologies depending on the synthesis conditions that alter the growth rate and attachment energy of the framework, like supersaturation, temperature, the solvent used, and the presence of impurities or surfactants [187, 188, 189]. Given ZIFs with different morphologies will have different face orientations, which would affect properties like accessible pore and functional group orientation. This, in turn, will affect the efficiency of the interaction between the targeted compounds and the functional groups or the pores [186, 189]

The size of the ZIF particles also plays an important role in applications. For example in a study on the use of ZIF-8 as a catalyst for the Knoevenagel condensation reaction of benzaldehyde and malononitrile at room temperature, Tran et *al.* [69] found that smaller crystals showed higher activity than larger ones, and attributed this to the higher external surface area. Cho et *al.* [172] studied the same system but used ZIF-8 particles in the range of 700 nm synthesized *via* a sonochemical route. This catalyst exhibited significantly higher activity than that prepared by Tran et *al.*, which was synthesized solvothermally and is significantly larger at 250 μm.

1.2.4 Effect of Electric Fields on MOFs and ZIFs

Research on the effect of external electric fields on non-ferro- or piezoelectric MOFs is still limited. In 2013, Yanai et *al.* [190] studied the effect of an alternating current external electric fields on ZIF particles suspended in solution. Monodisperse polyhedral ZIF-8 particles up to 5 μm in size were synthesized then dispersed in ethylene glycol. The system was then subjected to an AC electric field of 1 kHz or 1 MHz frequency. The result was a regulated crystal orientation, for both rhombic dodecahedra and truncated cube morphologies. The particles attached to each other within seconds of coming into contact, and within a few minutes from the onset of the electric field 1-dimensional chains started to form. Before attaching to the chains, the polyhedra reoriented to form facet-to-facet contacts, resulting in 1-D chains oriented in the direction of the electric field, Figure 1.7. After removing the high-frequency field (1 MHz), all the chains disassembled. However, chains of rhombic dodecahedral ZIF-8 constructed at 1 kHz remained stable after turning off the electric field. They also concluded that ma-

nipulating surface area and surface curvature make selective attachment between facets possible.

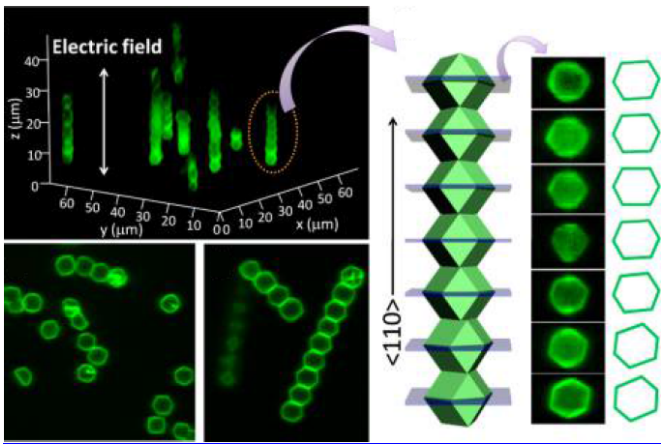

Figure 1.7: *In situ* observation of electric field assembly of rhombic dodecahedral ZIF-8 chains along the direction of electric field *via* confocal microscopy. From [190] Copyright 2013 American Chemical Society

Other groups directed their studies towards using an external electric field to enhance gas separation performance on MOFs and mostly focused on the "breathing" behavior of MOFs with soft porosity. This effect was first reported by Ghoufi et *al.* [191] in 2017, who performed molecular dynamics simulations on the breathing of MIL-53. They used advanced molecular simulations to demonstrate that the application of an electrical field in the range of 1- 2 V/nm induces the reversible structural switching of MIL-53(Cr). The electric field leads to a volume change of more than 40 %, with a drastic drop of the aperture of the channel from 12.8 Å in the initial form to 7.9 Å in the contracted pore form. This structural shrinkage under a high electric field is a first-order transition that is driven by the rotation of the linker. They also proposed the new concept of electrically tuning the pore size of MIL-53(Cr) to selectively capture CO_2 over CH_4 in a molecular sieving process. They showed that using the electrical field to maintain the structure in the narrow pore form during adsorption could lead to a full separation of CO_2 over CH_4 through a size exclusion effect. However, the magnitudes of the electrical fields used in the simulations are large due to the resilience of the MOF framework and are above the breakdown electric field of air.

Soon after, Schmid [192] proposed a molecular explanation for the electric field-induced phase transition of MIL-53(Cr). In the MIL framework, a positively charged metal ion is surrounded by negatively charged donor atoms. This unit could be deformed by a strong electric field which will create a local dipole moment. In addition, the bridging O-H groups carry local dipole moments that

point in alternating directions. An electric field could reorient these O-H groups which would also induce a local dipole moment. By deforming to a rhombic shape, the short-ranged attractive interactions increase. Thus, the driving force for the breathing is the mutual dipole-dipole interaction, and the electric field acts as the source for the necessary polarization. This qualitative description was very recently confirmed by mathematical modeling by Kolesnikov et *al.* [193].

Tam et *al.* [194] approached the use of an electric field to enhance molecular sieving in MOFs from a different angle, and proposed to mount molecular gates on the open-metal sites of MOFs and control their opening and closing *via* and electric field. They demonstrated the concept using DFT and classical molecular dynamics calculations on a system of 4,5-dimethyl-9,10-bis(trifloromethyl)pyrene-2,7-dicarboxylic acid for the gate and Mg-MOF-74, and high electric fields in the vicinity of 3 V/nm. The chosen MOF benefits from hexagonal one-dimensional channels and a high density of open metal coordination sites that could act as anchoring points for the gate. The gate molecule has carboxyl groups on both ends that can coordinate with the metal sites and a permanent dipole that would respond to the electric field. Their calculations show that the MOF-molecular gate complex can be switched between two stable configurations, open and closed, by turning on and off an external electric field. They also successfully tested the system with methane.

In the first experimental study on the topic, Knebel et *al.* [195] were able to exploit the soft porosity of the ZIF-8 framework, and use *in situ* a direct current (DC) electric field to switch gas transport through a ZIF-8 membrane. The resultant stiffening of the ZIF-8 lattice causes a reduction in gas transport through the membrane and sharpens the molecular sieving capability. ZIF-8 membranes of different thicknesses were subjected to a DC electric field of 500 V/mm, reversibly polarizing the ZIF-8 and transforming the lattice from cubic to monoclinic and triclinic polymorphs. This shifting was attributed to the lattice flexibility and linker movement. In the *Cm* space group, the limiting pore diameter of ZIF-8 changed from 3.4 to 3.6 Å in the polymorph. The stiffening of ZIF-8 improved molecular sieving for propene-propane mixtures but decreased separation selectivity for small molecules, such as H_2, CO_2, and CH_4. However, fields of 500 V/mm are not enough to completely align the linkers, and only an estimated 30% of the ZIF layer was transformed into metastable polymorph states.

The following year Namasani et *al.* [196] used DFT and molecular dynamics calculations to study the behavior of halogenated isoreticular MOFs in a high external electric field in order to manipulate the diffusion of molecules in the nanopores and successfully tested their system using methane molecules. The MOFs are halogenated to create permanent dipole moments on the linkers that would respond to changes in the direction and magnitude of the electric field. The strength of the electric field needed to control the rotation of linkers could be re-

duced depending on the chosen ligand size, the halogen type, and the substitution position. Cl substitution on larger linkers was the most effective, functioning with electric field strength as low as 0.5 V/nm.

1.2.5 ZIF-8: The Prototype MOF Material

Zeolitic imidazolate framework-8 (ZIF-8) is one of the most studied MOFs, and was first introduced by Huang et *al.* [67]. It is made of Zn^{2+} metal ions tetrahedrally coordinated by four nitrogen atoms from the 2-methylimidazole (mIm) linker. It has a cubic space group ($I\overline{4}3m$, a=16.991 Å) and a sodalite topology (SOD), with large 11.6 Å pores that are accessible through small apertures of 3.4 Å. It is hydrophobic in nature, thermally stable in ambient conditions up to 450 °C, and resists being boiled in benzene, methanol, and water for up to 7 days [62]. It has a surface area of 1630 m^2/g (BET) and a pore volume of 0.636 cm^3/g.

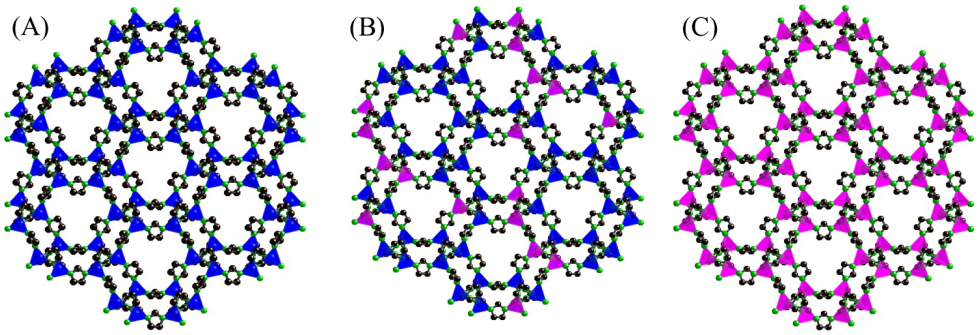

Figure 1.8: The crystal structure of ZIF-8 (A), Zn-Co mixed metal ZIF-8 (B), and ZIF-67 (C). The blue tetrahedra represent the Td coordinated Zn^{2+} ions, and the pink ones represent the Td coordinated Co^{2+} ions, the black spheres represent the carbon atoms, and the green spheres represent the nitrogen atoms. The hydrogen atoms are omitted for clarity.

Mixed-metal MOFs contain at least two metals in their structure and could exhibit enhanced properties for use in a certain application. ZIF-67 has the same structure and topology as ZIF-8 but uses Co^{2+} instead of the Zn^{2+} ions. Zn/Co-ZIF-8 is the mixed-metal variation, with only some of the zinc(II) ions replaced, figure 1.8. In an extensive study comparing the three structures Zhou et *al.* [197] found that Zn/Co-ZIF-8 has the highest hydrolytic stability between the three materials, higher catalytic activity than the single metal ZIFs, and better CO_2 adsorption performance than ZIF-8. Saliba et *al.* [114] showed that the doped variant has better adsorptive performance towards methylene blue dye, and Butova et *al.* [198] also showed that the part of iodine adsorbed by the

external surface of the structure is higher in the mixed metal than in the pure zinc analog.

Due to its properties, ZIF-8 has become a popular compound in the studies on potential applications of MOFs [147], and so far has been studied for use in CO_2 capture, hydrogen and methane storage, as a molecular sieve, drug delivery, and sensing. However, current synthesis methods have a low yield, so the applications of ZIF-8 and MOFs, in general, are still at the prototypical stage [73].

1.3 Aim of the Present Work

In the present work, we report for the first time the effect of an external electric field on ZIF particles during synthesis in a reaction-diffusion framework (RDF). The effect of small-scale electric fields on the reaction-diffusion process and the resulting precipitation patterns is well known and has been extensively studied, but how it affects the precipitated particles themselves is still uncharted territory. Since the electric field affects reaction parameters like the concentration gradients through ion migration, it could affect the mechanism of crystal growth and consequently the size and morphology of the formed precipitate. Even though previous studies on the effects of electric fields on MOFs and ZIFs use electric fields in the range of V/nm, this could imply that fields of much smaller magnitudes, that will not cause the gel structure to collapse, could still affect ZIFs synthesized *via* reaction-diffusion.

In this study, we apply a weak direct current (DC) external electric field to a 2-dimensional reaction-diffusion framework of the prototypical ZIF-8 with the aims of:

1. Investigating the effect of the electric field on the precipitation dynamics and patterns of ZIF-8.
2. Introducing a weak external electric field as a new parameter for controlling ZIF synthesis through:
   (a) Investigating the possible effects of the electric field on the size and morphology of ZIF-8, ZIF-67, and Zn-Co mixed-metal ZIF-8.
   (b) Investigating the effects of the electric field on the Zn:Co ratio in mixed-metal ZIF-8.

Chapter 2

Materials and Methods

2.1 Preparation of ZIF Crystals

2.1.1 Experimental Procedure

The ZIF-8, ZIF-67, and Co-doped ZIF-8 crystals are prepared using a 2-dimensional reaction-diffusion method, adapted from the method used in our lab for the 1-dimensional RD synthesis from sulfates [31] and nitrates [114]. The amount of DMF used in the gel mixture is decreased by half, since the 2-D reactors are made from plexiglass, and would dissolve in concentrated DMF.

An agar solution containing the metal ions (inner electrolyte) is poured into the circular plexiglass reactor dish, is covered, and left to gelate in an air thermostat chamber at 23±0.1°C for 2 hours. The cover and the base of the reactor are separated by three spacers, giving a uniform gel thickness of 0.7 mm. The gel at the bottom of the central cylindrical reservoir is removed, and the outer electrolyte solution of 1 M 2-methylimidazole is poured into the reservoir and diffuses radially into the gel matrix, Figure 2.1.

A potential difference is applied through circular tungsten electrodes. In the case of a direct positive field, the inner electrode in the reservoir is connected to the positive pole of the power supply, and the outer electrode around the cover of the dish is connected to the negative pole. In the case of a direct negative field, the opposite connections are applied.

The formation of the precipitate and the pattern evolution are monitored using a mounted CCD camera controlled by a computer when needed. After 7 days of diffusion for the sulfate system, and 4 days for the nitrate system, the outer electrolyte is poured out, the reactor cover is carefully lifted, and the gel containing the precipitate is sectioned and collected. The samples are washed

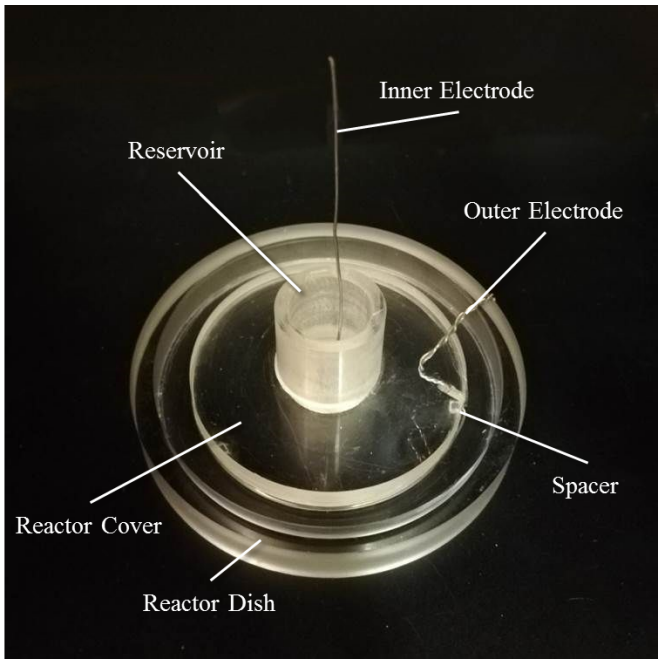

Figure 2.1: The 2-D circular reactor. The gel is sandwiched between the plate and the cover, and the outer electrolyte is poured into the central reservoir.

in DMF in a double-boiler to remove the gel and the unreacted species and are freeze-dried (Labconco, FreeZone) overnight to be ready for characterization.

Preparation of ZIF-8

A solution of 20 mM Zn^{2+} ions is prepared in 25:75 DMF:water solution using zinc sulfate or zinc nitrate powder. After dissolution, 1% w/w agar powder is added and the solution is heated with continuous stirring until the solid gel dissolves. The solution is then transferred to the reactor and covered.

Preparation of ZIF- 67

A solution of 20 mM Co^{2+} ions is prepared in 25% DMF using cobalt sulfate or nitrate salts. 1% w/w agar powder is added then the solution is heated with continual stirring until all the gel dissolves before being poured in the reactors and left to rest and gelate.

Preparation of Zn-Co Mixed-Metal ZIF-8

A mixture of different percentages of Zn^{2+} and Co^{2+} ions with a total metal ion concentration of 20 mM is prepared in 25% DMF. The solution is mixed with 1% w/w agar powder and heated with constant stirring until the gel dissolves before being poured into the reactor and covered.

2.1.2 Materials

Zinc sulfate monohydrate ($ZnSO_4 \cdot H_2O$, 99%) and zinc nitrate hexahydrate ($Zn(NO_3)_2 \cdot 6H_2O$, 98%) are purchased from Acros Organics, cobalt sulfate heptahydrate ($CoSO_4 \cdot 7H_2O$) and cobalt nitrate hexahydrate ($Co(NO_3)_2 \cdot 6H_2O$) from BDH Laboratory Supplies, bacto agar gel from Difco, and N,N-dimethyl formamide (DMF) from Fisher Chemicals. All chemicals are used without further purification.

The 2-D reactors used are made from plexiglass. They have an inner-radius of 0.75 cm in the reservoir, an outer radius of 4.35 cm around the edge of the cover, and an inter-electrode radius of 3.5 cm. The circular electrodes are made using 0.5 mm cross-sectional diameter tungsten wire from Aldrich. The electric field is supplied using a ScienceWorkshop®750 interface and Data Studio software from PASCO Scientific.

2.2 Characterization of ZIF Crystals

After cleaning, the ZIF powder is ready for characterization to determine the crystal structure, morphology, size, and doping.

2.2.1 Powder X-ray Diffraction (PXRD)

Powder X-ray diffraction is a non-destructive technique used to confirm the crystal structure of the collected powder. The PXRD patterns are obtained using a Bruker D8 Advance X-ray diffractometer using CuKα radiation with λ=1.5406 Å at 40 kV and 40 mA. The scanning rate is set at 0.0200 $^\circ \cdot$ min^{-1}, and 2θ from 5° to 40°, Appendix B.

2.2.2 Scanning Electron Microscopy Analysis (SEM)

The morphology and size of the particles in each sample are determined using a Mira LMU scanning electron microscope by Tescan operating at 10 kV. Before imaging, the samples are coated with a 25 nm layer of gold using a sputtering machine, Appendix A.

To determine the average size, the particles are approximated as spheres and the diameters of 100 particles in each sample are measured using the Mira software. The errors on the measurements are reported as the error on the mean, calculated using $err = \sigma/\sqrt{N}$, where σ is the standard deviation, and N is the population size.

2.2.3 Energy-dispersive X-ray Analysis (EDX)

The ratio of cobalt to zinc incorporated into the ZIF framework of doped samples is determined using energy-dispersive X-ray analysis via the Oxford EDX detector attachment of the Mira SEM operated at 20 kV. Each sample is analyzed in three different areas; the reported values and errors are the average of the three values and the error on the mean, unless stated otherwise.

Chapter 3

Effect of an External Electric Field on the 2-D Reaction-Diffusion of ZIF-8, ZIF-67, Zn-Co Mixed-Metal ZIF-8 using Sulfate Salts

3.1 Effect on Precipitation Patterns, Size, and Morphology of ZIF-8

3.1.1 Effect on Precipitation Patterns

The ZIF-8 sulfate system precipitates periodically forming a Liesegang band pattern, which is in agreement with previously reported results [31]. As expected, the application of an external electric field alters both the distance traveled by the precipitation front and the spacing of the precipitation pattern. For the ZIF-8 system, 2-methylimidazole 2-mIm) diffuses into the gel containing the zinc(II) salt. 2-mIm has pK_a=7.8 in water, and exists in equilibrium with its protonated form, 2-mImH$^+$ [199, 200]. Imposing a positive electric field is expected to fill the gel medium with 2-mIm and deplete it from Zn^{2+} ions, shifting the bands to farther distances from the diffusion interface, Figure 3.1. A negative field is expected to have the opposite effect.

The effect on the diffusivity and the precipitation speed is illustrated by the log-log plot of the distance traveled by the precipitation front versus time, where the diffusivity is represented by the slope β, and the speed by the y-intercept, Figure 3.2. According to Gálfi and Rácz, in a diffusion-limited process, the distance traveled by the front is linearly proportional to the square root of time,

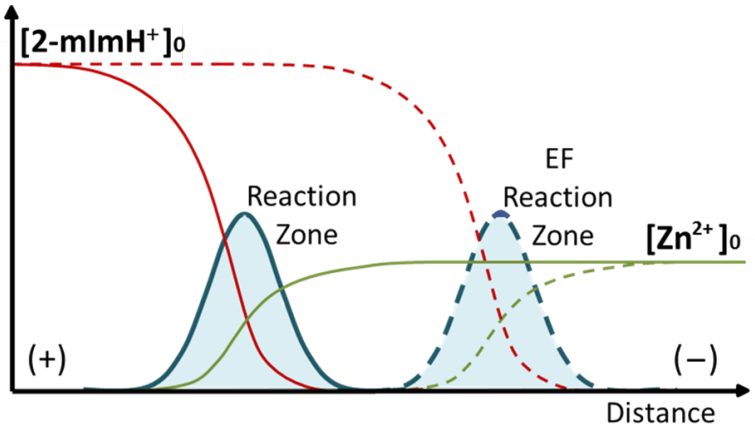

Figure 3.1: A representation of the effect of electric field on the concentration profiles for the ZIF-8 system before (solid line) and after (dashed lines) the application of a positive field.

giving $d = t^{\beta}$, where $\beta = 0.5$ [201]. The exponent of the diffusion profile β for the ZIF-8 system is extracted from the log-log fit and remains close to 0.5 with the application of a positive or negative potential difference of 2 V, which indicates that the process is diffusion-limited. The electric field has an apparent effect on the motion of the precipitation front, as shown by the shift in the y-intercept value. It increases with the application of a positive potential difference as the propagation of the front is accelerated, and decreases with the application of a negative potential difference that decelerates the front propagation.

The effect of the external electric field on the precipitation pattern is investigated using the scaling laws discussed in Chapter 1. The values of the spacing coefficient p are calculated as the slopes of the linear plots of x_{n+1} versus x_n according to eq.(1.1), and range from 0.16 upon applying -2 V, to 0.27 in the control, to 0.29 upon applying +2 V, Table 3.1a. This is a relatively small variation, but the applied potentials are low [39]. The application of positive potential differences causes migration of Zn(II) ions towards the outer electrode, accelerating the front propagation and shifting the bands further from the diffusion interface and each other resulting in a larger p value. Conversely, when negative differences are applied, Zn(II) ions migrate towards the inner electrode decelerating the front propagation and shifting the bands towards the interface and closer to each other.

The value of the width exponent α is calculated as the slope of the ln-ln fit of the bandwidth w_n versus its position x_n according to eq.(1.1.2). The width exponent decreases upon application of both positive ($\alpha = 0.59$) and negative ($\alpha = 0.94$) potential differences with respect to that of the control ($\alpha = 1.16$), which indicates that the application of a potential difference in any direction

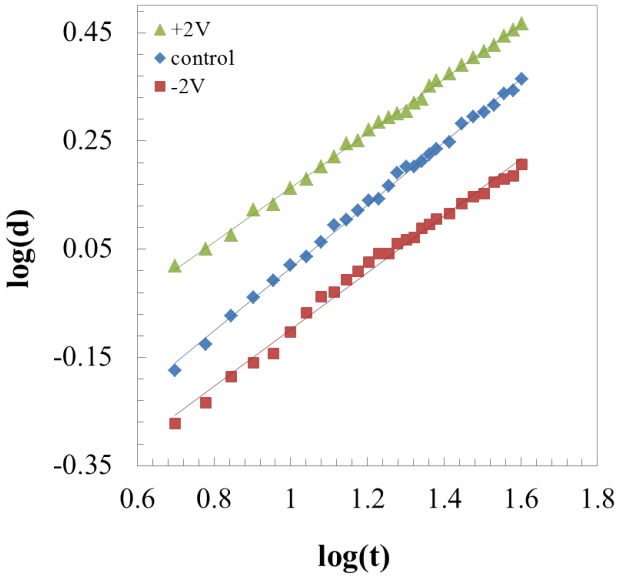

Figure 3.2: log-log plots of the distance travelled by the front vs. time. The equations of the linear fits are $y = 0.50x - 0.34$, $y = 0.57x - 0.56$, and $y = 0.51x - 0.61$ for the +2 V (green), control (blue), and -2 V (red) respectively.

	-2 V	0 V	+2 V
p	0.16±0.02	0.27±0.03	0.29±0.002
R^2	0.998	0.997	0.999

(a)

	-2 V	0 V	+2 V
α	0.94±0.064	1.16±0.06	0.59±0.005
R^2	0.973	0.996	0.972

(b)

Table 3.1: Spacing coefficient p and R^2 values of the linear fits of x_{n+1} versus x_n for the ±2 V and control reactors, table (a). Width exponent α and R^2 values of the ln-ln fits of w_n versus x_n for the ±2 V and control reactors, table (b).

reduces the bandwidth at a given distance from the diffusion interface, Table 3.1b. However, the α value for the positive field is much below 1. As mentioned in section 1.1.2, errors in the application of the width law are not uncommon, as it is difficult to decipher where a given band truly begins and ends. This is particularly the case with the reactor under the influence of +2 V, as the banding becomes less resolved. The limited number of data points that could be taken due to the short 3.5 cm reactor radius also adds to the observed error.

3.1.2 Effect on Size and Morphology

To select an effective potential difference, the experiment is first carried out in small reactors with an inter-electrode distance of 1.8 cm under potential differences varying from 0.5 V to 2 V for 24 hours. Potential differences higher than 2 V deform the gel and are excluded from the study. The Liesegang bands are well-defined and collected separately for analysis using SEM. All samples are confirmed to be ZIF-8 through PXRD analysis unless mentioned otherwise, Figure B.1 left column.

All bands collected from the control consist of polyhedral ZIF-8 particles with sizes ranging from 0.81±0.05 μm in the first band next to the interface to 0.97±0.07 μm in the last band at the diffusion front. The polyhedral shape of the ZIF-8 particles is a truncated octahedron; this will not change throughout the thesis work and will simply be referred to as polyhedron. The application of positive potentials leads to the gradual decrease in particle size, which is most defined at +2 V, with a 35% decrease in the first band and 40% decrease in the last band, Figure 3.3. The change in size could be attributed to the faster diffusion at +2V, Figure3.2, which hinders the growth process of the precipitated particles. On the other hand, the application of negative potential differences has little to no effect on particle size, Figure 3.3.

The experiment is then performed using the bigger reactors with an inter-electrode distance of 3.5 cm for 7 days at a potential difference of ±2 V, as it is found to have the most significant effect on the precipitate. The precipitation pattern is less defined in the big reactors, thus the samples are collected by sections of 0.5 cm zones, that will be referred to as bands. The effect is similar to that in the small reactors, with a 43-55% decrease in size in the samples subjected to +2 V, while a negligible effect is observed at -2 V, Figure 3.4.

The change in size is accompanied by a change in morphology in both reactor sizes. The first band near the interface consists of smooth polyhedra in all experiments. Their morphology is affected by the presence of +2 V in bands further from the interface as polyhedra with rugged surface start to form. Upon applying negative potential, the smoothness of the particles‘ surface is maintained. How-

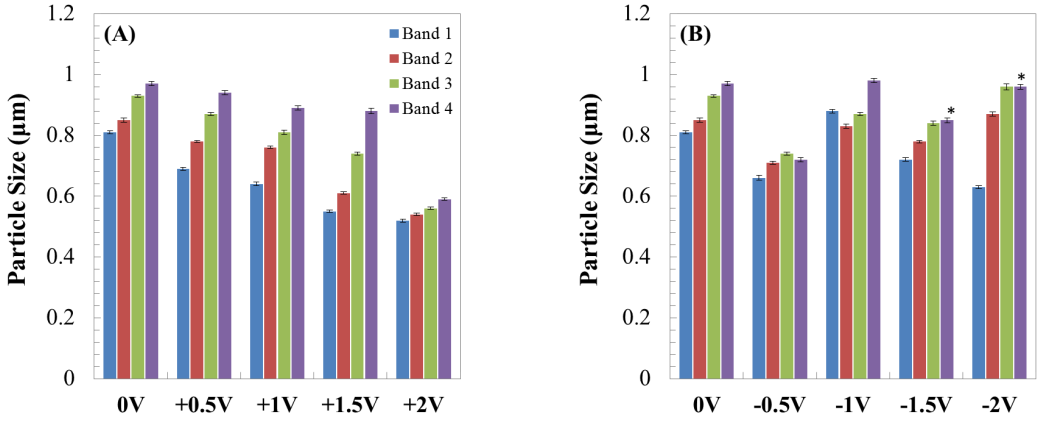

Figure 3.3: Bar graphs representing the effect of varying the positive (A) and negative (B) potential difference from 0.0 to 2.0 V on polyhedral particle size in the four leading bands using the small reactors. Samples containing the spherical co-precipitate are marked by an asterisk (*).

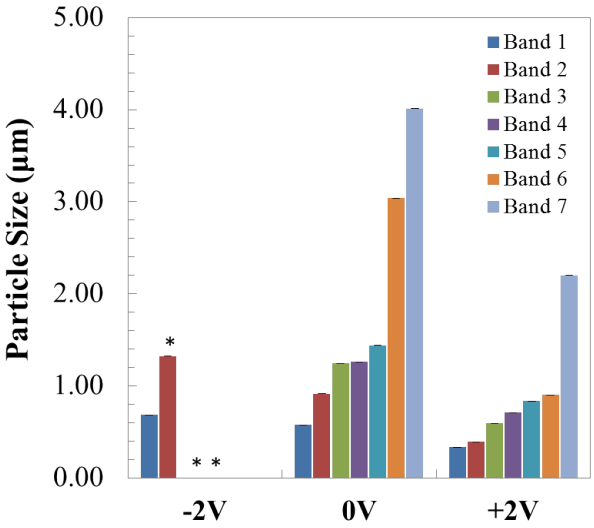

Figure 3.4: Bar graphs representing the effect of ±2.0 V on polyhedral particle size across the large reactors. Samples containing the spherical co-precipitate are marked by an asterisk (*).

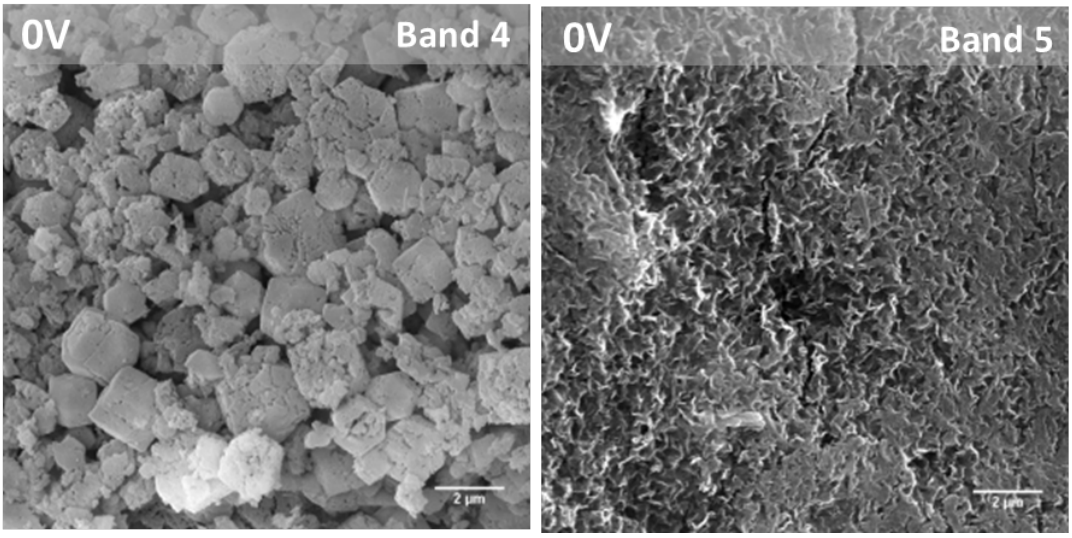

Figure 3.5: SEM micrographs of bands in the control plate that show the change from polyhedral ZIF-67 in the fourth band (left) to the flake-like particles in the darker precipitation zone (right).

ever, a spherical co-precipitate forms in bands far from the interface, Figure A.2. The PXRD profile of the spherical particles shows a prominent peak at 2θ=11.2°, Figure B.1(iii), and is comparable to the spectrum of an unidentified complex that forms when the molar ratio of 2-mIm:Zn(II) is less than 2:1 [202, 203].

3.2 Effect on Size and Morphology of ZIF-67

The ZIF-67 system precipitates continuously, and is collected in 0.5 cm "bands". In line with previous results, the control precipitates in two adjacent zones [31]; the first 2 cm consist of polyhedral ZIF-67, while the following darker zone consists of flake-like particles, Figure 3.5. The PXRD pattern of the second phase is that of the background, with a wide band at around 15°, indicating that the precipitate is amorphous, Figure B.2. The application of -2 V brings an early onset of the second phase at 1.5 cm, while precipitation is completely suppressed by the application of an external electric field of +2 V.

The particle size in the control dish ranges from 0.79±0.01 μm in band 1 to 1.81±0.03 μm in band 4. The dish subjected to -2 V features a similar size distribution but in a smaller spacial range, with sizes ranging from 0.69±0.01 μm in band 1 to 1.68±0.02 μm in band 2, Figure 3.7. Comparing the morphology of samples of similar size reveals that the application of negative potential differences encourages the formation of smoother and more uniform polyhedra, Figure 3.6.

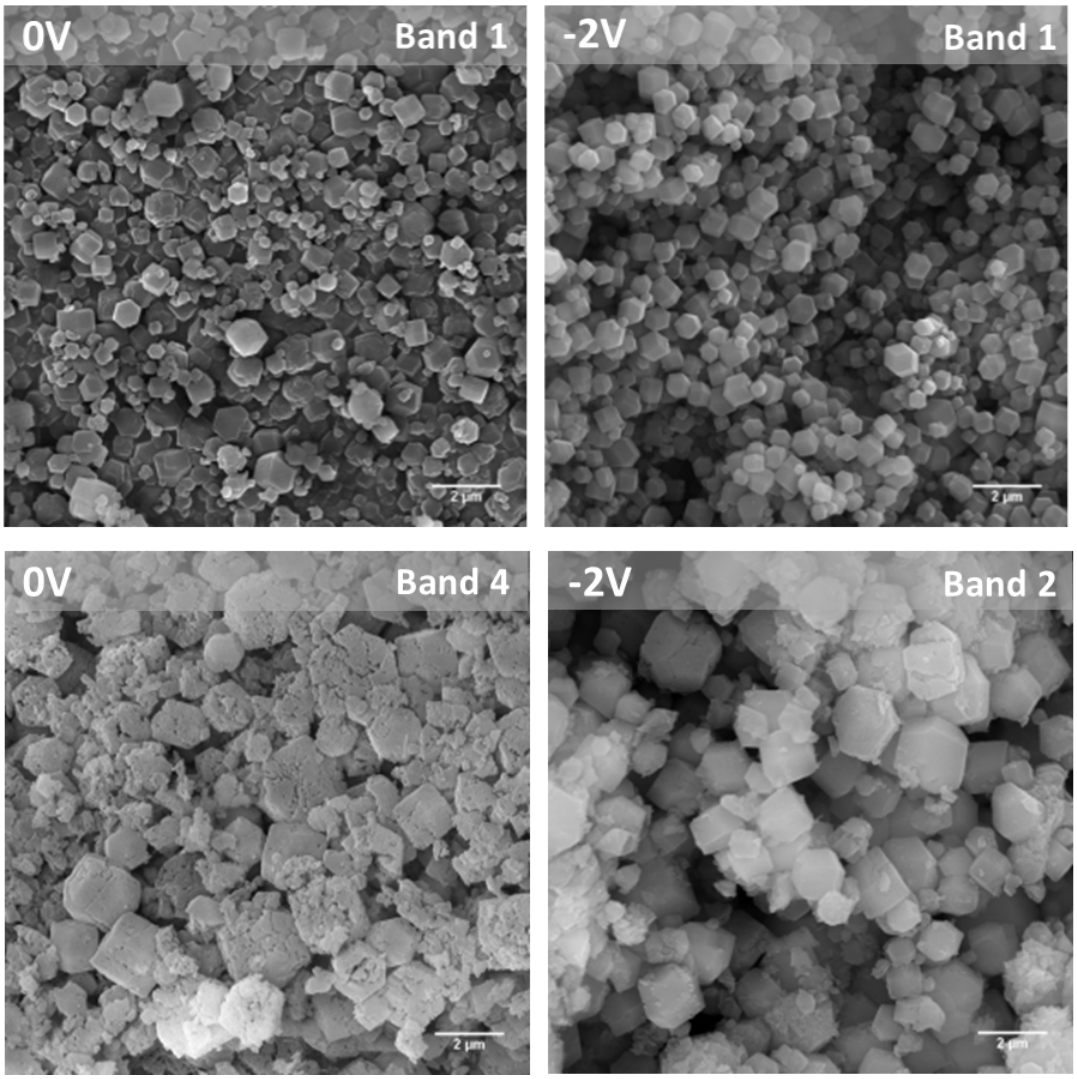

Figure 3.6: SEM micrographs comparing the morphology of the ZIF-67 polyhedra precipitated in bands 1 and 4 in the control plate to those of similar size in the -2 V reactor at bands 1 and 2 respectively.

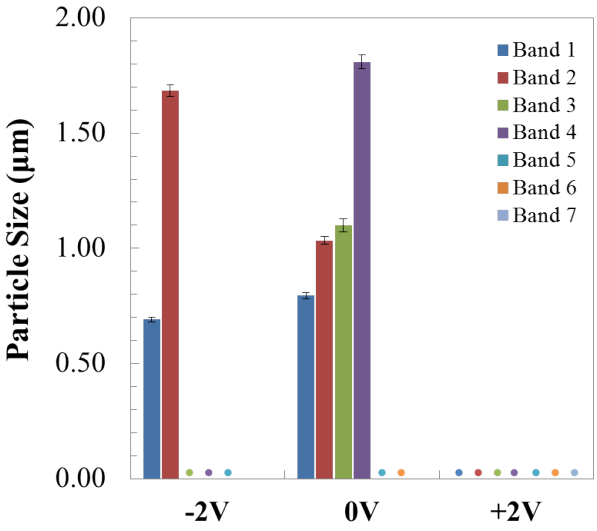

Figure 3.7: The effect of the application of ±2.0 V on ZIF-67 polyhedral particle size. The bullets represent the precipitation areas of the flake-like particles.

3.3 Effect on Zn-Co Mixed-Metal ZIF-8

To study the effect of an external electric field on the doping of ZIF-8 with cobalt, the percentage of dopant incorporated into the framework under the influence of ±2 V is monitored. Precursor solutions with inner compositions of 10, 20, 30, 40, and 50% cobalt are used. The experiment is carried out in the large reactors and allowed to propagate for 7 days. The systems precipitate in an indistinct Liesegang pattern and are collected using two methods, Figure 3.8. In the first method (M1), the precipitated area is divided into four quarters; since the electric field influences the extent of precipitate propagation, this allows for comparing cobalt incorporation at similar relative distance traveled in all plates. In the second method (M2), the precipitate is collected in 0.5 cm "bands", which allows for monitoring cobalt incorporation at set distances from the interface and also illustrates the effect on precipitation speed, Figure 3.11. The samples are washed before characterization by EDX for elemental analysis. All samples that do not contain the spherical co-precipitate are confirmed by PXRD as ZIF-8, Figure B.3 left column.

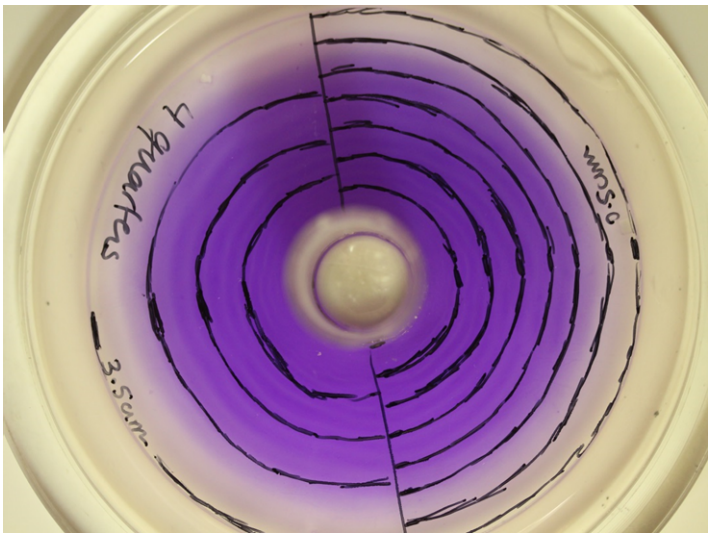

Figure 3.8: The two collection methods used with doped samples. Method 1 (left) divides the precipitated area into quarters; method 2 (right) divides it into 0.5 cm "bands" .

3.3.1 Effect on Size and Morphology

The effect on the morphology of Co-doped ZIF-8 synthesized under the influence of -2 V is similar to that of ZIF-8, where polyhedra are formed in addition to the spherical co-precipitate starting with the second quarter. As for positive potential differences, the formation of polyhedra is affected. In reactors with cobalt concentrations higher than 30%, the positive potential difference suppresses the formation of polyhedra and leads to the precipitation of particles with undefined morphology in the first quarter. The polyhedra start to appear in areas closer to the front.

The effect on the size of Co-doped ZIF-8 is similar to that in ZIF-8. The application of -2 V has little effect, while the application of +2 V leads to a decrease in particle size. In the first quarter, size is reduced by a factor of 0.69 and 0.50 in the 10 and 20% cobalt precursor solution reactors respectively. A decrease in the size of particles in the second quarter by a factor of 0.72, 0.37, and 0.37 is noted in the 30, 40, and 50% reactors respectively, Figure 3.9.

3.3.2 Effect on Cobalt Incorporation

The external electric field has a significant effect on the incorporation of cobalt into the ZIF-8 framework. In general, a negative potential difference induces an increase in the incorporation of cobalt near the interface, while a positive

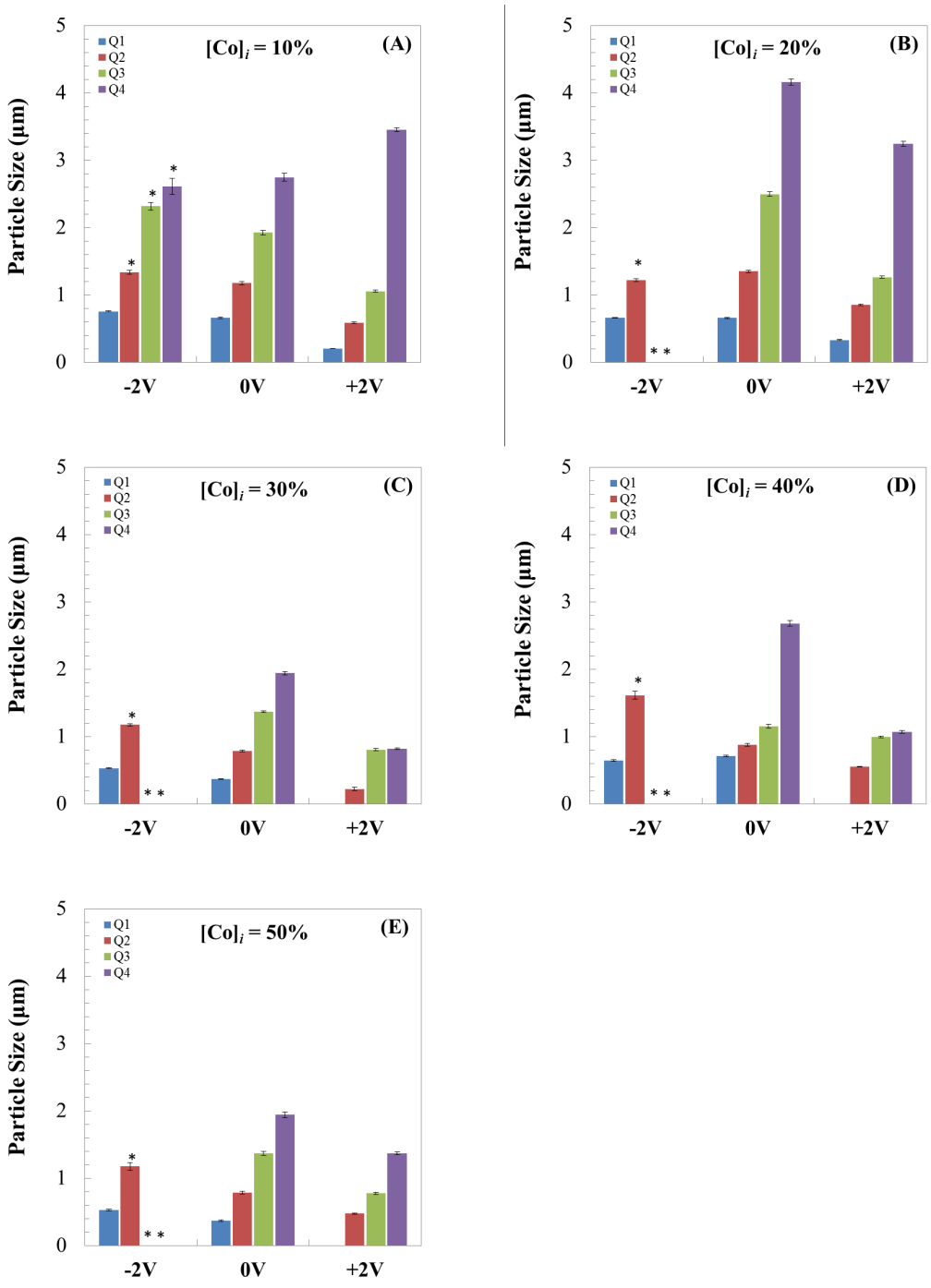

Figure 3.9: Bar graphs representing the effect of ±2.0 V on polyhedral particle size in the reactors with cobalt concentrations of 10% (A), 20% (B), 30% (C), 40% (D), and 50% (E). Samples containing the spherical co-precipitate are marked by an asterisk (*).

potential induces its decrease across the reactor.

This trend is most significant in the first quarter of the precipitated area using collection method M1, fig 3.10, and in the first two bands using collection method M2. Upon applying -2 V, the percentage of cobalt incorporated into the framework in the first quarter increases from ∼8 to 16% in the 10% Co precursor solution, from ∼18 to 24% in the 20% Co solution, from ∼24 to 34% in the 30% Co solution, from ∼35 to 46% in the 40% Co solution, and from ∼53 to 63% in the 50% Co solution. On the other hand, with the application of +2 V, the amount of incorporated cobalt decreases from ∼8 to 6% in the 10% Co precursor solution, from ∼18 to 7% in the 20% Co solution, from ∼24 to 11% in the 30% Co solution, from ∼35 to 26% in the 40% Co solution, and from ∼53 to 3% in the 50% Co solution.

In the areas beyond the first quarter, the trend is less apparent due to fluctuations in the percentage of incorporated cobalt in both the control and experimental reactors. This is characteristic of the sulfate system [204] and is more apparent in the second collection method, Figure 3.11. Moreover, the first quarter exclusively consists of ZIF-8 polyhedra in the control and -2 V samples, which further highlights the importance of the effect on cobalt incorporation in this area.

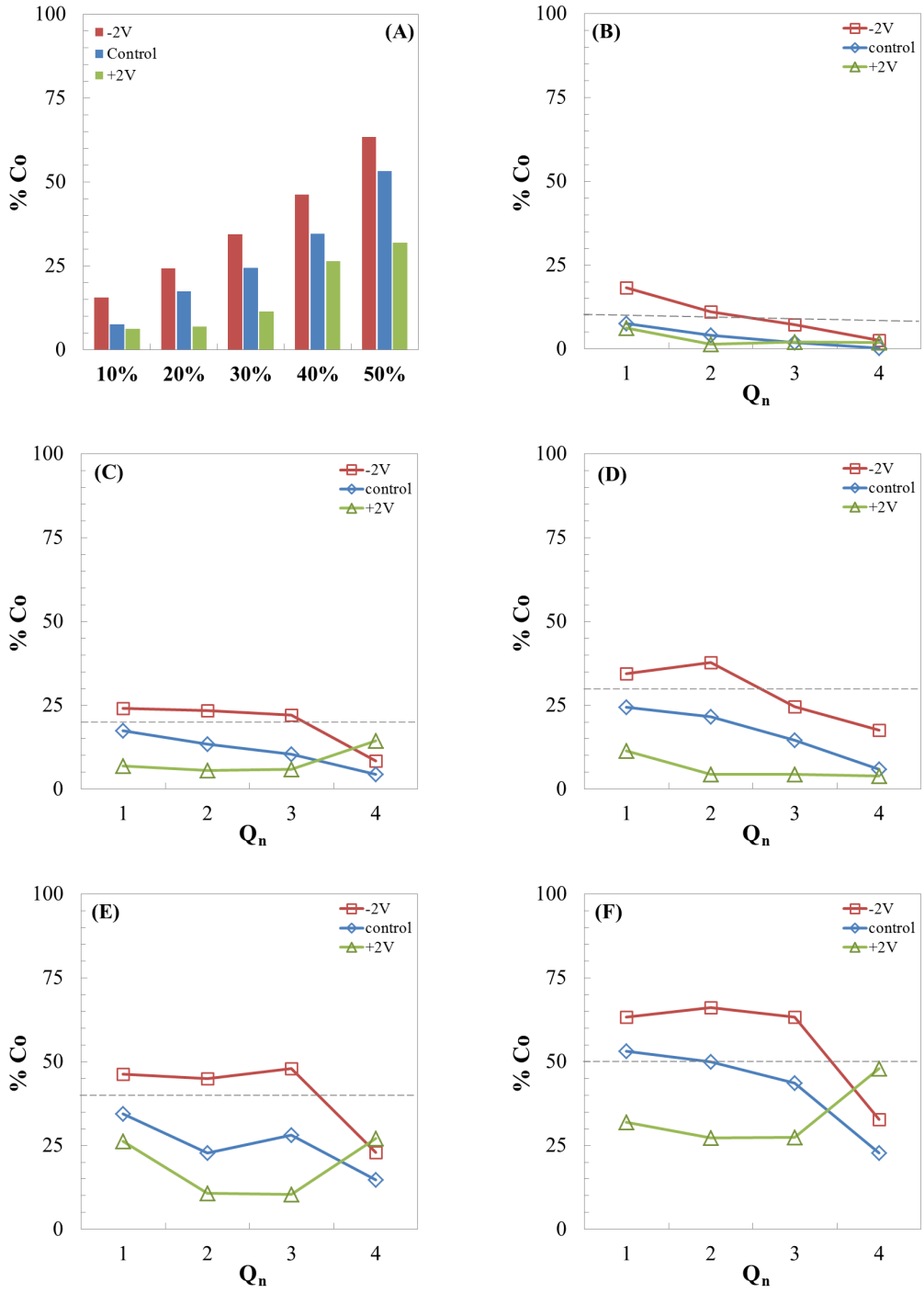

Figure 3.10: Plots displaying the effect of electric field on the percentage of cobalt incorporated into the ZIF-8 framework using the quarter collection method. The bar graph (A) shows the effect on the first quarter across the different precursor solutions. The plots (B) through (F) show the distribution of cobalt across the reactors for the 10%, 20%, 30%, 40%, and 50% precursor solutions respectively.

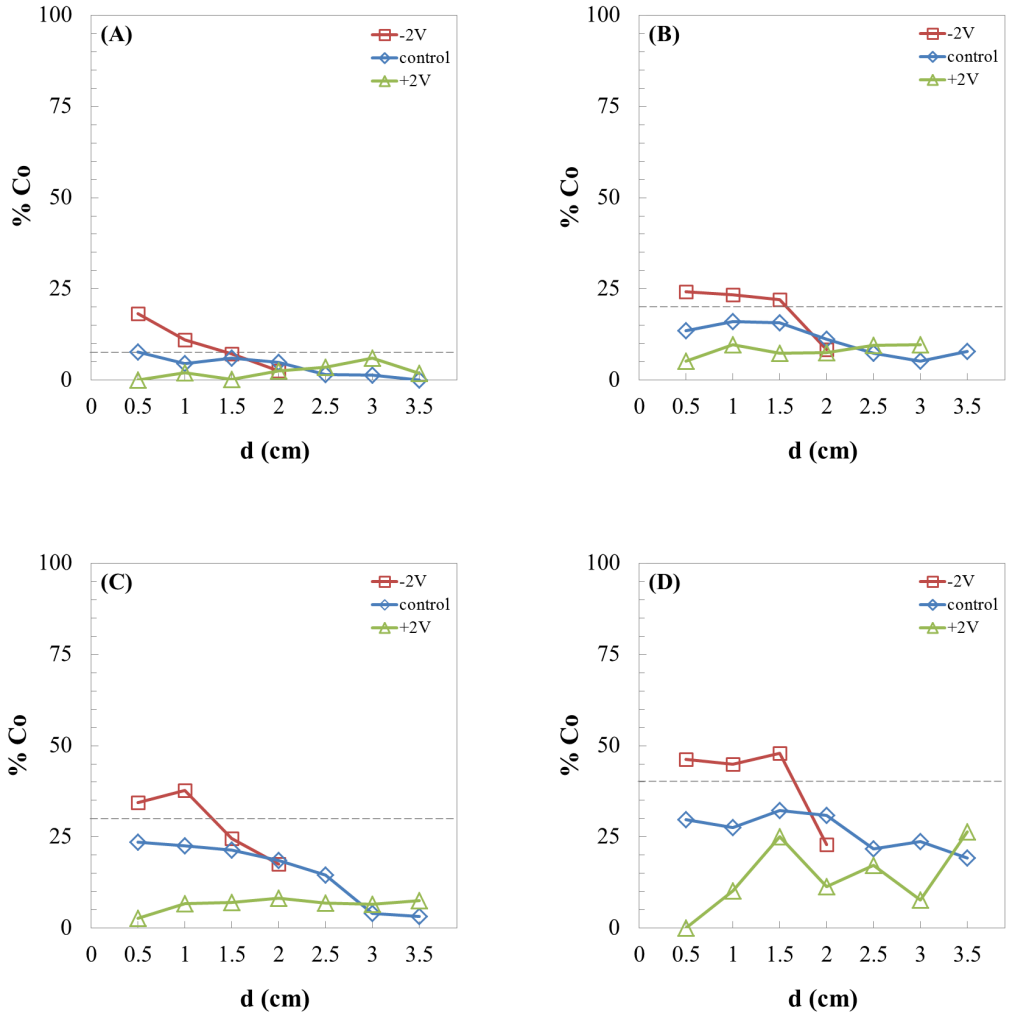

Figure 3.11: Plots displaying the effect of electric field on the percentage of cobalt incorporated into the ZIF-8 framework using the 0.5 cm band collection method. The plots (A) through (D) show the distribution of cobalt across the reactors for the 10%, 20%, 30%, and 40% precursor solutions respectively.

Chapter 4

Effect of an External Electric Field on the 2-D Reaction-Diffusion of ZIF-8, ZIF-67, and Zn-Co Mixed-Metal ZIF-8 using Nitrate Salts

Changing the anion of the metal salt used in the reaction-diffusion process could affect the precipitation pattern formed, the morphology of the crystals, and their doping [31, 114, 113]. In the case of the one-dimensional reaction-diffusion of ZIF-8, using nitrate salts results in continuous precipitation, as opposed to the Liesegang banding observed in the sulfate system. The cobalt incorporation in doped ZIF-8 is also affected, where the percentage of cobalt in the framework decreases gradually as particles precipitate further from the interface [114]. The metal precursor also affects the morphology and growth process of ZIFs in general [131, 132].

4.1 Effect on Precipitation Patterns, Size, and Morphology of ZIF-8

4.1.1 Effect on Precipitation Patterns

The ZIF-8 nitrate system precipitates continuously in 2-D, as with the 1-D system [114]. The difference in the patterns of the nitrate and sulfate systems might be due to the pH difference between the two salt solutions. The slightly more basic

property of the sulfate inner could encourage the deprotonation of the $[Zn(2\text{-}mIm)_2]^2+$ complex that leads to ZIF formation, leading to more consumption of the diffusing 2-mIm than in the nitrate system, which could in turn lead to band formation. The experiment is carried out in the large reactors and allowed to propagate for 4 days. As expected, the application of an external electric field alters the distance traveled by the precipitation front. The exponent of the diffusion profile β is extracted from the log-log plot of the distance traveled by the precipitation front versus time and remains close to 0.5 with the application of a positive or negative potential difference of 2 V, which indicates that the process is diffusion-limited, Figure 4.1. The effect of the electric field on the motion of the precipitation front is similar to the sulfate system, as shown by the shift in the y-intercept value. It increases with the application of a positive potential difference as the propagation of the front is accelerated, and decreases with the application of a negative potential difference that decelerates the front propagation.

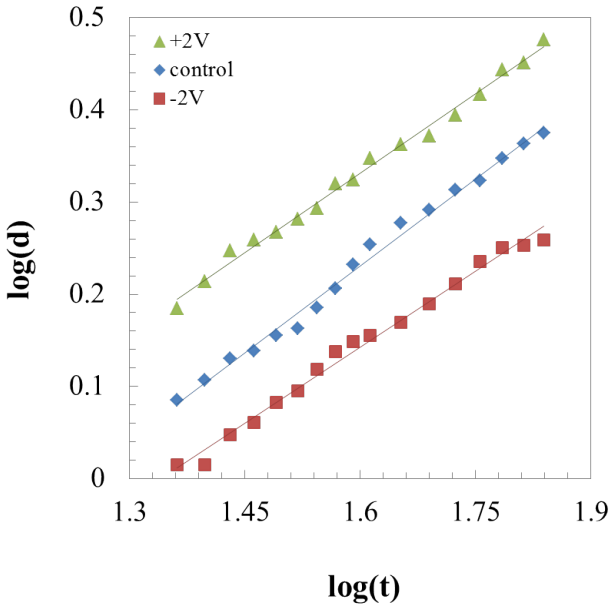

Figure 4.1: log-log plots of the distance travelled by the front vs. time. The equations of the linear fits are $y = 0.57x - 0.58$, $y = 0.62x - 0.72$, and $y = 0.53x - 0.76$ for the +2 V (green), control (blue), and -2 V (red) respectively.

4.1.2 Effect on Size and Morphology

To study the effect on particle size and morphology, the precipitate is collected in 0.5 cm "bands" for analysis using SEM. All samples are confirmed to be ZIF-8 through PXRD analysis unless mentioned otherwise, Figure B.1 right column. Unlike the sulfate system, all bands collected from the control dish in the nitrate system consist of a mixture of smooth and rugged polyhedral ZIF-8. The amount of smooth polyhedra decreases in bands collected further from the interface. The ZIF-8 particle size ranges from 0.55±0.01 μm in the first band next to the interface to 1.52±0.03 μm in the last band at the diffusion front. The application of positive potentials leads to a slight decrease in particle size, which is most noticeable in the first band at a 34% decrease, Figure 4.2. On the other hand, the application of negative potential differences leads to the increase in particle size, which is also most noticeable in the first band, which contains particles of average size 1.09±0.01 μm, almost twice the size of those in the control, Figure 4.2.

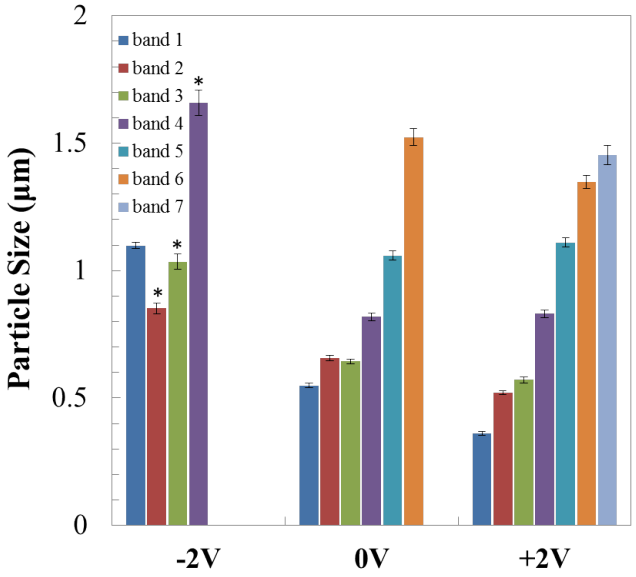

Figure 4.2: Bar graphs representing the effect of ±2.0 V on polyhedral particle size across the reactors. Samples containing the spherical co-precipitate are marked by an asterisk (*).

While the application of a positive potential difference does not have an apparent effect on morphology, negative potential affects both the size and the morphology of the precipitated particles. This is apparent by comparing the particles in the first band of each plate, where bigger particles are formed at -2 V,

Figure 4.3 top. The observed effect on the particle size is similar to that of increasing the concentration of the inner electrolyte [205], since under the influence of a negative field, the metal ions migrate towards the inner electrode, raising the local concentration. The effect on morphology is shown by comparing the first band in the plate subjected to -2 V with samples of similar size in the other two plates, revealing the formation of smoother and more uniform polyhedra with a narrower size distribution in the -2 V sample, Figure 4.3 bottom. Furthermore, band 2 in the -2 V plate is the only sample containing smooth ZIF-8 polyhedra exclusively, however, it also marks the onset of the spherical co-precipitate as seen with the sulfate system. The PXRD profile of the spherical particles is identical to that of the co-precipitate in the sulfate system, Figure B.1(vi).

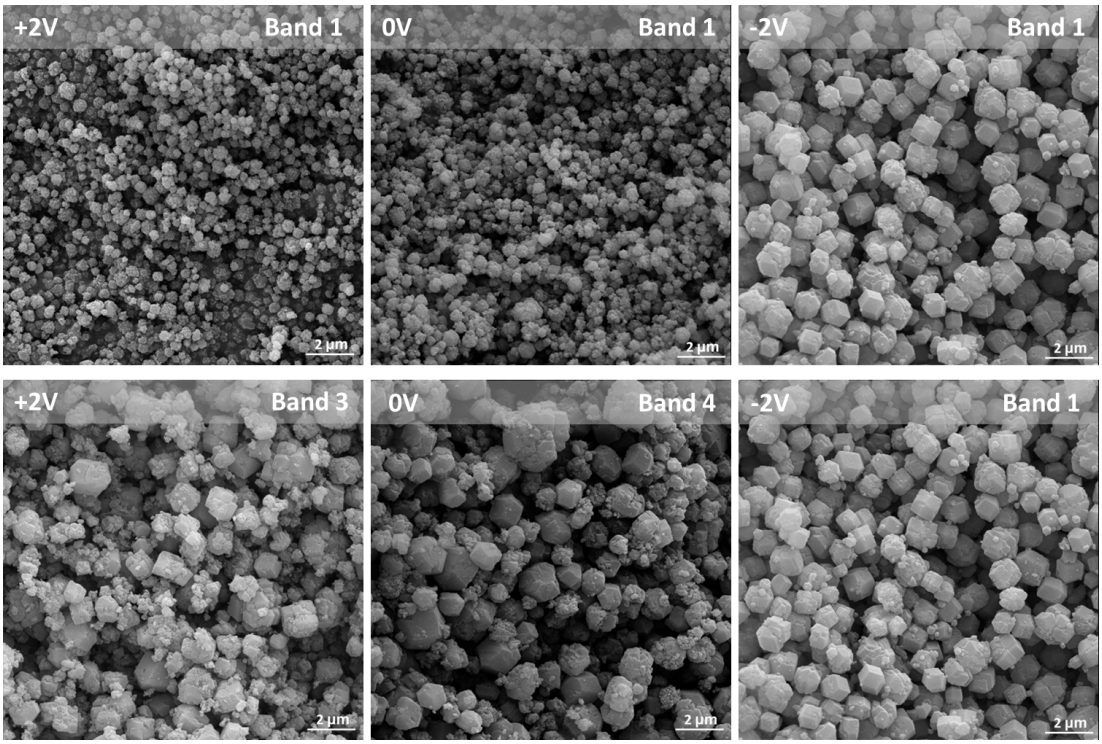

Figure 4.3: SEM micrographs comparing the morphology of the ZIF-8 polyhedra precipitated in the first band of each plate (top), and bands 3 and 4 and 1 in the +2 V, control, and -2 V plates, respectively, which are of similar size (bottom).

4.2 Effect on Size and Morphology of ZIF-67

The ZIF-67 system precipitates continuously, and is collected in 0.5 cm "bands". The experiment is carried out in the large reactors and allowed to propagate for 4 days. All bands collected from the control consist of polyhedral ZIF-8 particles

with sizes ranging from 1.50±0.09 μm in the first band next to the interface to 10.5±0.2 μm in the last band. The application of -2 V leads to the precipitation of a second phase at 1.5 cm, while precipitation is completely suppressed by the application of an external electric field of +2 V. As with the sulfate system, the dish subjected to -2 V features a similar size distribution to that in the control but in a smaller spacial range. This is most apparent in the first band, with an average particle size of 1.00±0.02 μm in band 1, Figure 4.4, Figure 4.5.

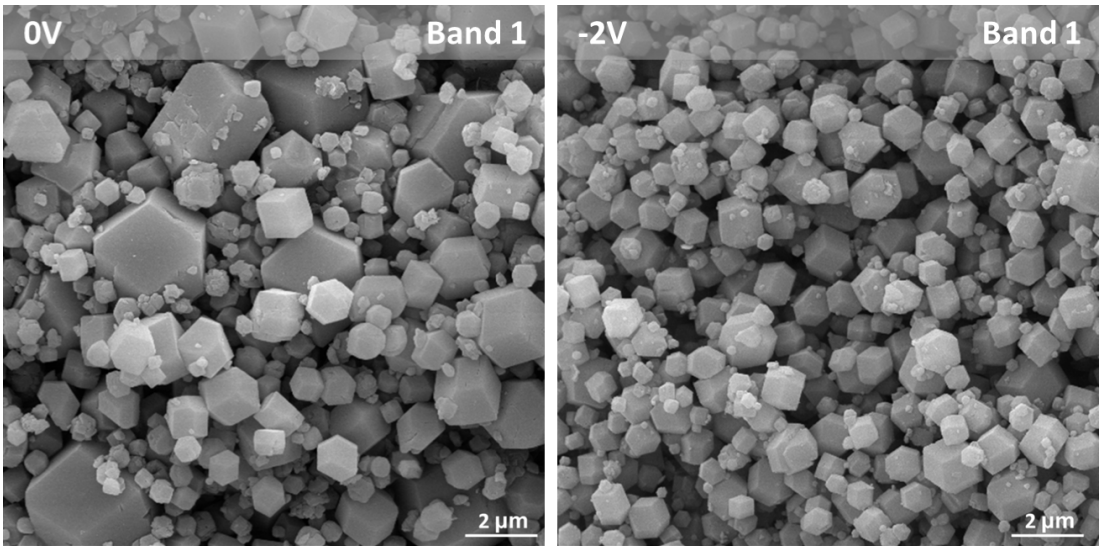

Figure 4.4: SEM micrographs comparing the size distributions of the ZIF-67 polyhedra precipitated in band 1 of each the control and -2 V dishes. The samples have similar morphology and average size but the sample from the control plate has a much wider size distribution.

4.3 Effect on Zn-Co Mixed-Metal ZIF-8

To study the effect of an external electric field on the doping of ZIF-8 with cobalt, the percentage of dopant incorporated into the framework under the influence of ±2 V is monitored. Precursor solutions with inner compositions of 25, 50, and 75% cobalt are used. The experiment is carried out in the large reactors and allowed to propagate for 4 days. The systems precipitate continuously and are collected using the same two methods used with the sulfate system, Figure 3.8. The samples are washed before characterization by EDX for elemental analysis. All samples that do not contain the spherical co-precipitate are confirmed by PXRD as ZIF-8, Figure B.3 right column.

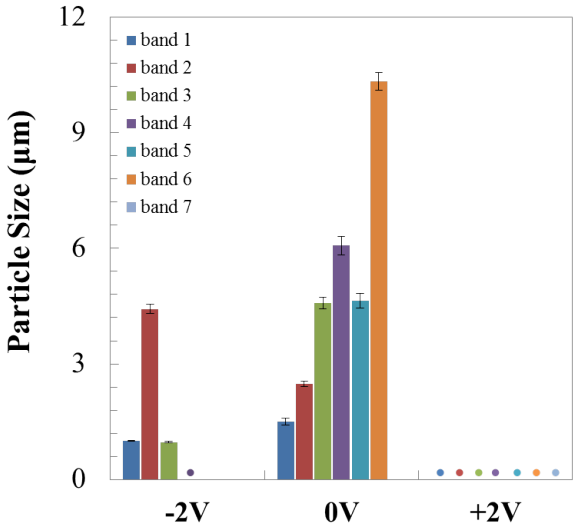

Figure 4.5: The effect of the application of ±2.0 V on ZIF-67 polyhedral particle size. The bullets represent the precipitation areas of the flake-like particles.

4.3.1 Effect on Size and Morphology

The effect on the morphology of Co-doped ZIF-8 synthesized under the influence of ±2 V is similar to that of ZIF-8. The plates subjected to +2 V are similar to the control plates; all contain a mixture of rugged and smooth polyhedra throughout. The application of -2 V encourages the formation of smooth polyhedra near the interface in addition to the spherical co-precipitate starting with the second quarter, Figure 4.6.

The effect on the size of Co-doped ZIF-8 is similar to that in ZIF-8. The application of +2 V has little effect, while the application of -2 V leads to an increase in particle size. In the first quarter, size increases by a factor of 1.52, 1.78, and 1.50 in the 25, 50, and 75% cobalt precursor solution reactors respectively, Figure 4.7.

Unlike in the 1-D reaction-diffusion of Co-doped ZIF-8 using nitrate salts, there is no relation between cobalt incorporation and particle size [114]. The average particle size in a given section of a plate is similar across all precursor solutions for the same experimental condition. For example, the average particle size for the first quarter in the three plates subjected to -2 V is 0.74 μm with a standard deviation of 0.07 μmm and that in the second quarter is 0.91 μm with

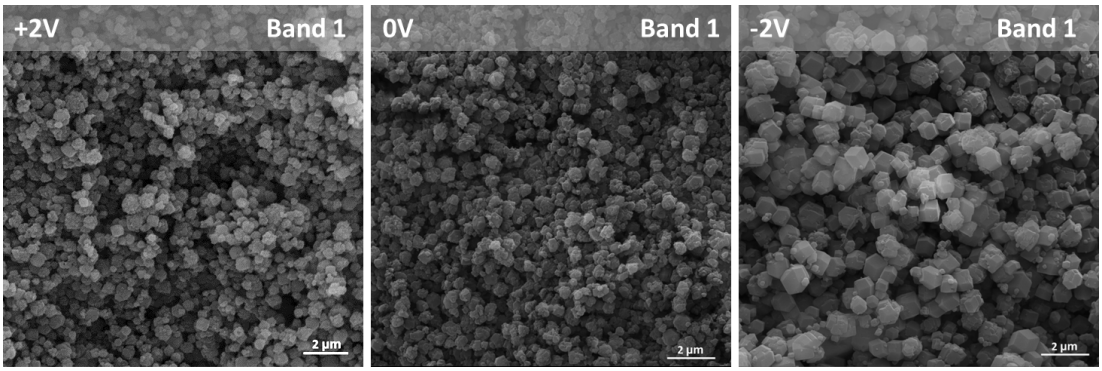

Figure 4.6: SEM micrographs comparing the morphology of the Co-doped ZIF-8 polyhedra precipitated in the first band in of each plate with 25% Co inner electrolyte concentration.

a standard deviation of 0.08 μm; the relative standard deviation for both bands is 9%.

4.3.2 Effect on Cobalt Incorporation

The Co gradient effect in the doped systems observed in 1D is maintained in 2-D reaction-diffusion. Upon application of ± 2 V, the external electric field has an effect on the incorporation of cobalt into the ZIF-8 framework. The same trend is evident in the 25 and 50% Co reactors, where more cobalt is incorporated into the system under the influence of -2 V, and less is incorporated under the influence of $+2$ V. Applying negative field to the 75% Co reactor has no effect on the incorporated cobalt, but the same trend as before is observed with application of positive field, Figure 4.8

This trend is most significant in the first two quarters of the precipitated area using collection method M1, fig 3.10, and in the first two bands using collection method M2. Upon applying -2 V, the percentage of cobalt incorporated into the framework in the first quarter increases from $\sim$21 to 36% in the 25% Co precursor solution, and from $\sim$48 to 61% in the 50% Co solution. On the other hand, with the application of $+2$ V, the amount of incorporated cobalt decreases from $\sim$21 to 16% in the 25% Co precursor solution, from $\sim$48 to 39% in the 50% Co solution, and from $\sim$82 to 62% in the 75% Co solution.

The 25% Co system is chosen for the remaining studies, as the effect of the electric field on both cobalt incorporation and morphology is more pronounced than with higher cobalt concentrations. It is also convenient because even under the influence of -2 V, the ratio of zinc to cobalt incorporated into the system remains greater than one.

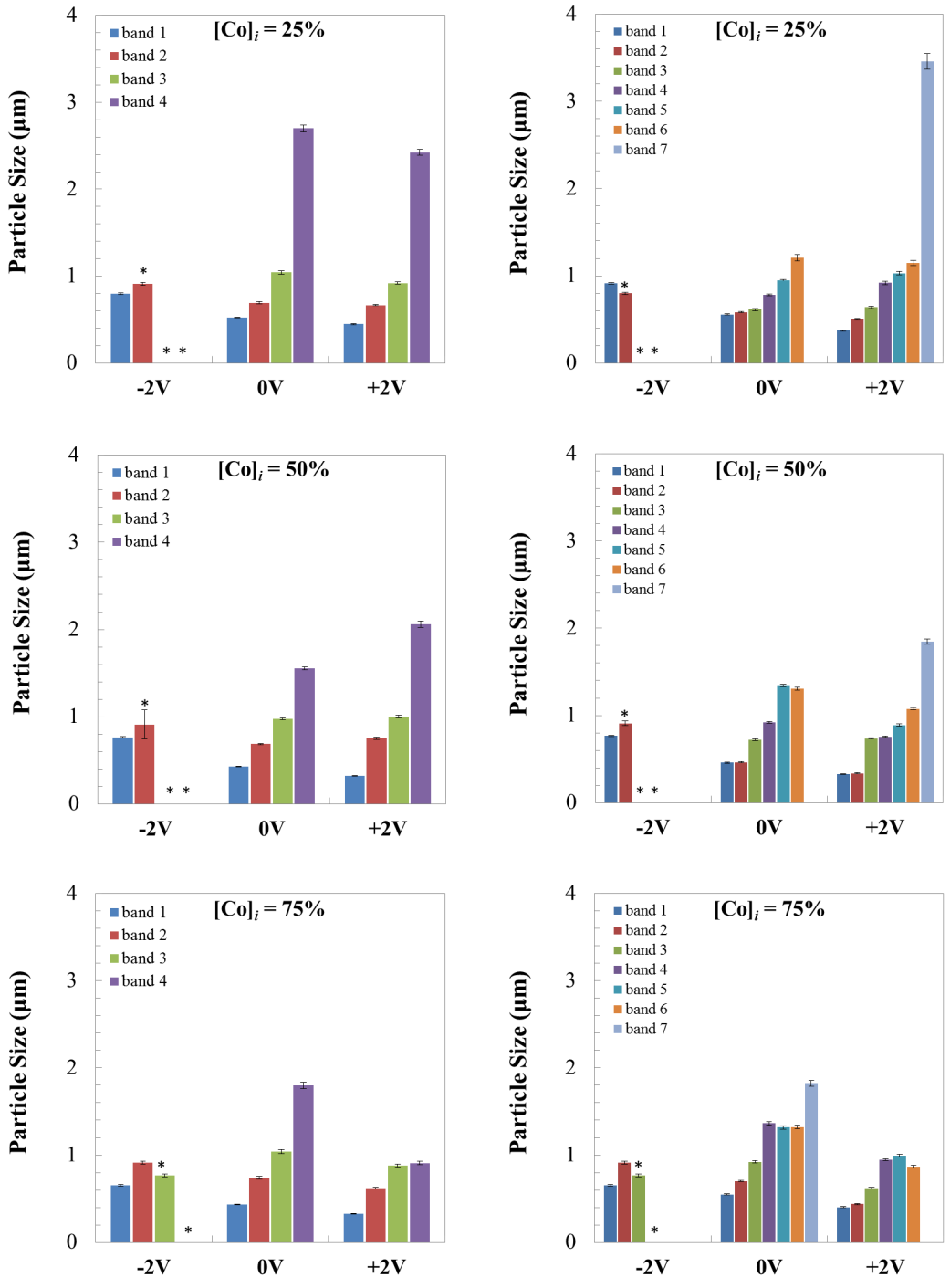

Figure 4.7: Bar graphs representing the effect of ±2.0 V on polyhedral particle size in the reactors with cobalt concentrations of 25, 50, and 75%, using both collection method 1 (left column) and method 2 (right column). Samples containing the spherical co-precipitate are marked by an asterisk (*).

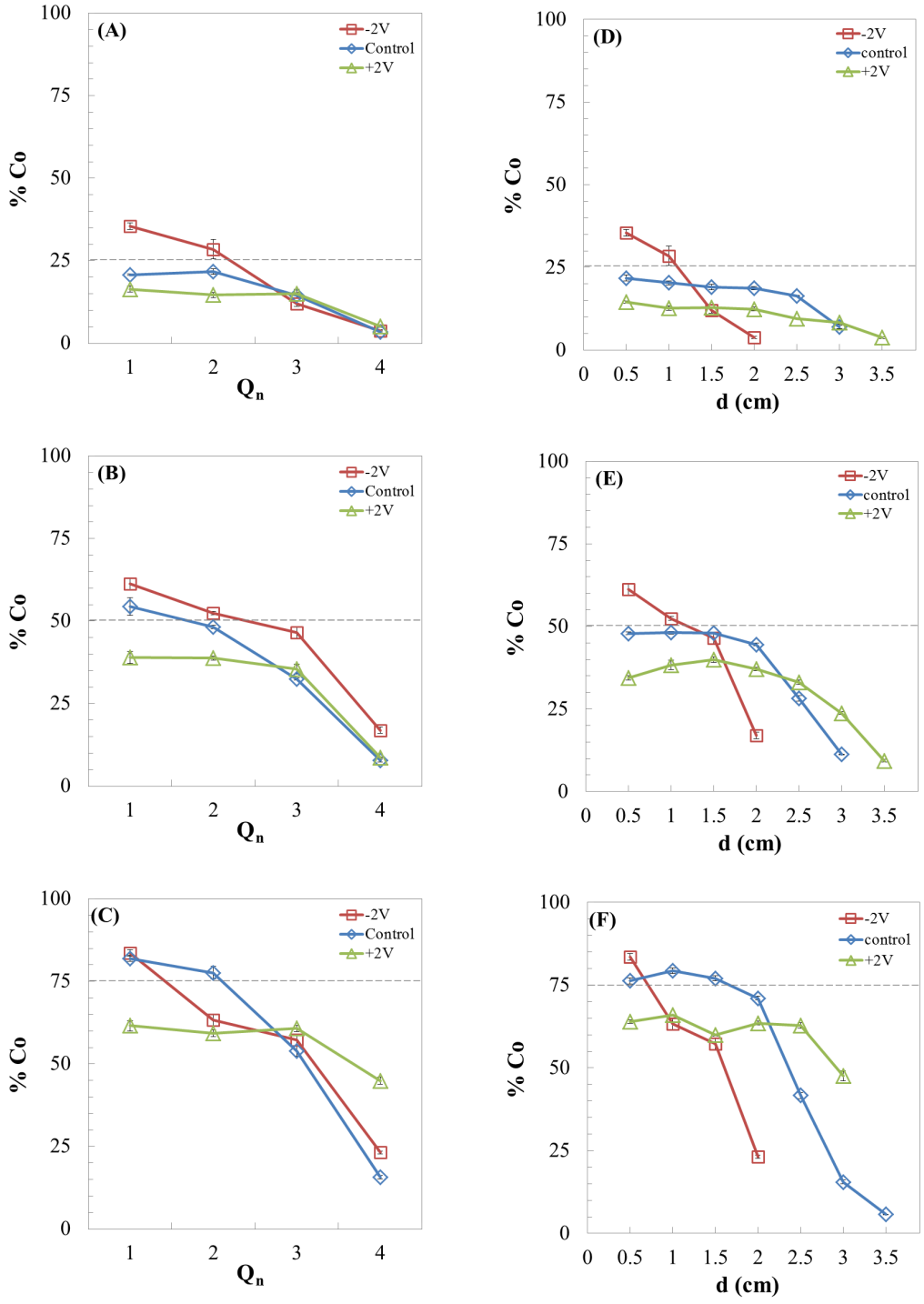

Figure 4.8: Plots displaying the effect of electric field on the percentage of cobalt incorporated into the ZIF-8 framework. Plots (A), (B), and (C) show the distribution of cobalt across the reactors for the 25%, 50%,and 75% precursor solutions respectively using the quarter collection method. Plots (D), (E), and (F) show the cobalt distribution using the band collection method.

4.3.3 Reproducibility Studies

To test the reproducibility of the results of the doped system, triplicates are prepared from the same batch and allowed to gelate then propagate under the same conditions for 4 days. Both collection methods are used, and the average percent of incorporated cobalt, the standard deviation, and the relative standard variation (RSD) are calculated for each sample in the ±2 V and control plates. Figure 4.9a. The relative standard deviation remains lower than 10% in the first three bands and the first three quarters in all reactors, but increases towards the propagation front. The particle mythologies are similar in the three plates of each set; All control samples contain a mixture of smooth and rugged polyhedra, the first quarter in the three -2 V plates consists of smooth polyhedra, with the spherical co-precipitate appearing staring the second quarter, and the morphology in the +2 V plates is mostly unaffected, Figures A.17 A.18 A.19.

The experiment is then performed three times on three consecutive weeks to test the repeatability using different batches, Figure 4.9b. Both collection methods are used, and the average percent of incorporated cobalt, the standard deviation, and the relative standard variation are calculated for each sample. The general trend of increasing cobalt incorporation in the -2 V samples and decreasing incorporation in the +2 V samples is observed in all three batches. However, the RSD is higher than in the reproducibility study, with values around 12% for the first quarter of the -2 V, +2 V, and 0V samples, and increasing towards the propagation front. The effect on particle mythologies is similar in the three plates; +2 V shows no effect, while -2 V increases the number of smooth polyhedra near the interface and induces the formation of the co-precipitate near the front, Figures A.20 A.21 A.22. A new box of Bacto agar gel from the same manufacturer was used for the third batch, which affected the morphology of the particles in all samples in both control and experimental plates, Figure A.22.

4.3.4 Effect of Potential Difference Magnitude on Cobalt Incorporation

The experiment is repeated using the 25% Co system under the influence of ±1 V and ±1.5 V, and compared to the results obtained under ±2 V. The application of ±1 V does not affect the cobalt incorporation, the propagation of the front, or the morphology. The effect of the application of ±1.5 V is similar to that of ±2 V in the first two bands and quarters, Figure 4.10. The application of -1.5 V leads to the reduction of the propagation distance from 3 cm to 2 cm, and to the increase in cobalt incorporation from 25% to 33% in the first band. The application of +1.5 V leads to the extension of the propagation front to 3.5 cm, and the reduction in cobalt incorporation to 14% in the first band.

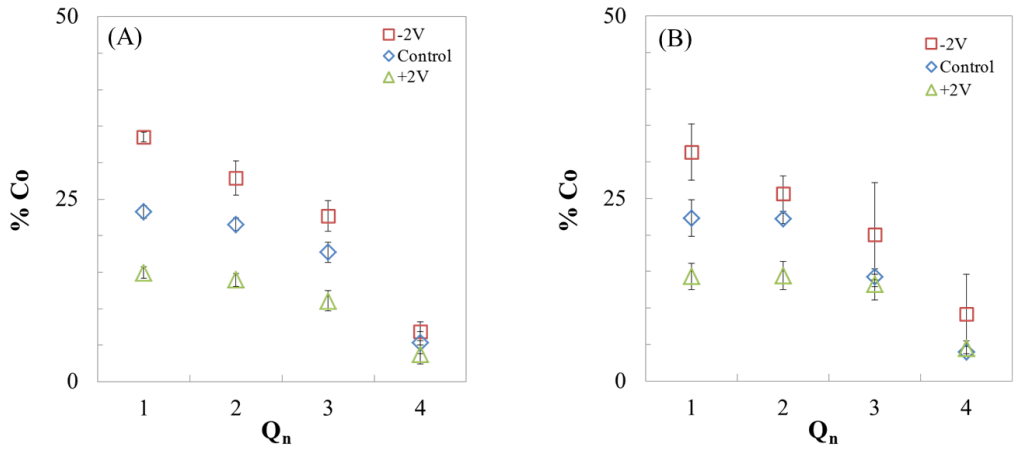

Figure 4.9: Plots of the calculated average %Co incorporated (Av) , and average standard deviation (SD) of the samples in the -2 V, control, and +2 V plates of the same-batch reproducibility (A) and different-batch repeatability (B) studies calculated using the quarter collection method.

4.3.5 Time Study on the Morphology and Cobalt Incorporation

The time study is performed to gain insight into the mechanism of cobalt incorporation into the ZIF-8 framework under the influence of an external electric field. Cobalt-doped ZIF-8 is synthesized in the big reactors using a 25%Co precursor solution, is subjected to ±2 V, and allowed to react for 1, 2, 3, and 4 days before extraction cleaning and characterization by EDX. All samples are collected using the 0.5 cm band method.

In all the Co-doped systems, the white ZIF-8 precipitates and gradually turns into the doped compound. This results in the formation of two precipitation regions: a leading white precipitate band that is followed by the purple precipitation zone. By the one-day mark, the first band near the interface is already a purple color in all the plates. In the control plates, the maximum concentration of cobalt in the first band is reached from day one and remains approximately 21% throughout the study, Figure 4.11b. A similar effect is observed in the +2 V plates, where the lower cobalt concentration of approximately 17% is achieved and maintained by the first day.

The application of -2 V for one day bears no effect on cobalt incorporation, with a cobalt concentration of 23% comparable to the 21% in the control. The cobalt concentration jumps up to 28% by day 2, then jumps again to 31% from day 3 to day 4. The trend is similar in terms of morphological enhancement.

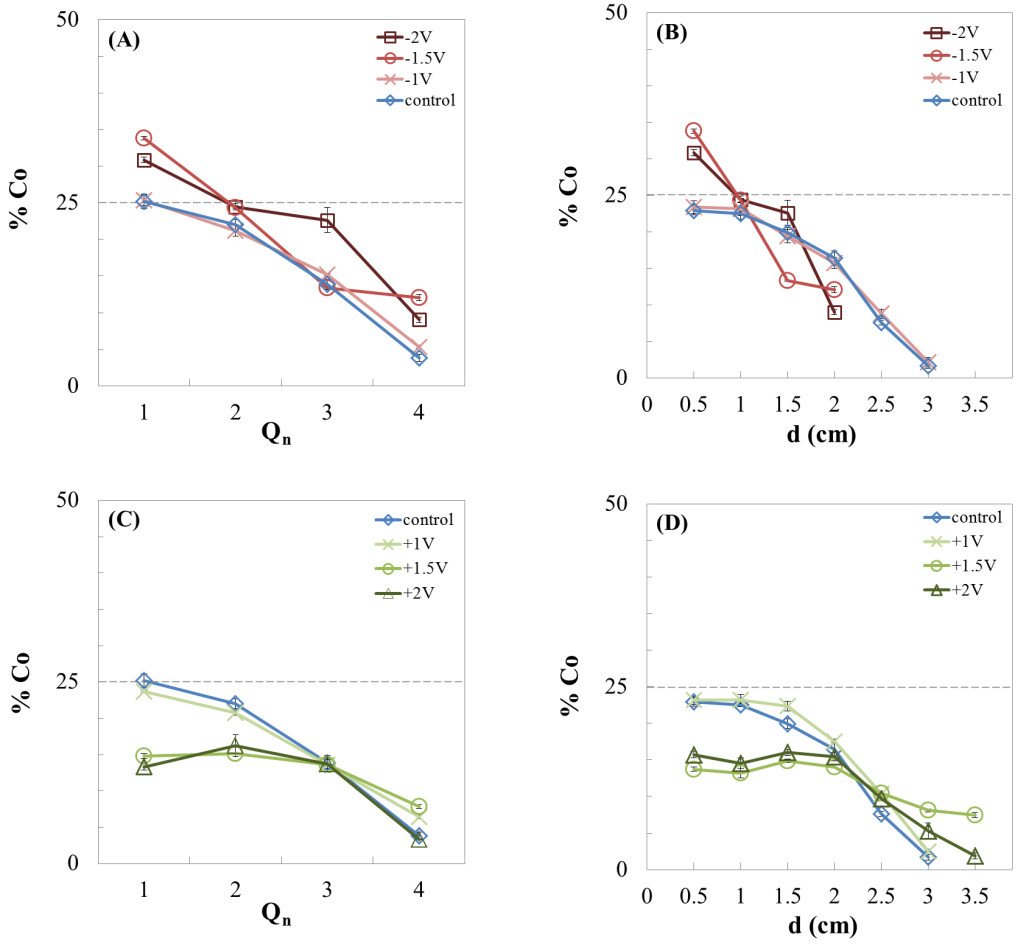

Figure 4.10: Plots displaying the influence of different potential differences on cobalt incorporation. Plots (A) and (C) show the distribution of cobalt in the negative and positive plates, using the quarter collection method, and plots (B) and (D) using the bands method.

The first band in the -2 V plate is identical to that in the control on day 1 and consists of mostly rugged polyhedra. The amount of smooth polyhedra increases with time until a sample consisting of only smooth polyhedra is obtained on day 4. In all -2 V reactors, the co-precipitate appears starting the second band, Figures A.23 through A.26.

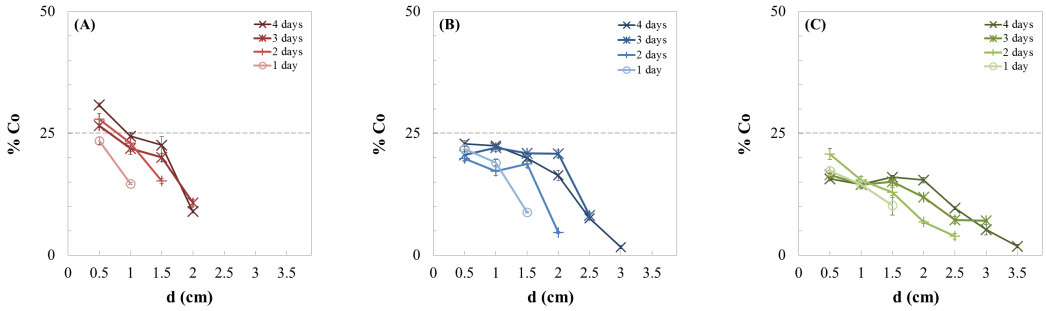

Figure 4.11: Plots displaying the incorporation of cobalt into the ZIF-8 framework in 1,2,3, and 4 days under the influence of -2 V (A), 0V (B), and +2 V (C).

4.3.6 Application of an External Electric Field to a Co-doped ZIF-8 System After Reaction-Diffusion

The kinetic study shows that under the effect of -2 V, cobalt is incorporated into the system in two waves: the first occurs by the first day of propagation and is compatible with that in the control, and the second occurs in the subsequent three days. This implies that an external electric field might affect the cobalt concentration in Co-doped ZIF-8 that had already formed. To investigate this possibility, three reactors are prepared using a 25% cobalt precursor solution and are allowed to propagate for 2 days. Afterward, one plate is subjected to -2 V, another to +2 V, and the third is kept as a control, and the plates are kept to propagate for another 4 days before the precipitate is collected using 0.5 cm bands for analysis by EDX.

The concentration of cobalt in the section that precipitated before the application of the electric field was affected by the presence of a potential difference, following the same trend observed previously. Under the influence of -2 V, the cobalt concentration increased from 23 to 34% in band 1, from 22 to 32% in band 2, and from 21 to 30% in band 3, Figure 4.12a. The effect of +2 V is less pronounced, with a slight decrease in cobalt concentration to 19, 20, and 17% in bands 1,2, and 3, respectively. This means that the enhancement in cobalt incorporation occurs after the initial precipitation stage. In the nitrate system, we expect that the effect of the negative field is analogous with that of raising the temperature of the medium. At higher temperatures more cobalt is incorporated

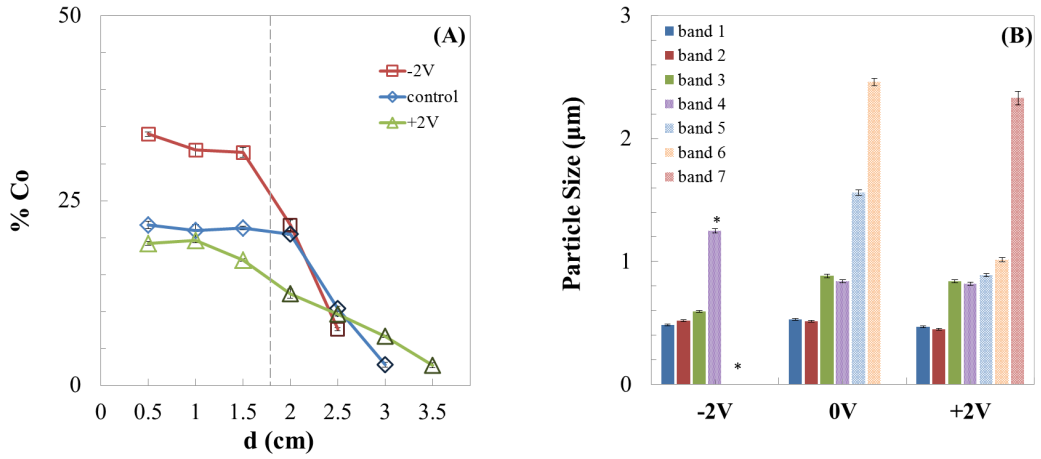

Figure 4.12: Plots representing the effect of electric field on Co-doped ZIF-8 after precipitation. Plot (A) illustrates the effect on the concentration of cobalt in the precipitate. Data points to the left of the dashed line represent samples that precipitated before the external electric field was applied, and points to the right of the line represent samples that precipitated while the system was under the influence of the electric field. Plot (B) illustrates the effect on particle size. The solid columns represent samples that precipitated before the application of the electric field and the textured ones after. Samples containing the spherical co-precipitate are marked by an asterisk (*).

into the ZIf-8 framework, since an increase in the nucleation of ZIF-8 depletes the zinc from the surroundings, leading to more cobalt consumption during the growth stage to form the mixed-metal product [114]. In the section that precipitated under the influence of the electric field, the concentration of cobalt in the -2 V reactor drops sharply and becomes equivalent to that in the control plate. The effect of +2 V becomes more pronounced in this section, with concentrations dropping from 20 to 12% in band 4.

The size of the particles is unaffected in both sections of the reactors, Figure 4.12b. As with previous results, the application of +2 V has a negligible effect on the particle morphology. The effect of -2 V on morphological enhancement is also present, with more smooth polyhedra forming in the first band of the -2 V sample than in that of the control, Figure 4.13. Moreover, the formation of the co-precipitate is inhibited in the section of the reactor that precipitated before the introduction of the electric field, Figure 4.12b.

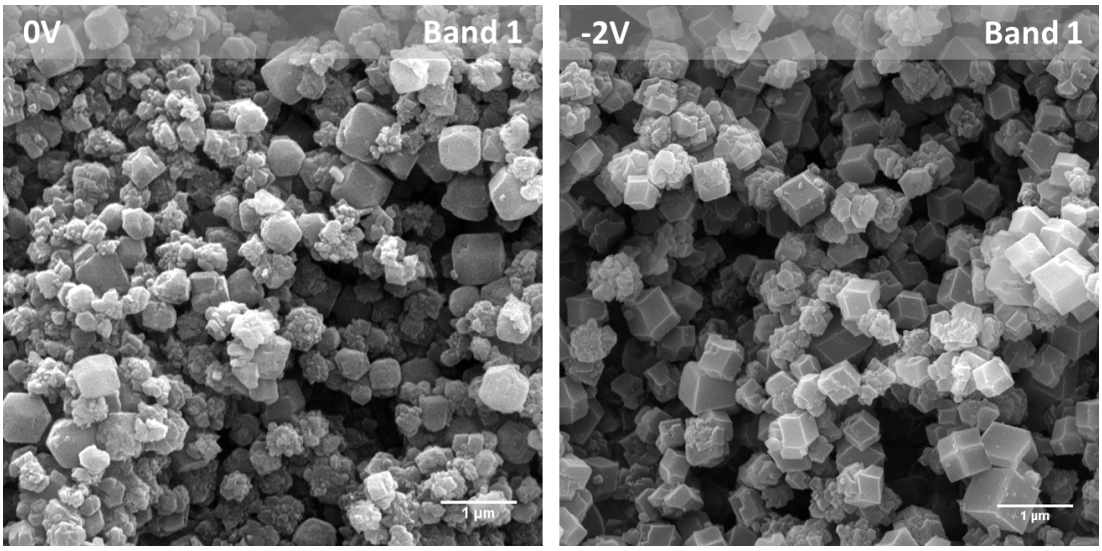

Figure 4.13: SEM micrographs comparing the morphology of the Co-doped ZIF-8 polyhedra precipitated in the first band in of the control plate (left) and the -2 V plate (right).

The electric field also affects the speed of propagation. While the precipitate in all reactors traveled 1.5 cm in the first four days, after the application of electric field the -2 V plate propagated for an additional 1 cm, the control plate an additional 1.5 cm, and the +2 V plate 2 cm.

4.3.7 Electric Field-Induced Doping of ZIF-8

Since there is an apparent effect of an external electric field on the cobalt incorporation in doped ZIF-8 that had already precipitated in the reaction-diffusion system, a preliminary study is done to test the possibility of doping ZIF-8 by postsynthetic exchange (PSE) using an external electric field, which is usually assisted by high temperatures [206, 207].

First, ZIF-8 is synthesized via 1-dimensional reaction-diffusion, using the method reported by Saliba et. al [114]. The precipitate is collected, cleaned, and allowed to dry into a powder. Second, a solution containing 20 mM of cobalt nitrate salt, 1% v/w agar powder, and 25% DMF is prepared. When the gel dissolves, the solution is left to cool to mix in the prepared ZIF-8 powder before being poured into three small reactors. After 30 minutes of gelation at 23 °C, one reactor is subjected to -2 V, the other to +2 V, and the third is kept as a control. The reactors are then left to sit for 7 days at room temperature before the inner 0.5 cm of each is collected for cleaning and analysis by EDX.

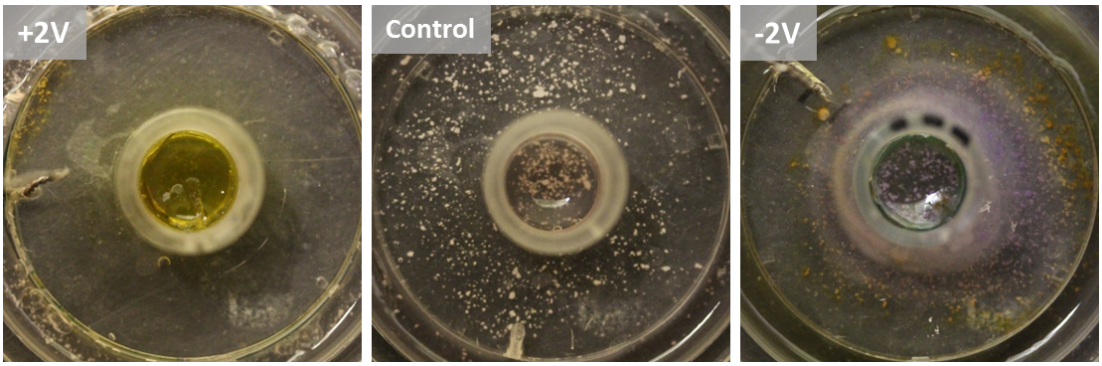

Figure 4.14: The three reactors after 7 days. The ZIF-8 powder is still visible in the control plate (middle), while it is clear that there is no more powder in the +2 V reactor (left). The change in color from white to deep purple is visible near the inner electrode of the -2 V reactor (right).

The precipitate in the control plate remains as it was, unaffected by soaking in 20mM cobalt gel for 7 days, and very low concentrations of 2-3% cobalt are found in the powder. Under the influence of +2 V, The ZIF-8 is dissociated and the gel deformed. However, under the influence of -2 V, the precipitate in the inner half of the reactor changes color from white to purple, the characteristic color of ZIF-67, with cobalt concentration rising to 47%. This is also apparent by simple observation, as the powder remains white in the control dish, disappears completely from the +2 V dish, and turns purple near the inner electrode of the -2 V dish, Figure 4.14.

Chapter 5

Conclusion

In this work, we study the effect of weak external direct-current electric fields (EF) on the precipitation of ZIF-8, ZIF-67, and Zn-Co mixed-metal ZIF-8 in a reaction-diffusion framework (RDF). The effect on the precipitation patterns, size, and morphology of the precipitate, and cobalt concentration in the doped framework is examined for two RD systems for each type of ZIF: one using sulfate metal salt precursors, and the other using nitrate salt precursors.

The effect on the precipitation pattern is similar in all systems, with the positive field accelerating the propagation, and negative field decelerating it, which was expected since the active species are positively charged. The ZIF-8 system using sulfate salts exhibits Liesegang banding, which is also affected by the EF. The positive potential difference results in bands spaced further apart, while the negative difference brings the bands closer together.

The effect of EF on the size and morphology of the precipitated particles depends on the system used but is most prominent in the first quarter of the precipitation zone for all systems. In the sulfate systems, the positive potential difference reduces the particle size by approximately 40 % and leads to the precipitation of polyhedra with rougher surfaces than in the control, while the negative field has no effect. However, in the nitrate systems, the positive field has no effect while the negative potential difference leads particles that are approximately twice the size of those in the control, and results in smoother and more uniform polyhedra. While the observed effects could be explained separately, the reason behind the lack of effect of a negative field on the sulfate system and a positive field on the nitrate system is still unclear. Further investigations on the pH changes during the reaction under the different conditions could help us gain insight, since the electric field could have an effect on acid-base reactions that play a role in ZIF formation [208, 209]. All systems show narrow particle size distributions, except for the ZIF-67 precipitated using nitrate salts. The con-

trol samples all consist of smooth polyhedra but have a wide size distribution; the application of a negative EF results in more monodisperse particles while maintaining the smooth surface of the polyhedra.

The electric field also affects the formation of co-precipitates and the precipitation of different phases. In ZIF-8 and mixed-metal ZIF-8, the application of a negative electric field results in the production of a spherical co-precipitate starting with the second quarter of the precipitation zone and eventually becomes the only precipitate at the diffusion front. PXRD analyses show that this co-precipitate is common at low linker to metal ion ratios [202, 203], which could be a result of ion migration towards the inner electrode under the influence of the negative field. In ZIF-67 systems, an amorphous second phase usually forms at the precipitation front [204]. A negative potential difference brings the early onset of the second phase, while positive EF completely suppresses the formation of the precipitate.

The effect of the electric field on the cobalt concentration in mixed-metal ZIFs is similar in both metal salt precursor systems. The application of a negative potential difference encourages the doping, increasing the concentration of cobalt in the mixed-metal framework, while the positive EF reduces the extent of doping. The trend is clearer in the nitrate salt systems than in the sulfate salt ones, as the nitrate systems already witness a cobalt concentration gradient along the reactor [114], while the extent of cobalt incorporation is more random in the sulfate salt system.

Further study on the effect on mixed-metal ZIF-8 using nitrate salts shows that the change in cobalt incorporation occurs around one day after the precipitation begins. The electric field also affects systems that are allowed to precipitate for two days in the absence of EF first. The same trend as with the systems that precipitate in the presence of electric field persists, with the negative potential difference increasing the amount of cobalt in the mixed-metal framework, and the positive potential reducing it, even in the precipitate near the electrode, which precipitated before an electric field is applied, which shows that the enhancement in cobalt incorporation occurs after the initial precipitation stage. Furthermore, the formation of spheres in that area is avoided, and they only appear in the zone that precipitates after the application of EF.

Finally, we find that applying a negative external electric field to pre-synthesized ZIF-8 powder that is suspended in 20 mM cobalt gel induces cobalt doping by postsynthetic exchange, resulting in a mixed-metal ZIF in the area near the inner electrode, while the positive field leads to the complete dissolution of the framework. However, this result is preliminary and further investigation is needed to be able to understand the factors that affect the electric field-induced doping and build a skeleton that would allow us to use an external electric field as a parameter to control doping in ZIFs.

Appendix A

Digital Camera and SEM Images

The images of all the systems are labeled using the same legend:

- Images in the first (horizontal) row are labeled "A" and belong to samples in the +2V reactor.
- Images in the second row are labeled "C" and belong to samples in the control reactor.
- Images in the third row are labeled "B" and belong to the samples in the -2V reactor.
- The scale bar in all SEM images represents 2 μm.

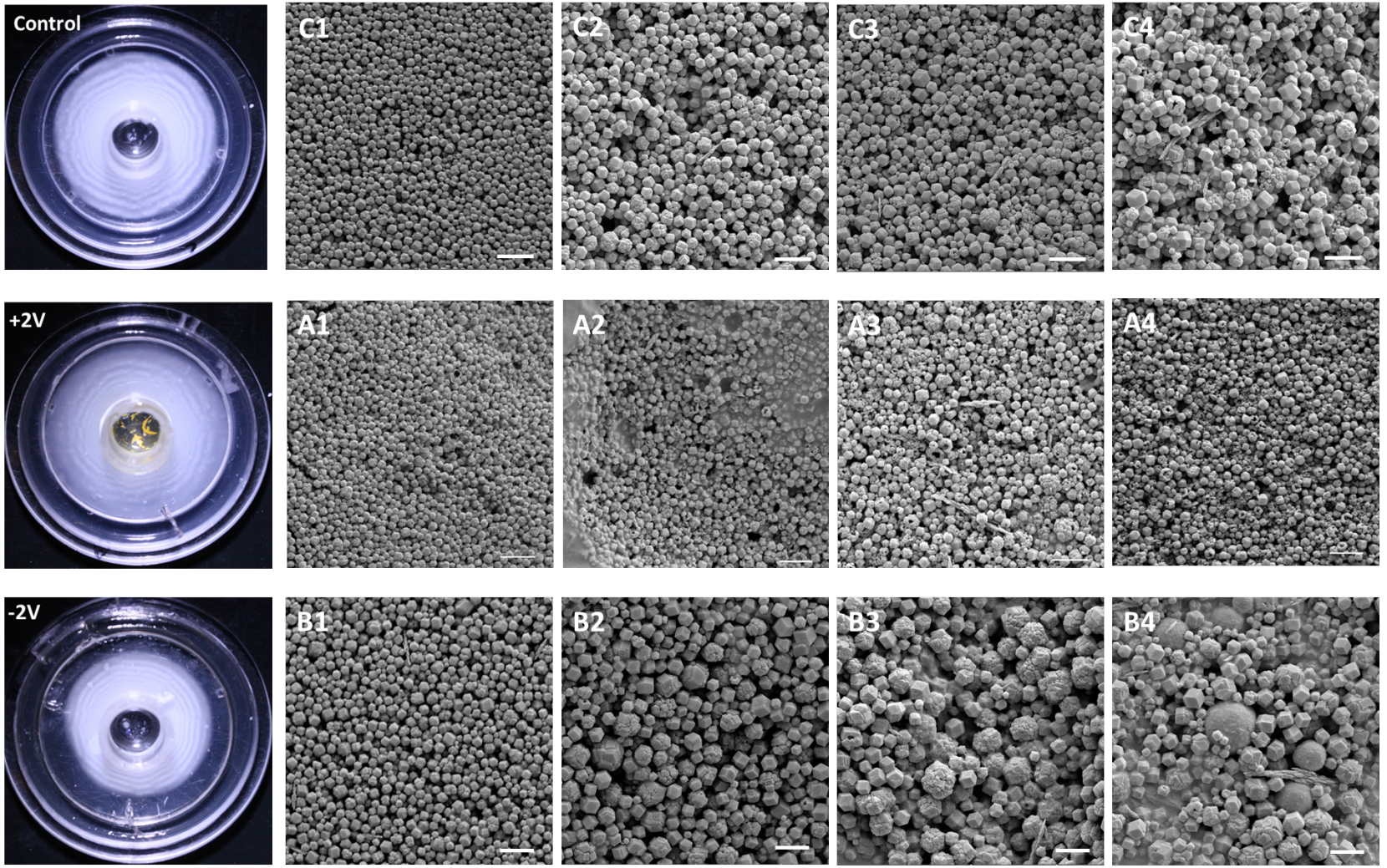

Figure A.1: Images of the ZIF-8 system using sulfate salts in small reactor plates. The samples are collected as separate Liesegang bands.

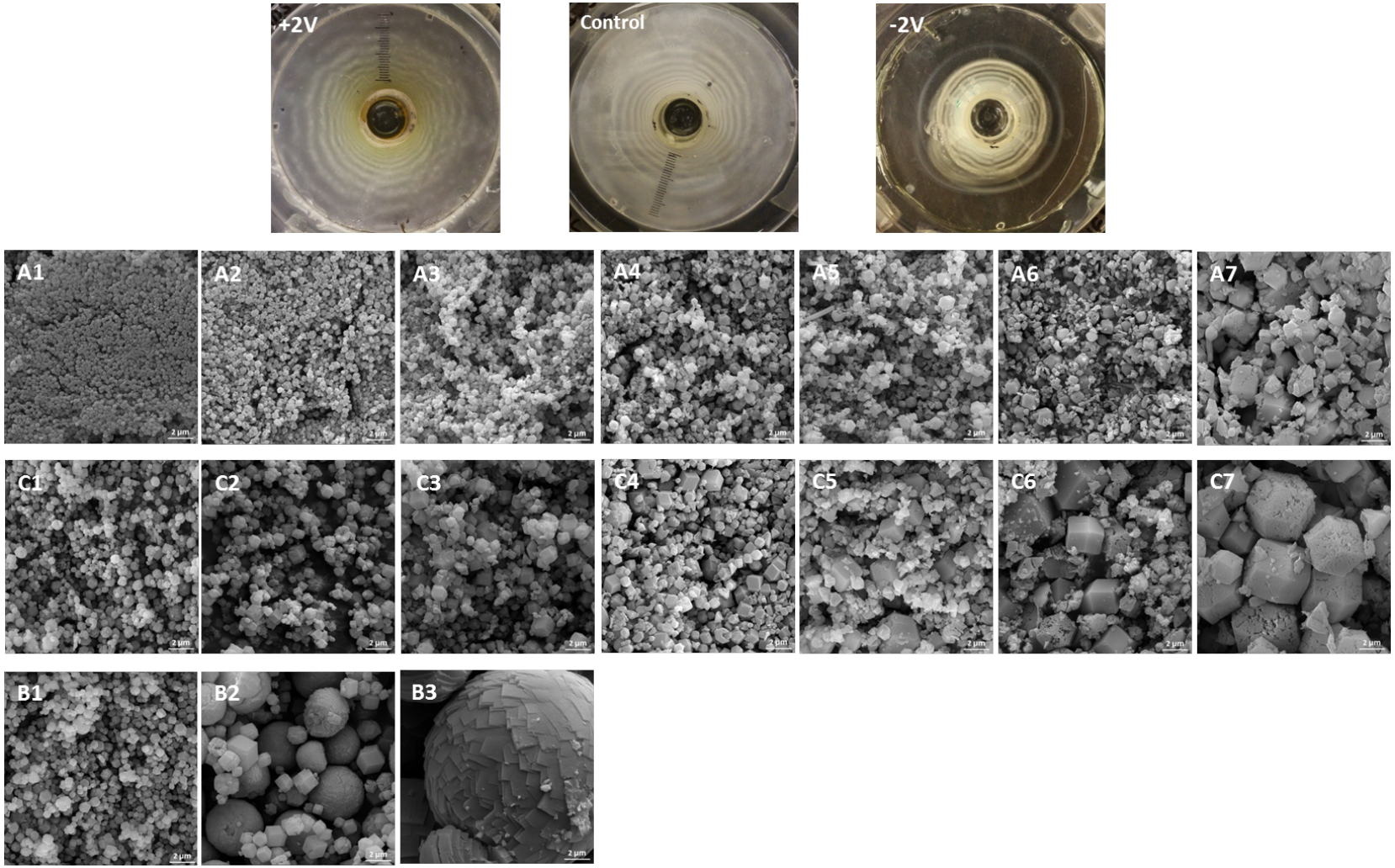

Figure A.2: Images of the ZIF-8 system using sulfate salts in big reactor plates. The samples are collected as 0.5 cm "bands".

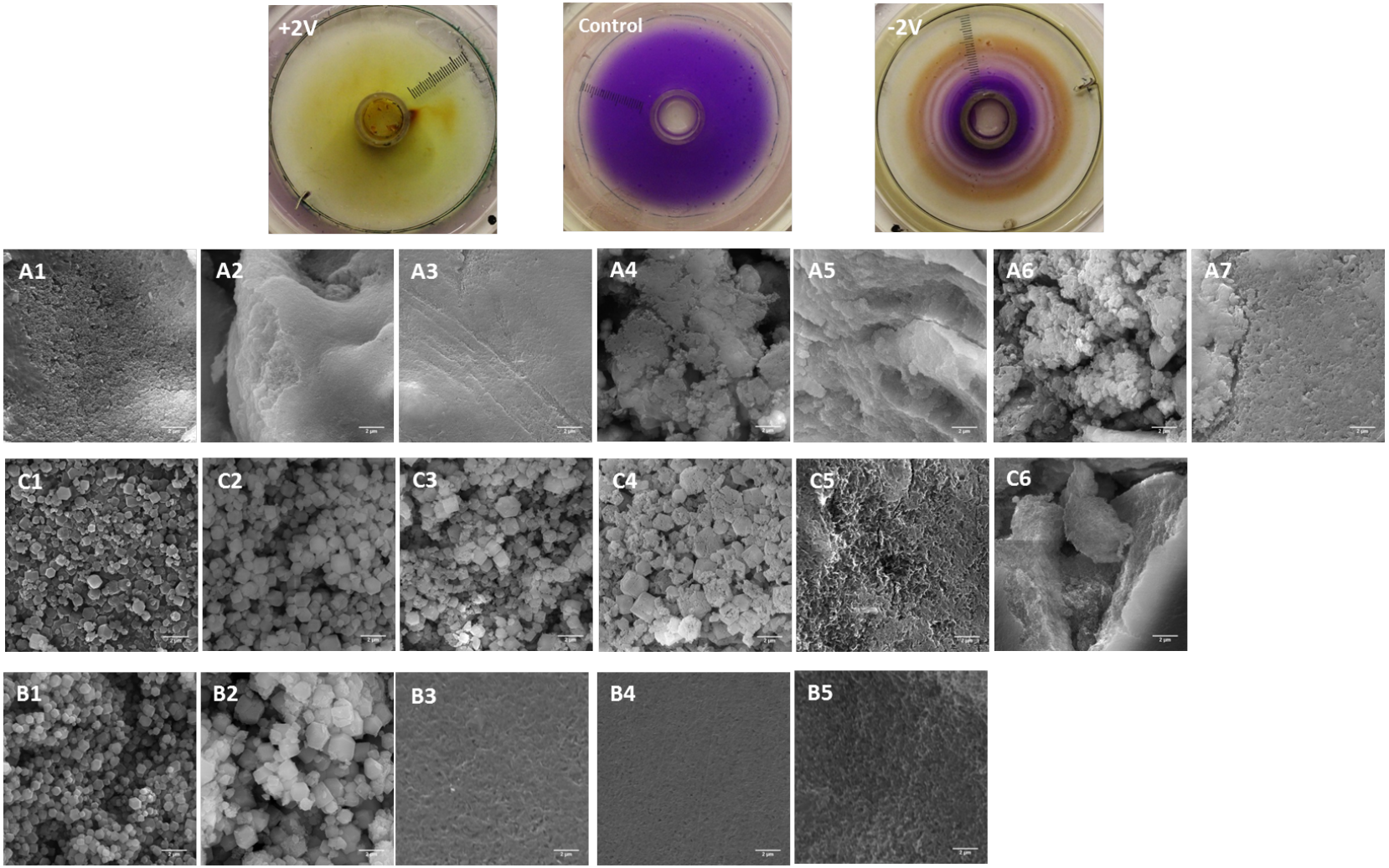

Figure A.3: Images of the ZIF-67 system using sulfate salts in big reactor plates. The samples are collected as 0.5 cm "bands".

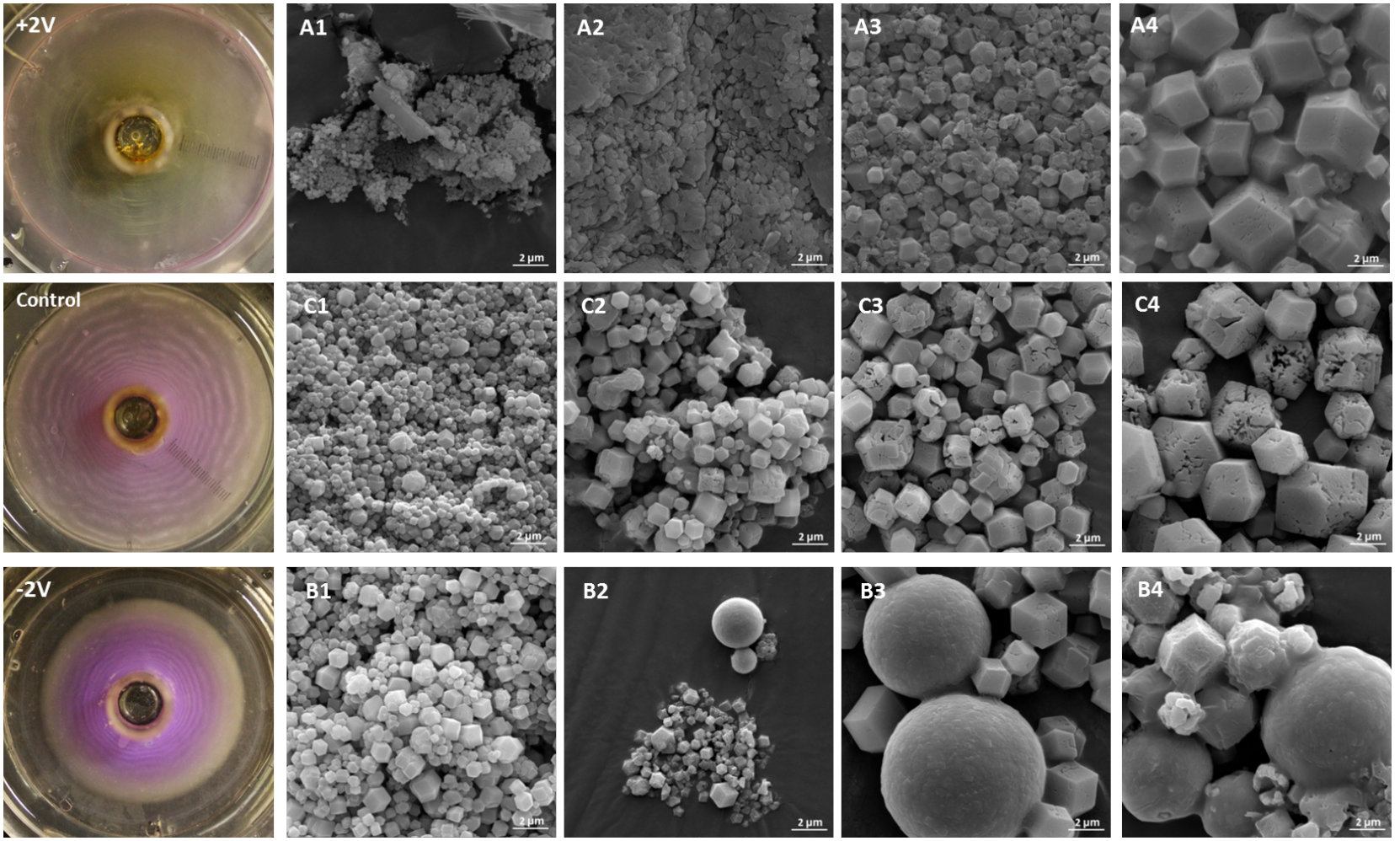

Figure A.4: Images of the Zn-Co mixed-metal ZIF-8 system using 10% Co precursor solutions and sulfate salts. The samples are collected as quarters.

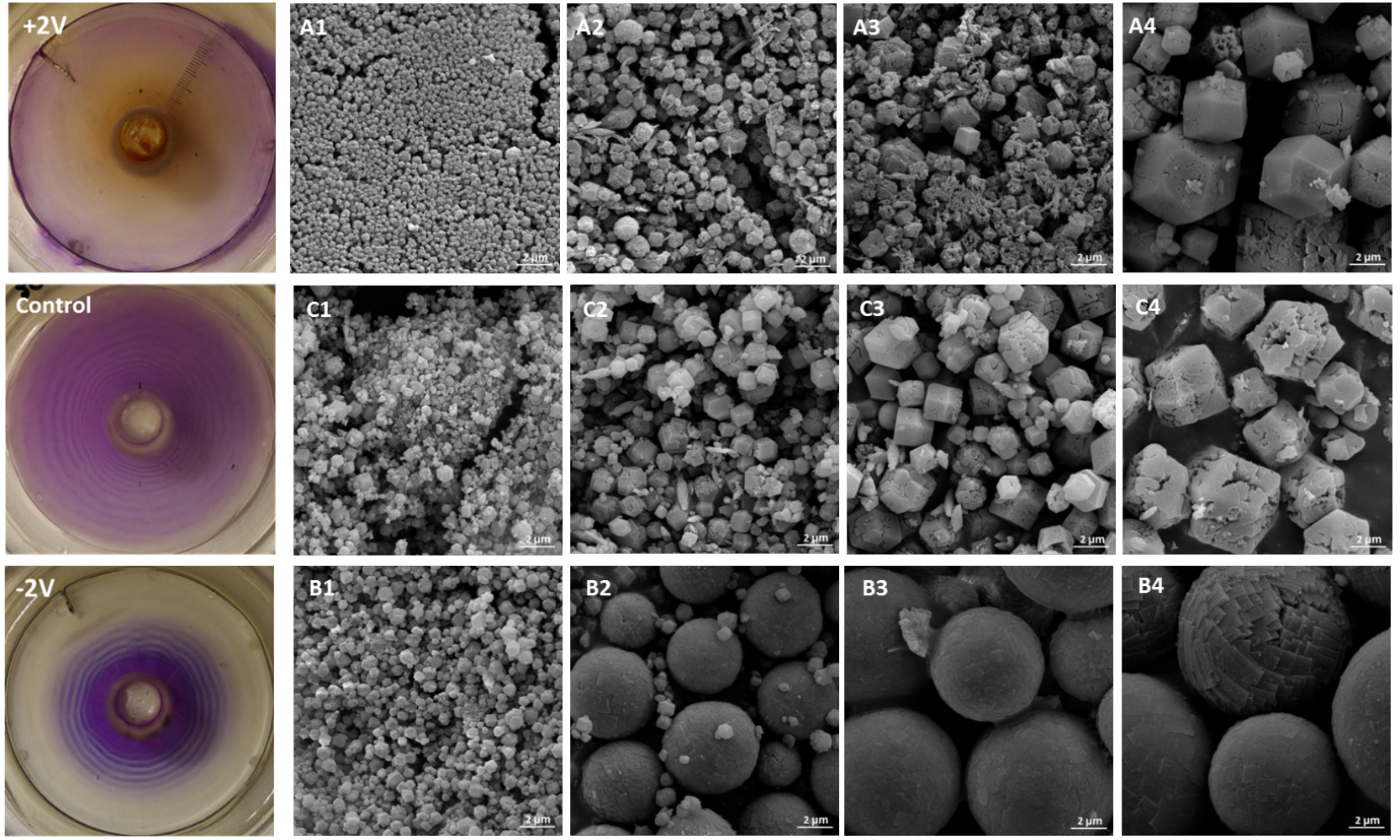

Figure A.5: Images of the Zn-Co mixed-metal ZIF-8 system using 20% Co precursor solutions and sulfate salts. The samples are collected as quarters.

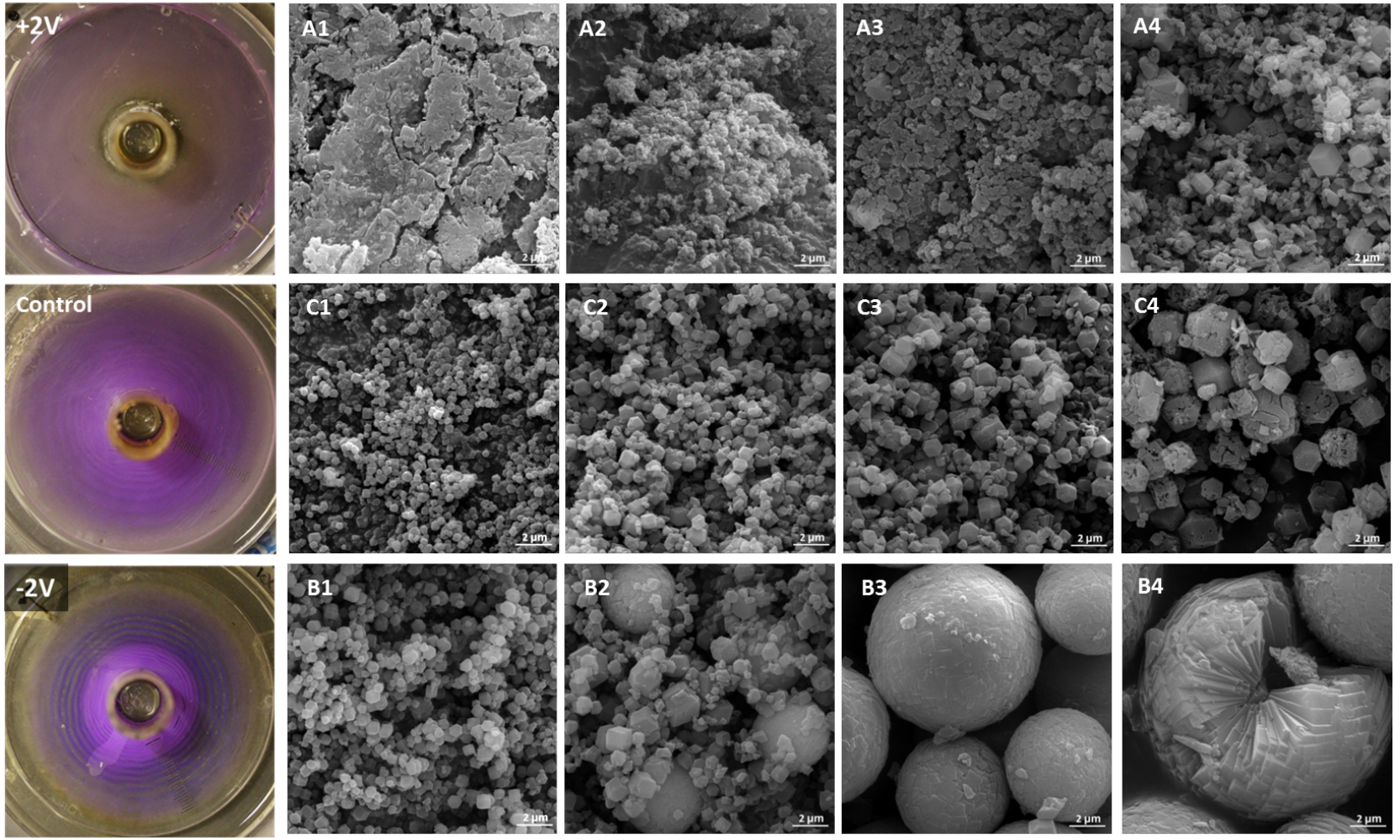

Figure A.6: Images of the Zn-Co mixed-metal ZIF-8 system using 30% Co precursor solutions and sulfate salts. The samples are collected as quarters.

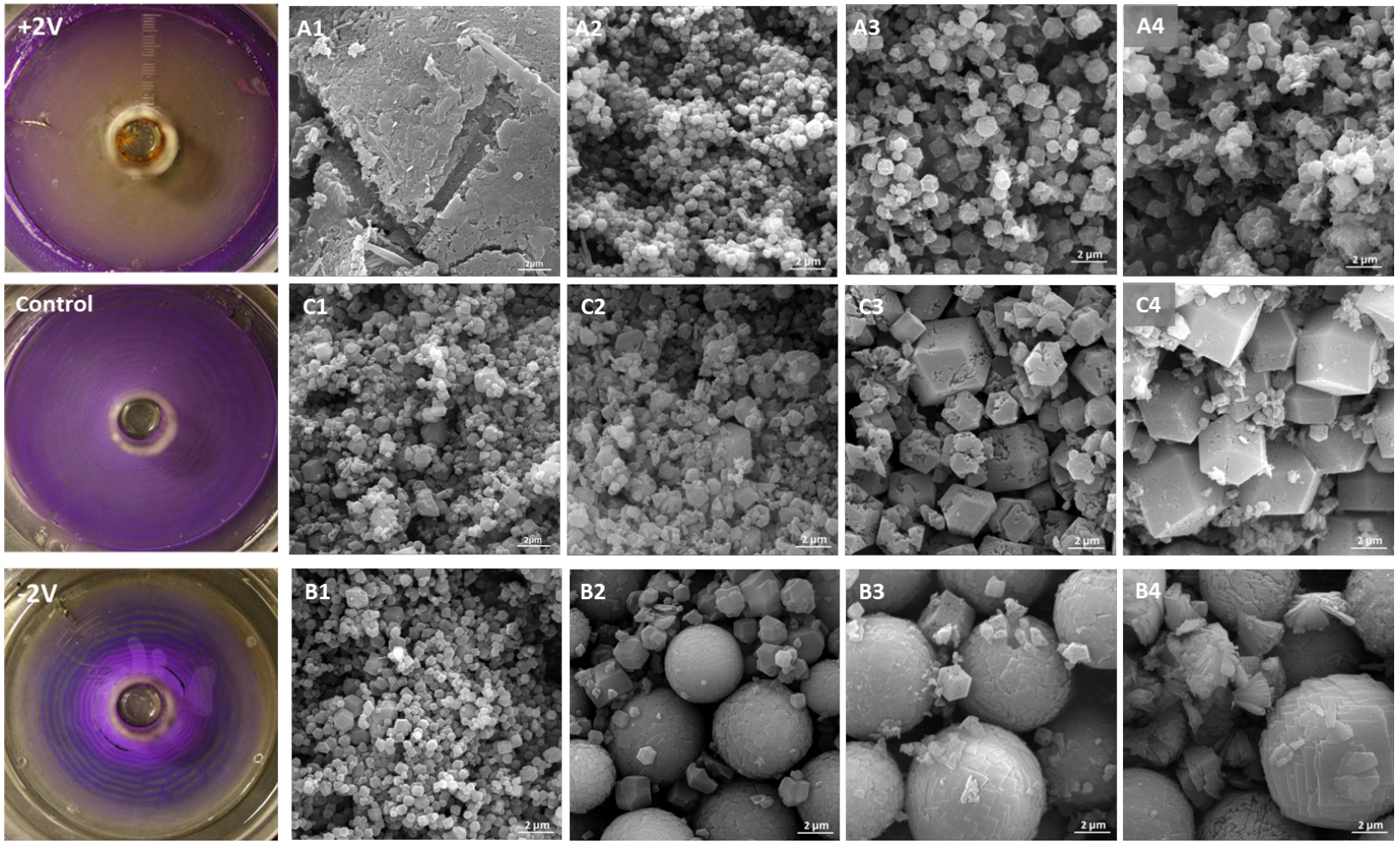

Figure A.7: Images of the Zn-Co mixed-metal ZIF-8 system using 40% Co precursor solutions and sulfate salts. The samples are collected as quarters.

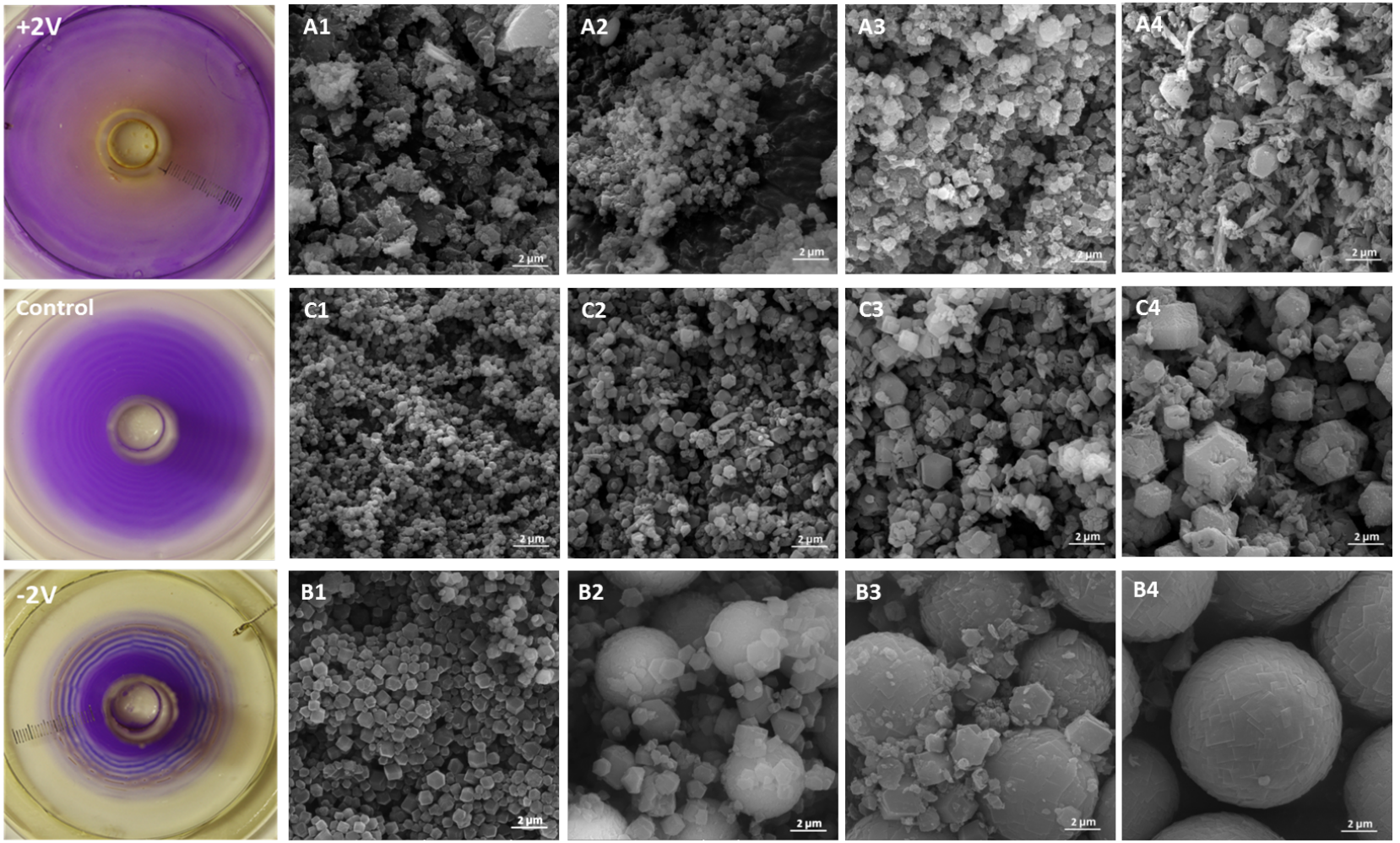

Figure A.8: Images of the Zn-Co mixed-metal ZIF-8 system using 50% Co precursor solutions and sulfate salts. The samples are collected as quarters.

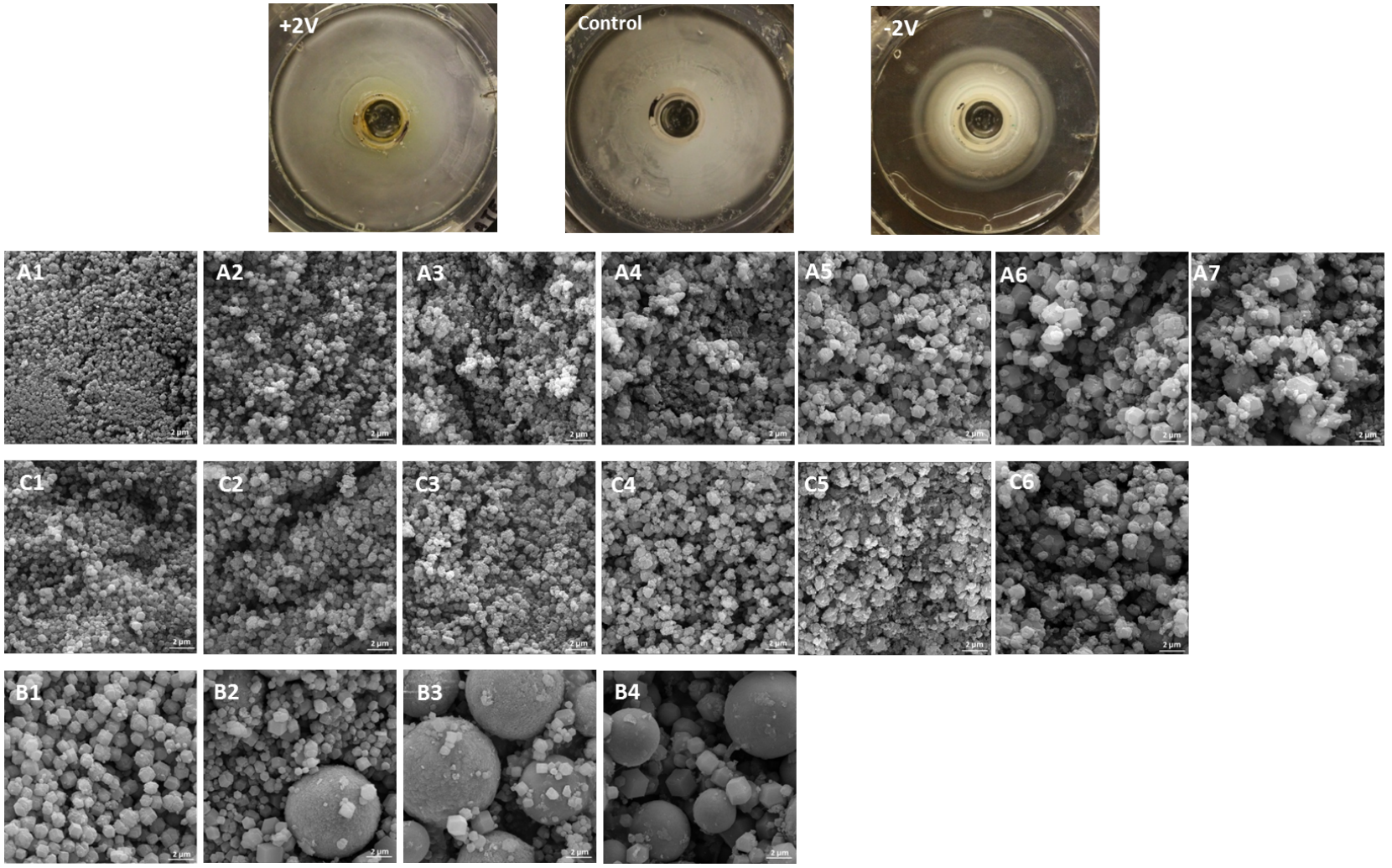

Figure A.9: Images of the ZIF-8 system using nitrate salts. The samples are collected as 0.5 cm "bands".

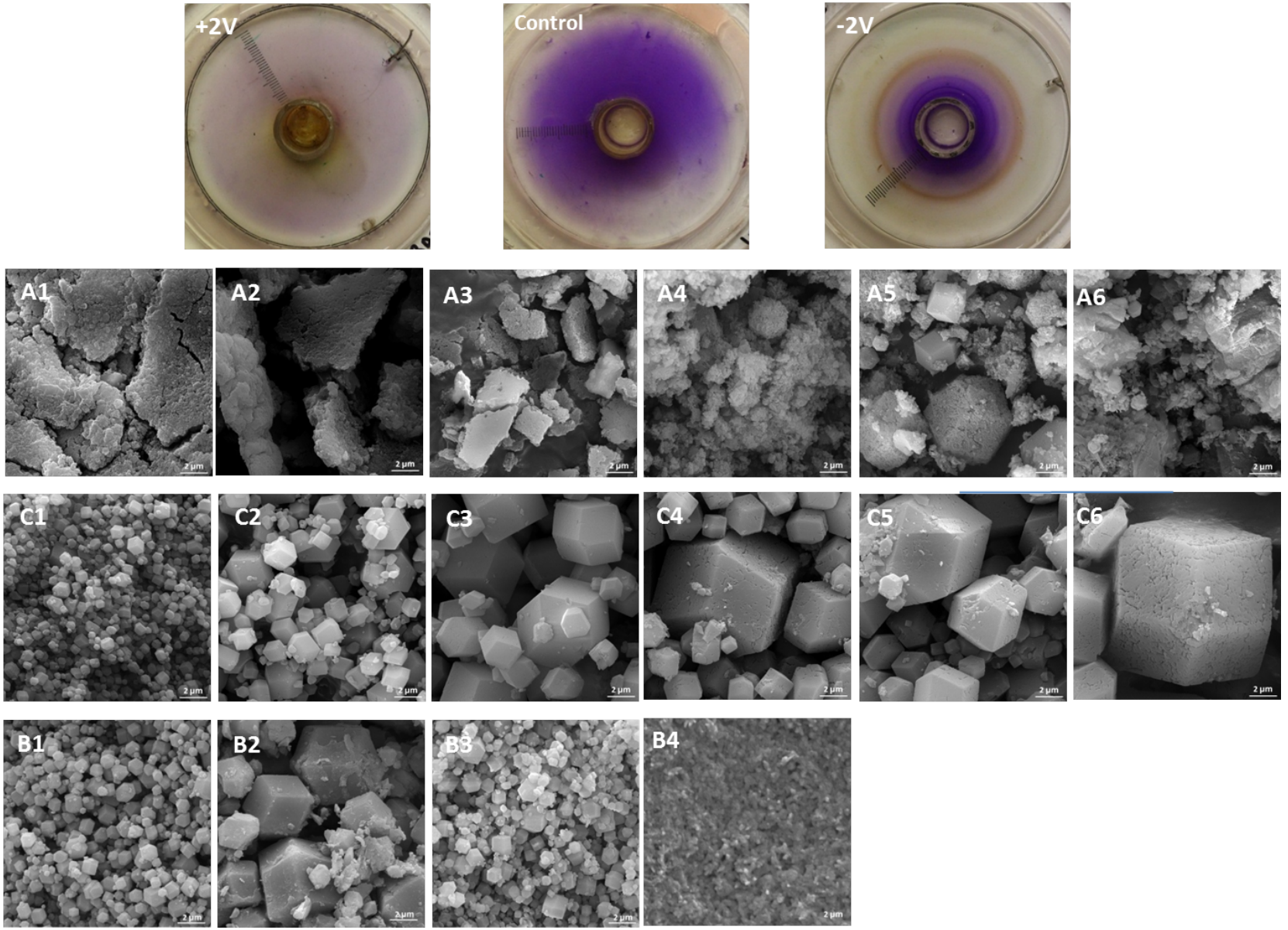

Figure A.10: Images of the ZIF-67 system using nitrate salts. The samples are collected as 0.5 cm "bands".

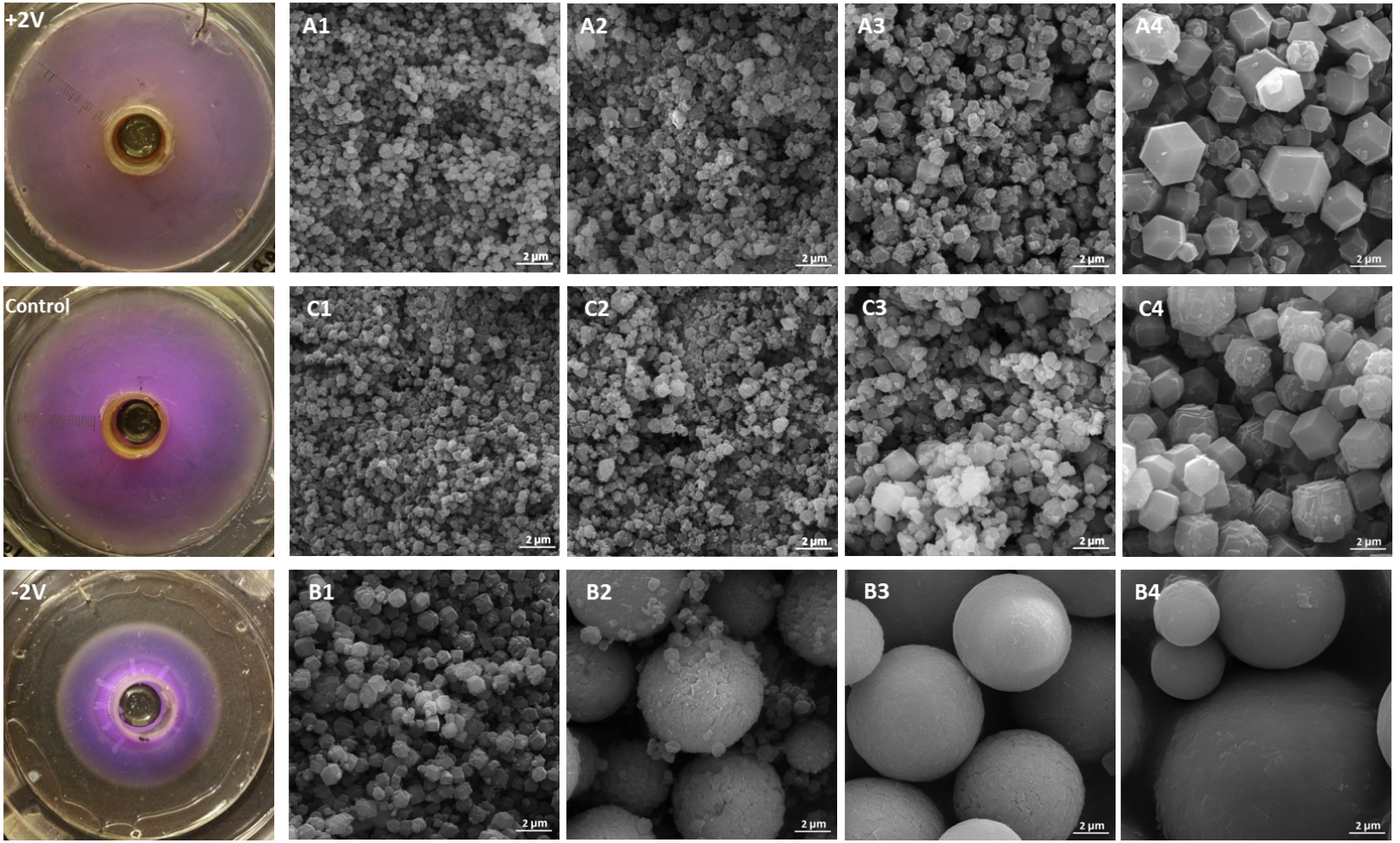

Figure A.11: Images of the Zn-Co mixed-metal ZIF-8 system using 25% Co precursor solutions and nitrate salts. The samples are collected as quarters.

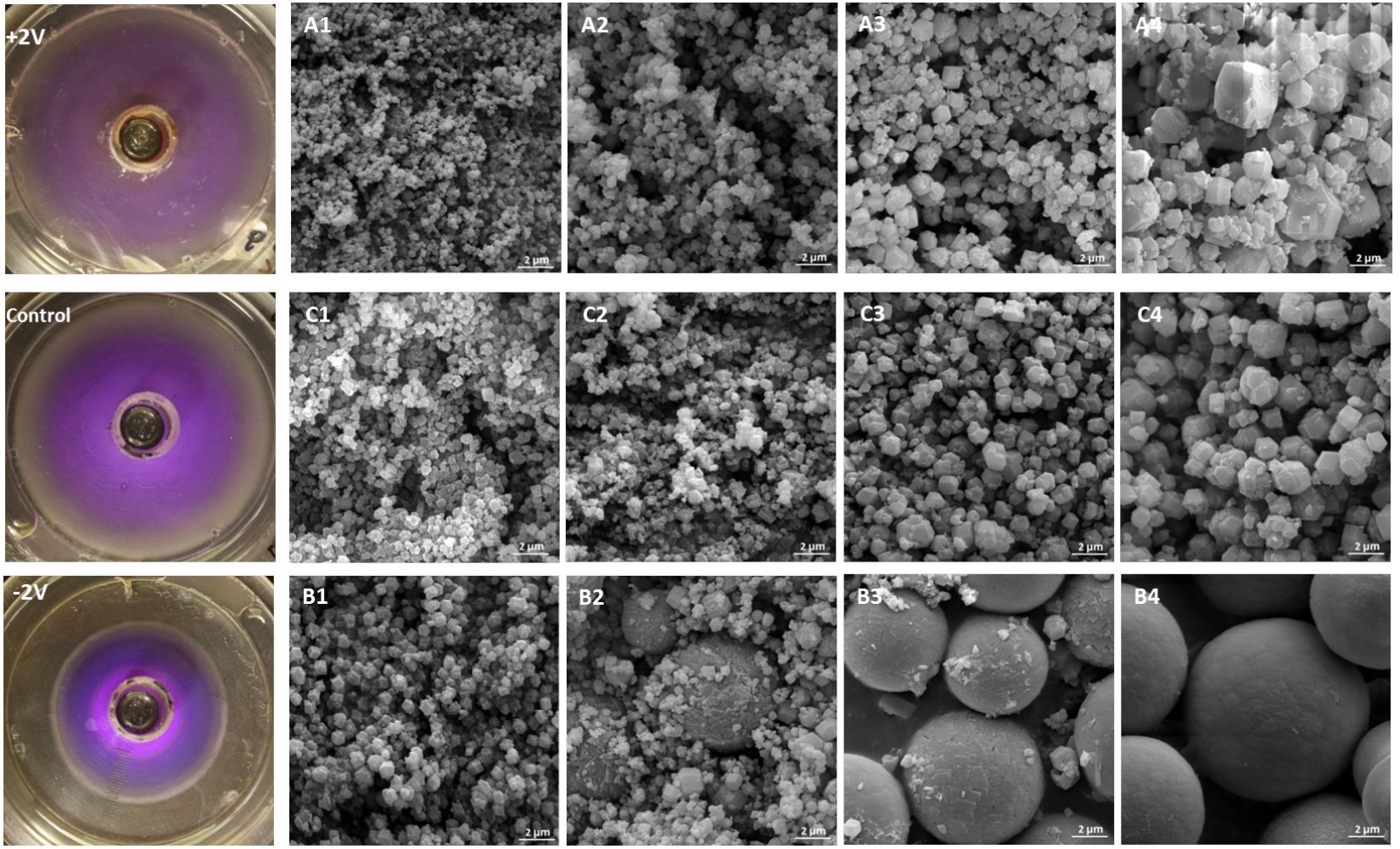

Figure A.12: Images of the Zn-Co mixed-metal ZIF-8 system using 50% Co precursor solutions and nitrate salts. The samples are collected as quarters.

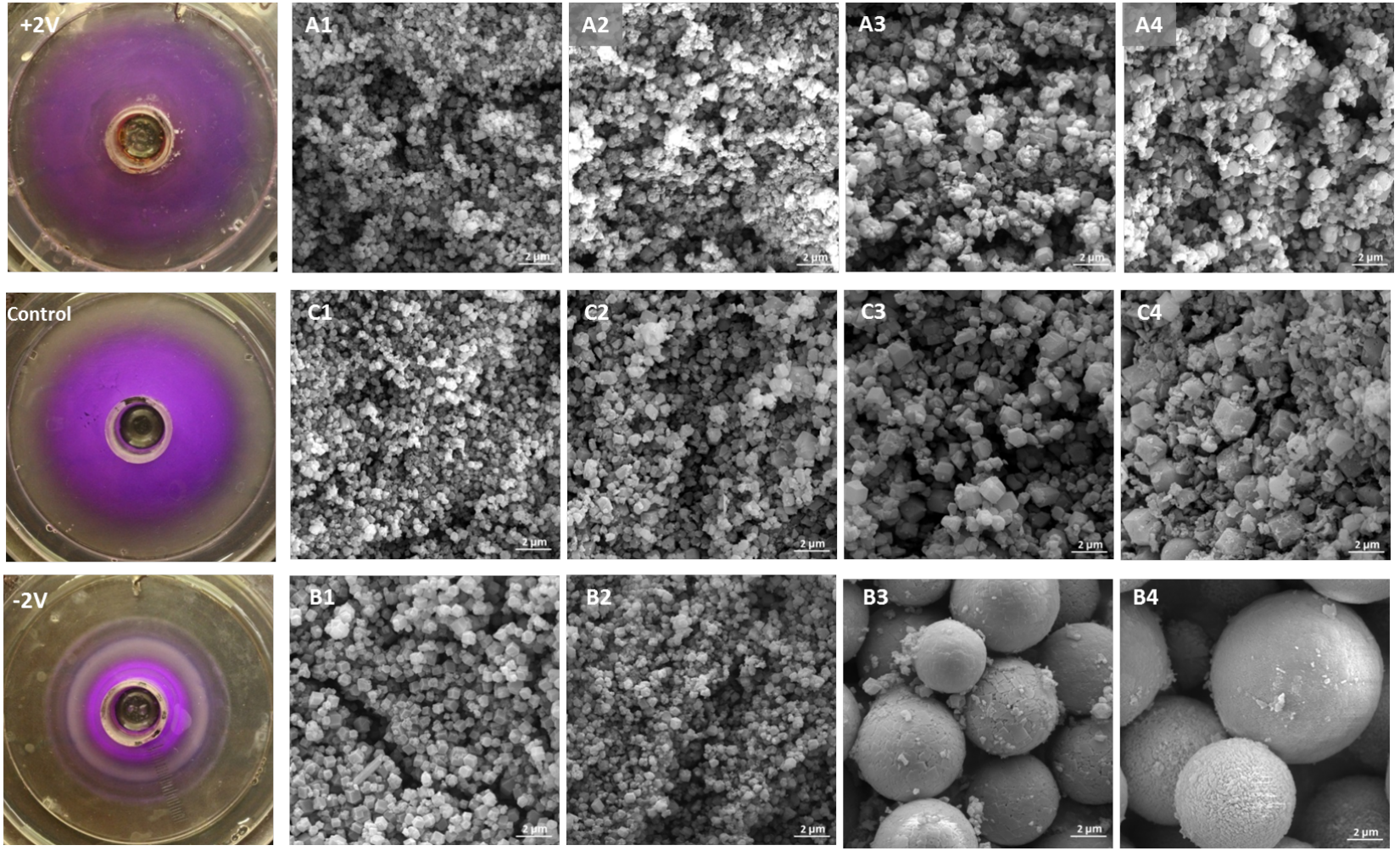

Figure A.13: Images of the Zn-Co mixed-metal ZIF-8 system using 75% Co precursor solutions and nitrate salts. The samples are collected as quarters.

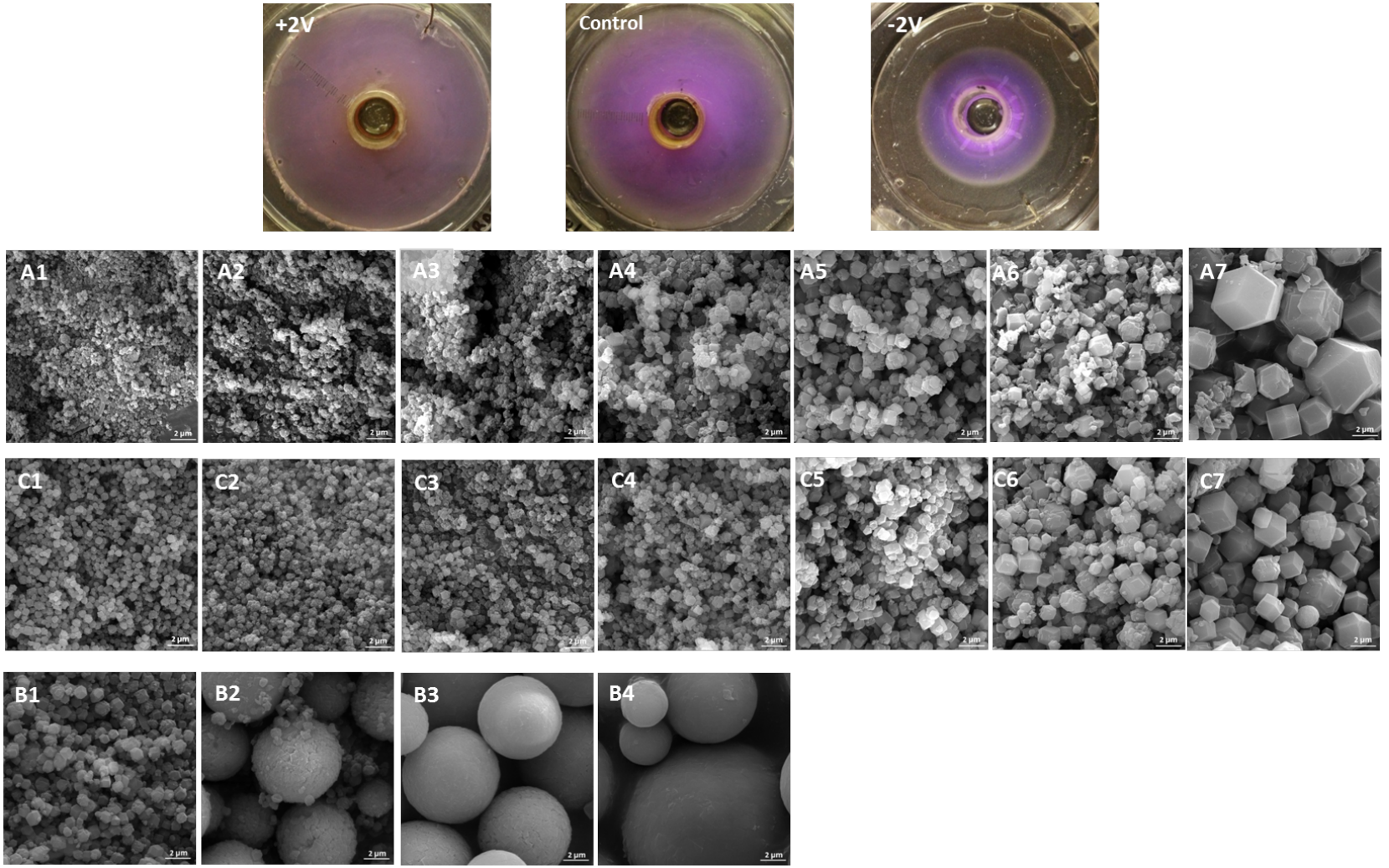

Figure A.14: Images of the Zn-Co mixed-metal ZIF-8 system using 25% Co precursor solutions and nitrate salts. The samples are collected as 0.5 cm "bands".

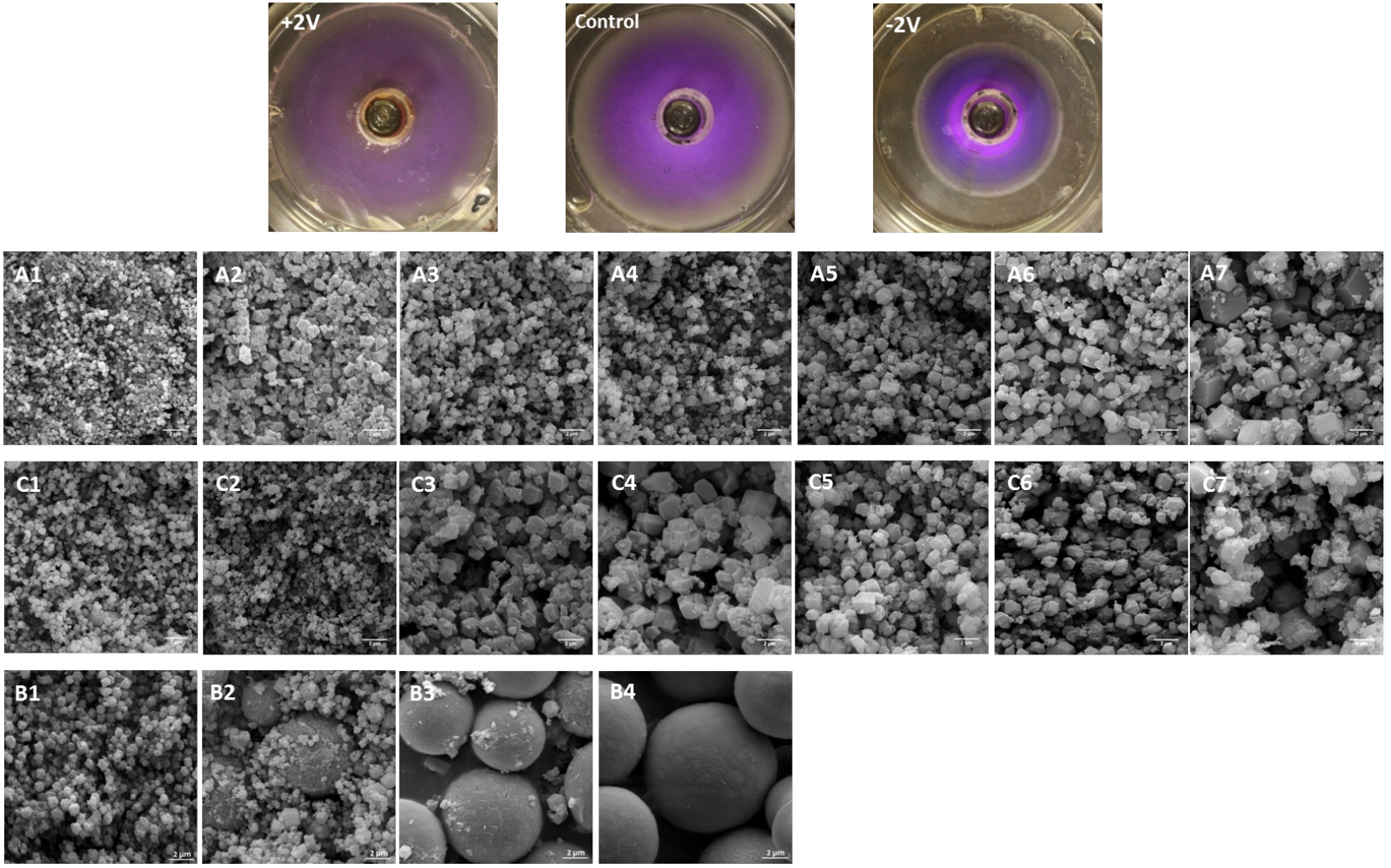

Figure A.15: Images of the Zn-Co mixed-metal ZIF-8 system using 50% Co precursor solutions and nitrate salts. The samples are collected as 0.5 cm "bands".

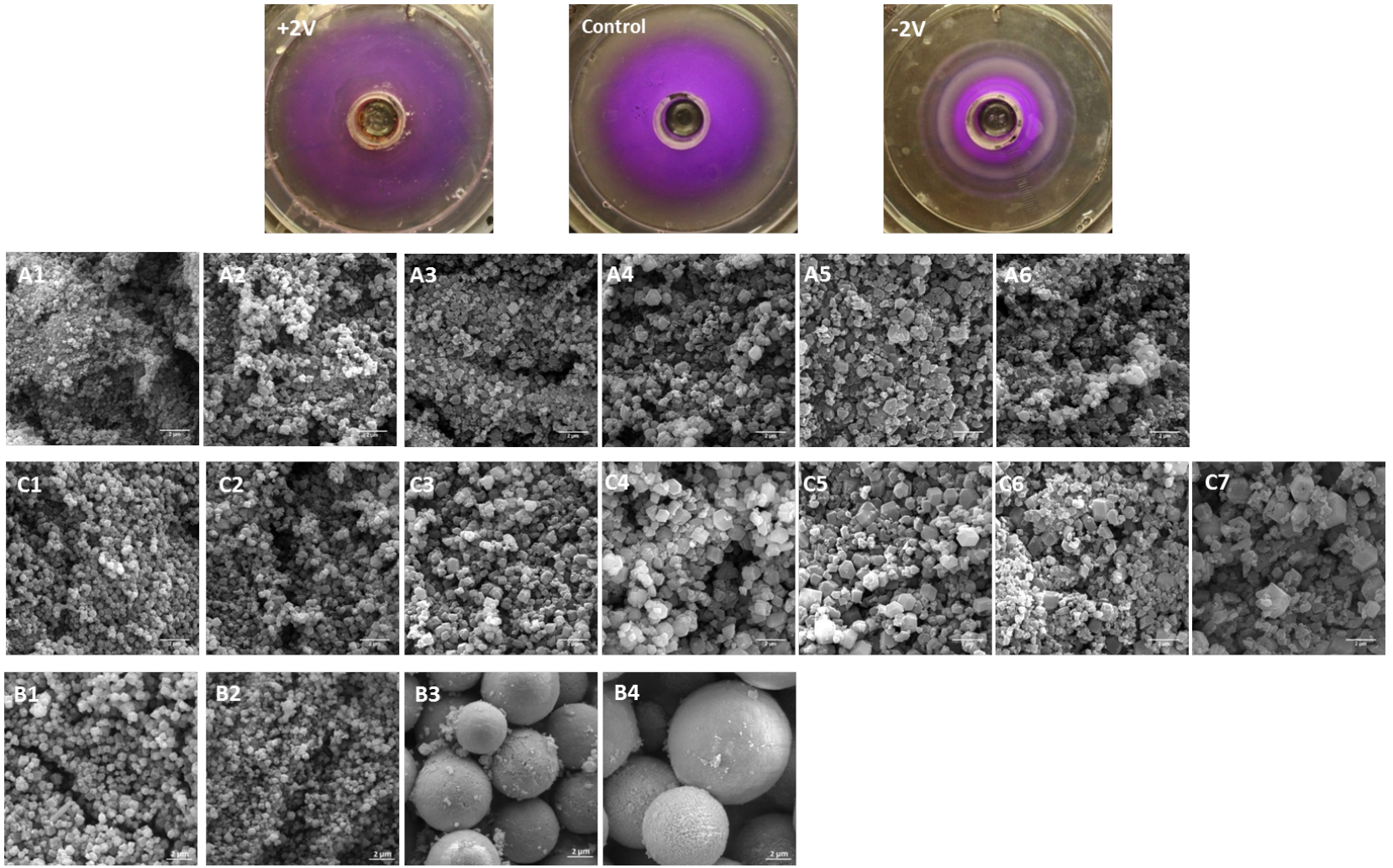

Figure A.16: Images of the Zn-Co mixed-metal ZIF-8 system using 75% Co precursor solutions and nitrate salts. The samples are collected as 0.5 cm "bands".

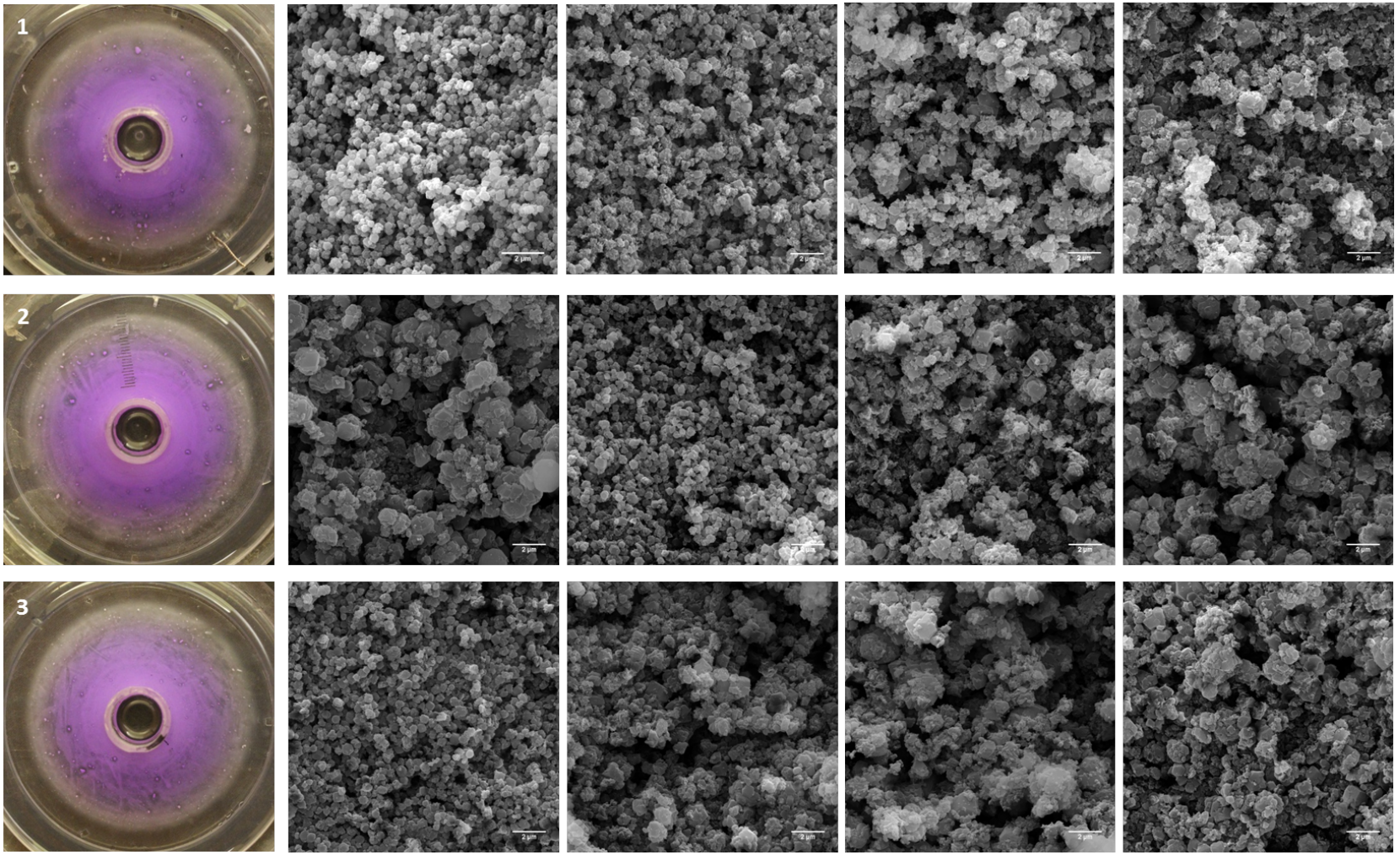

Figure A.17: Images of the three control plates in the same-batch reproducibility study. The system is Zn-Co mixed-metal ZIF-8 using 25% Co precursor solutions and nitrate salts. The samples are collected as 0.5 cm "bands".

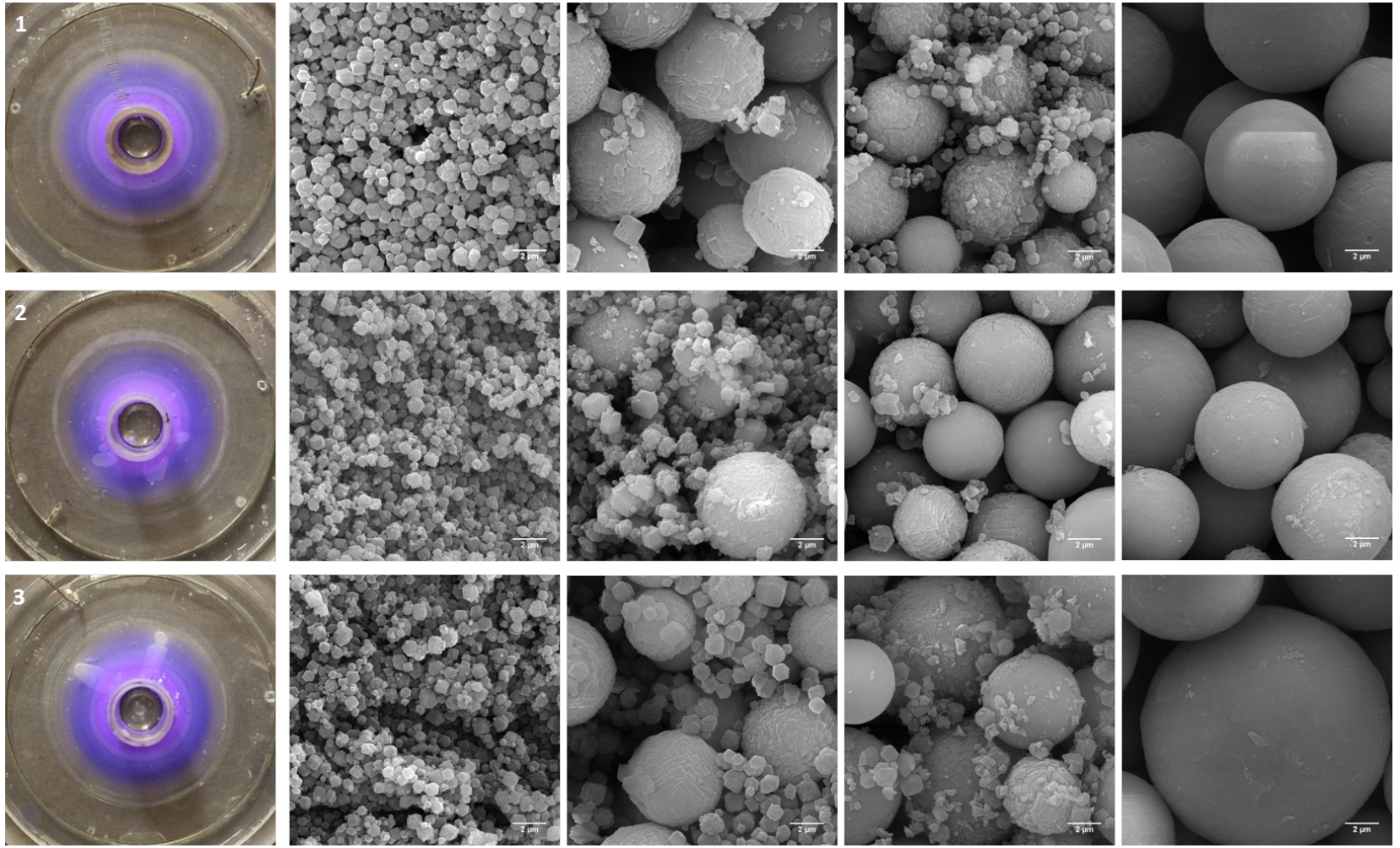

Figure A.18: Images of the three -2V plates in the same-batch reproducibility study. The system is Zn-Co mixed-metal ZIF-8 using 25% Co precursor solutions and nitrate salts. The samples are collected as 0.5 cm "bands".

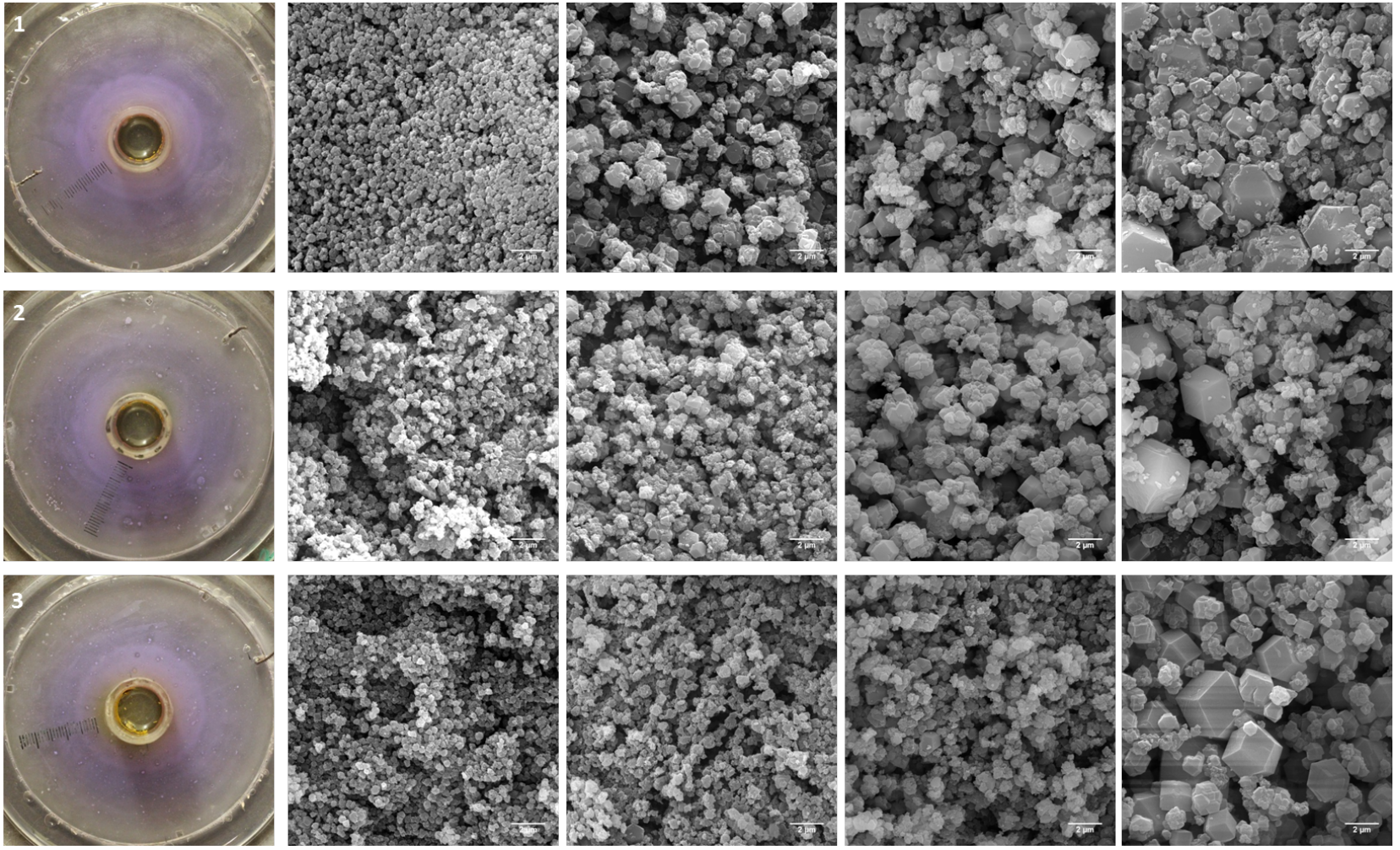

Figure A.19: Images of the three +2V plates in the same-batch reproducibility study. The system is Zn-Co mixed-metal ZIF-8 using 25% Co precursor solutions and nitrate salts. The samples are collected as 0.5 cm "bands".

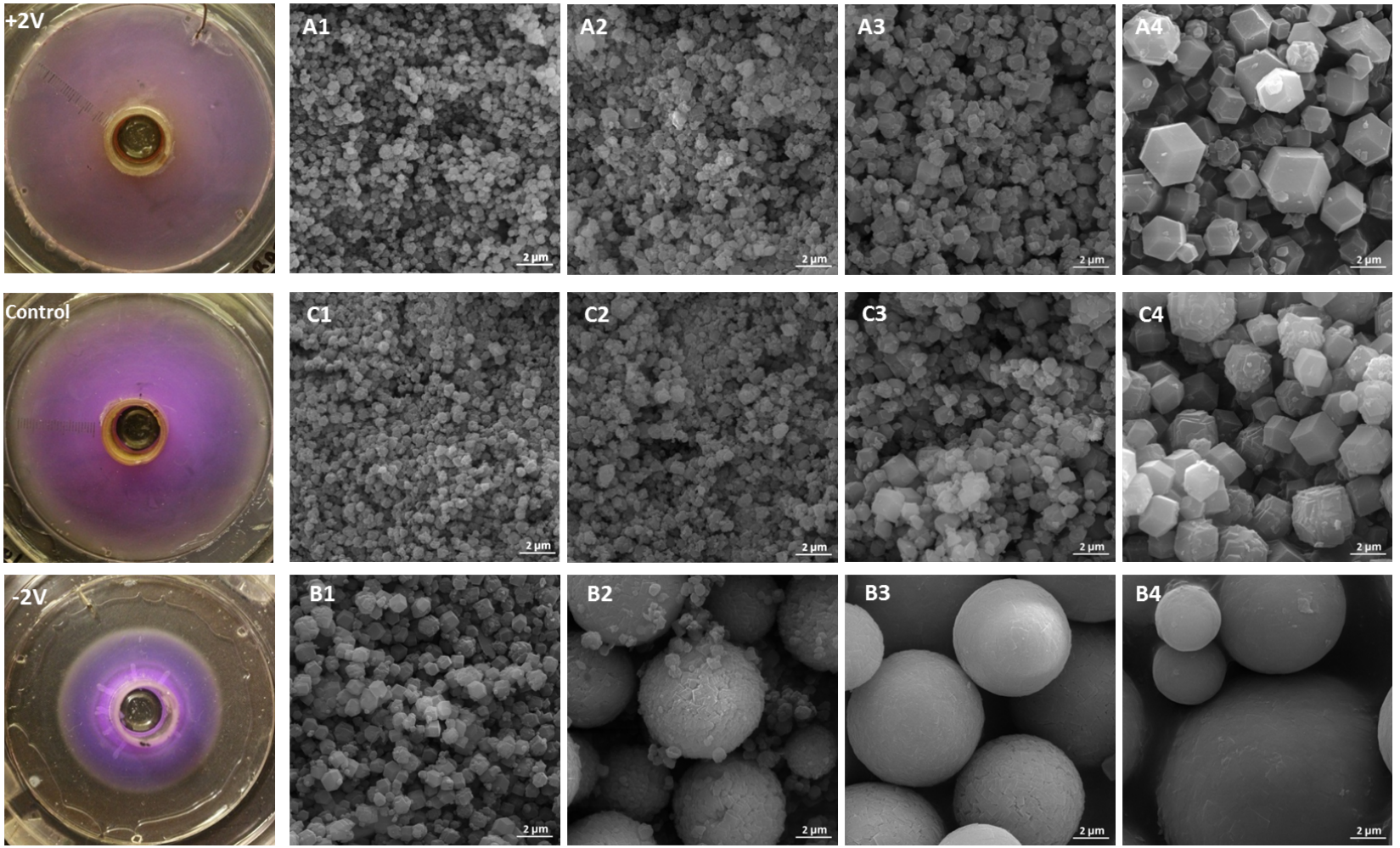

Figure A.20: Images of the three plates in the 1^{st} run of the multiple-batch repeatability study. The system is Zn-Co mixed-metal ZIF-8 using 25% Co precursor solutions and nitrate salts. The samples are collected as 0.5 cm "bands".

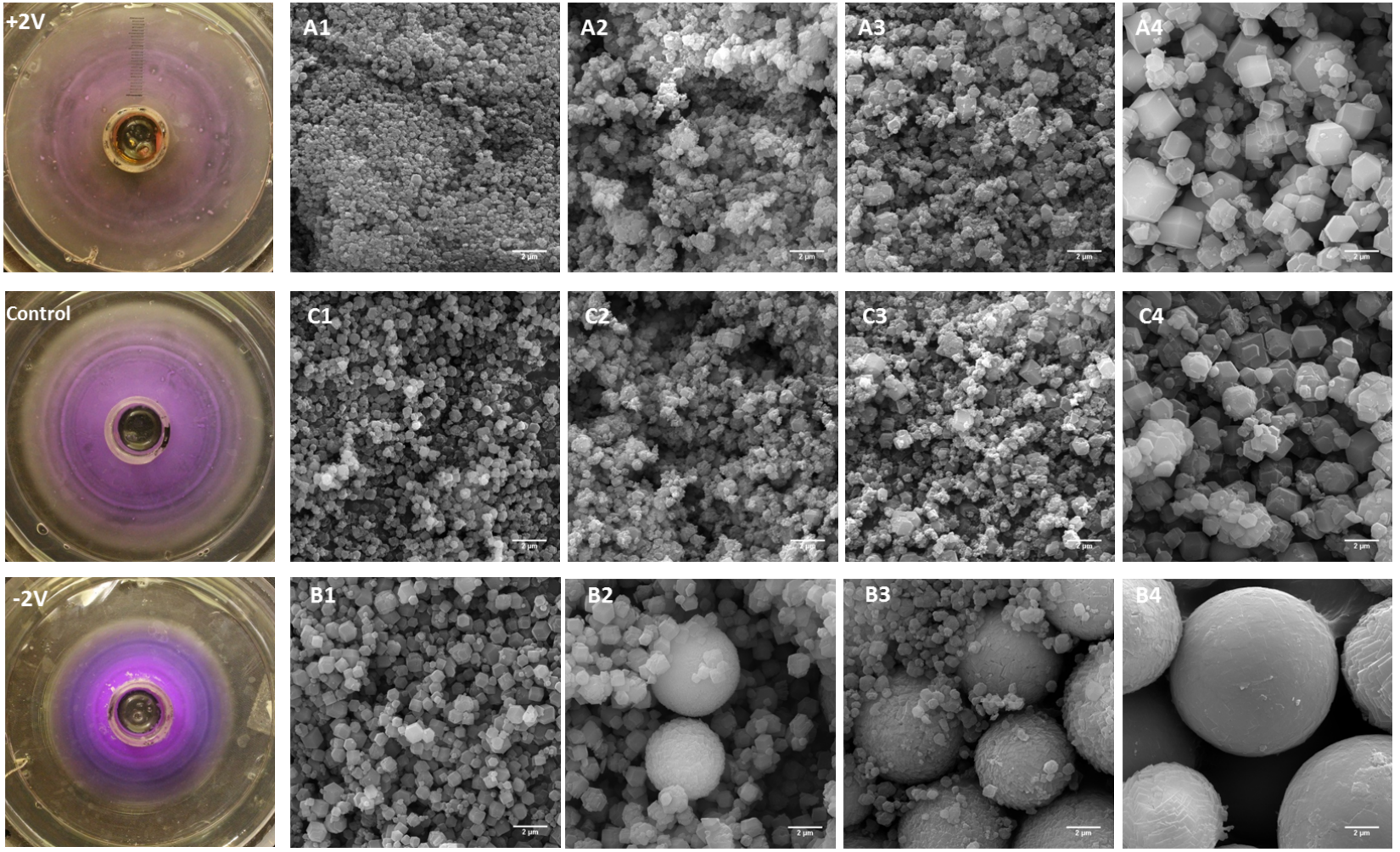

Figure A.21: Images of the three plates in the 2^{nd} run of the multiple-batch repeatability study. The system is Zn-Co mixed-metal ZIF-8 using 25% Co precursor solutions and nitrate salts. The samples are collected as 0.5 cm "bands".

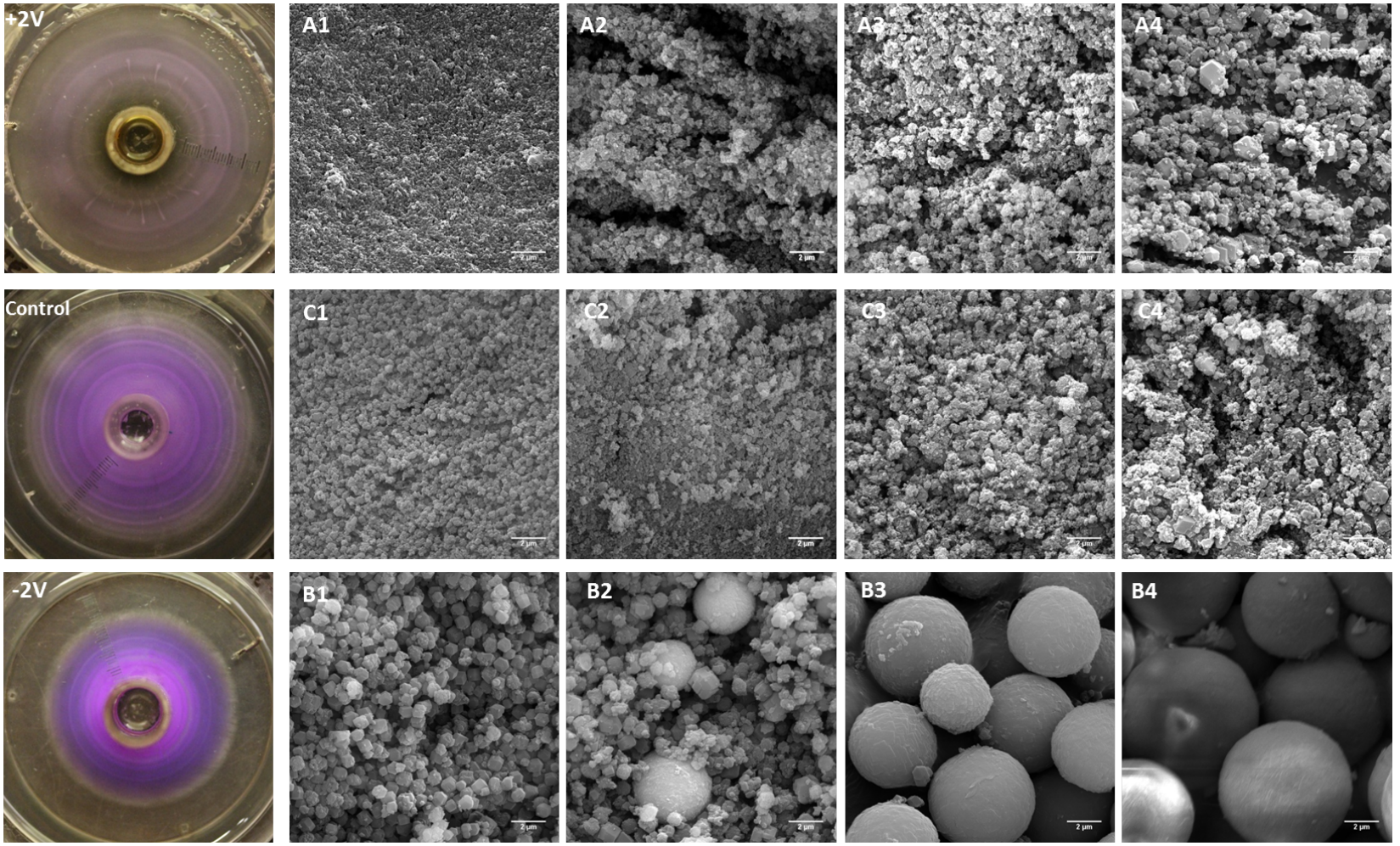

Figure A.22: Images of the three plates in the 3^{rd} run of the multiple-batch repeatability study. The system is Zn-Co mixed-metal ZIF-8 using 25% Co precursor solutions and nitrate salts. The samples are collected as 0.5 cm "bands".

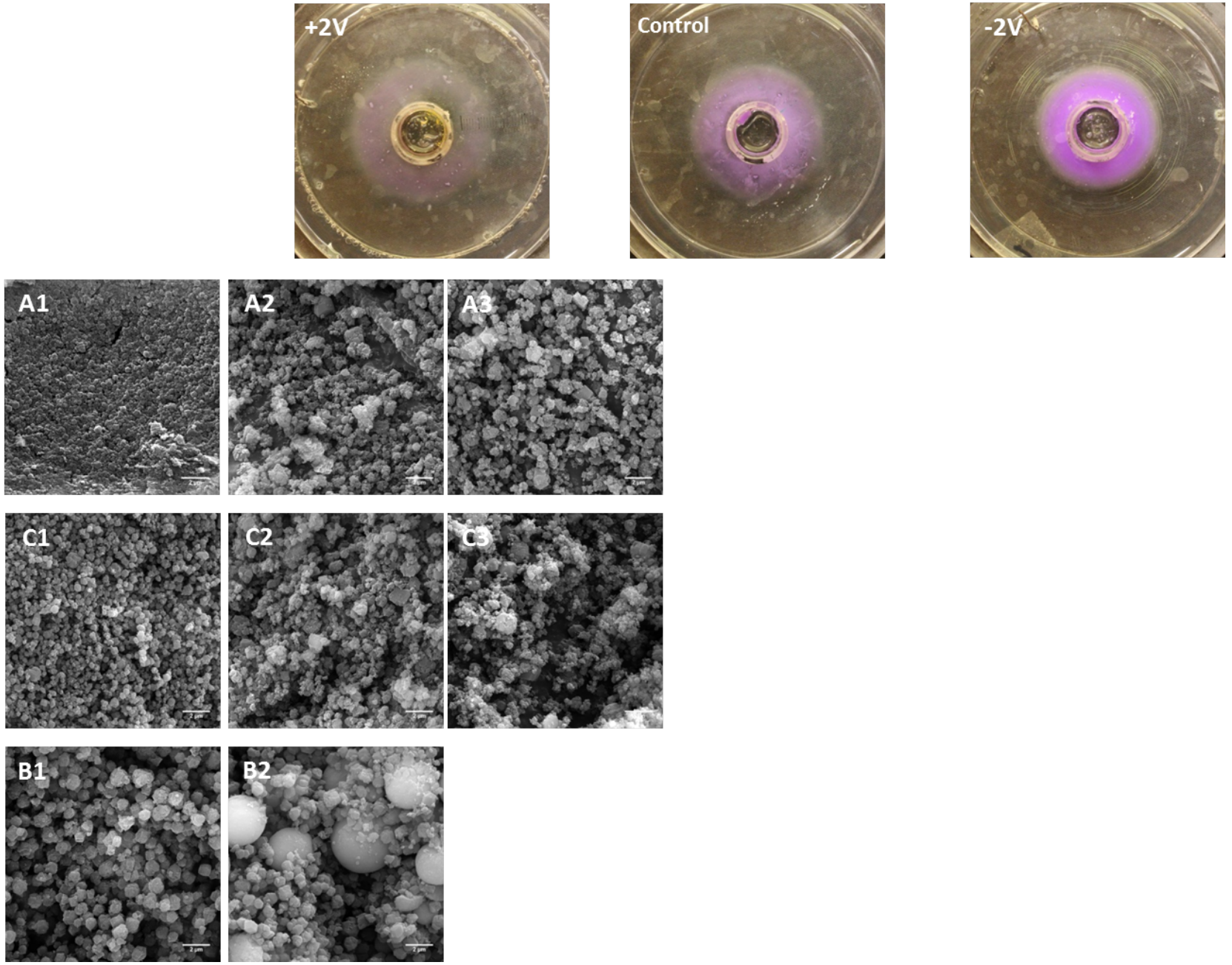

Figure A.23: Images of the three plates in the 1^{st} day of the time study. The system is Zn-Co mixed-metal ZIF-8 using 25% Co precursor solutions and nitrate salts. The samples are collected as 0.5 cm "bands".

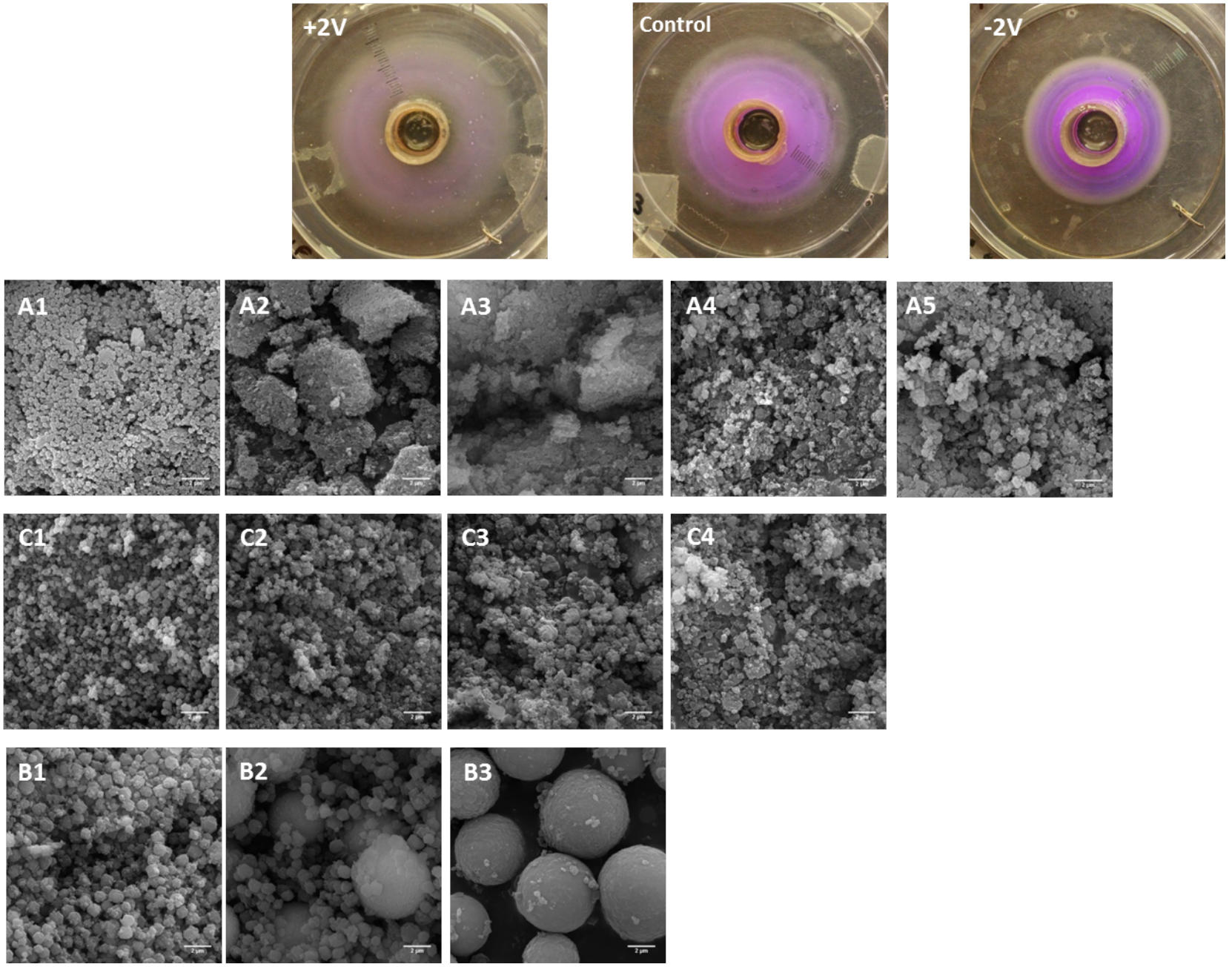

Figure A.24: Images of the three plates in the 2^{nd} day of the time study. Zn-Co mixed-metal ZIF-8 system using 25% Co precursor solutions and nitrate salts. The samples are collected as 0.5 cm "bands".

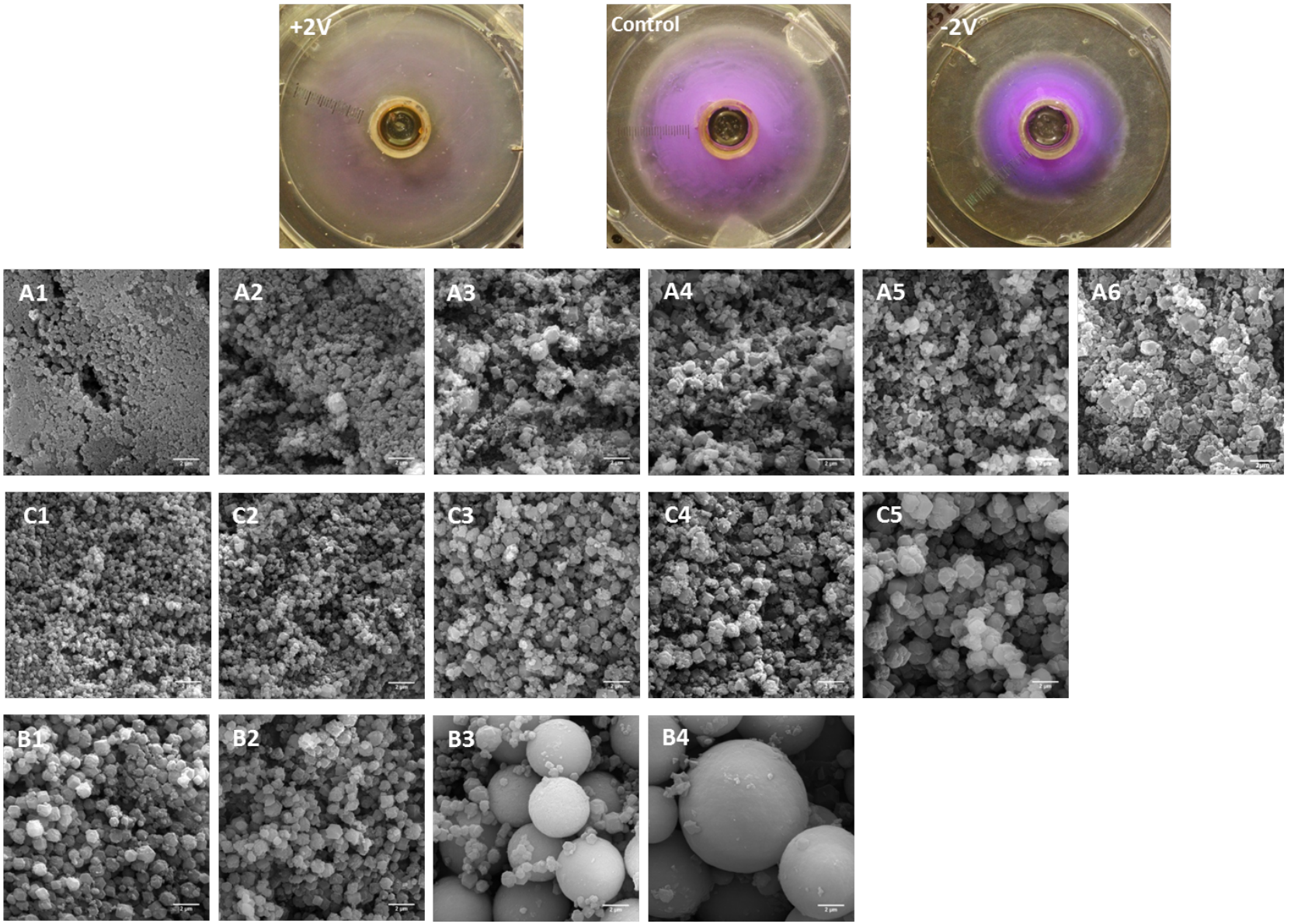

Figure A.25: Images of the three plates in the 3^{rd} day of the time study. The system is Zn-Co mixed-metal ZIF-8 using 25% Co precursor solutions and nitrate salts. The samples are collected as 0.5 cm "bands".

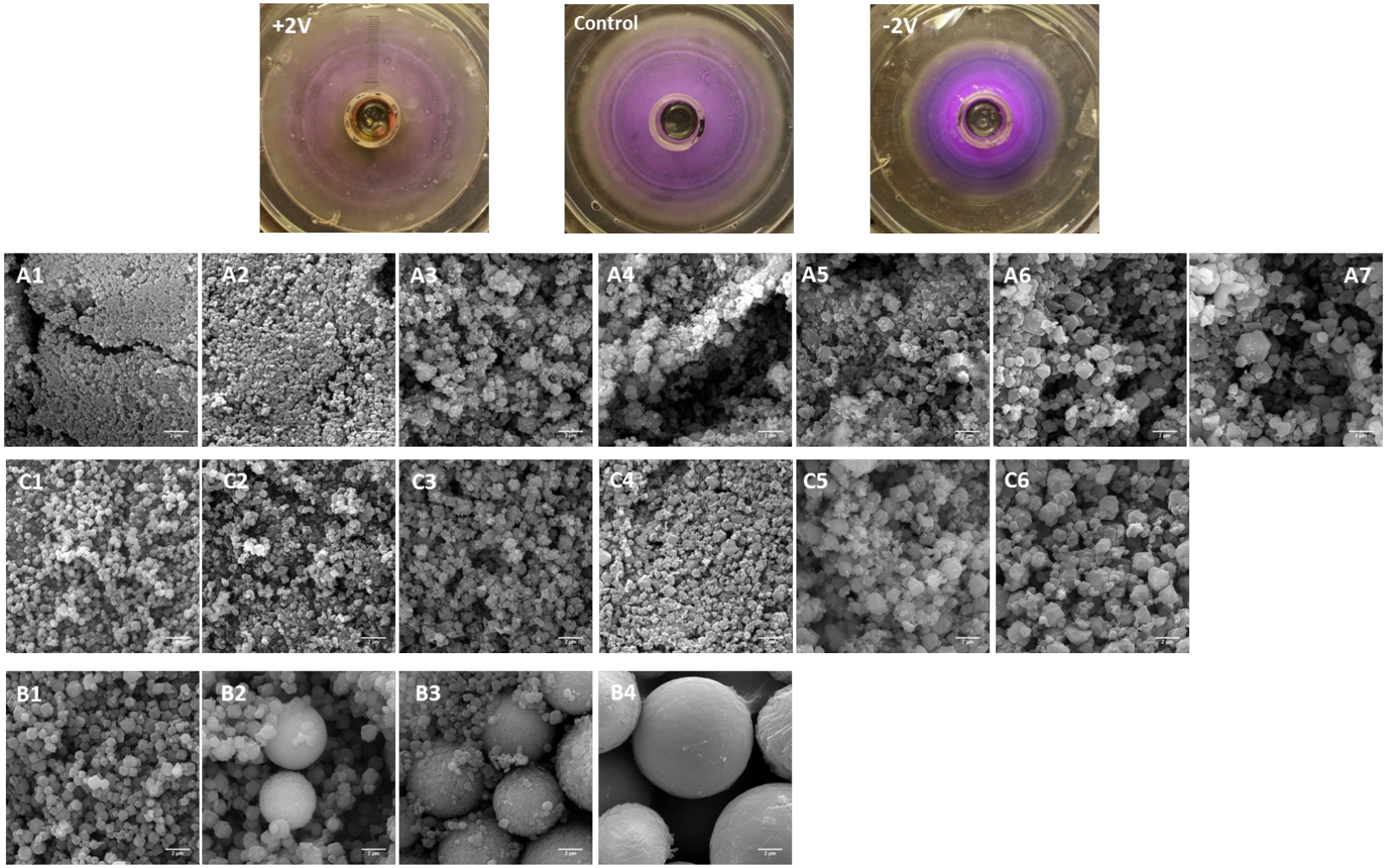

Figure A.26: Images of the three plates in the 4^{th} day of the time study. The system is Zn-Co mixed-metal ZIF-8 using 25% Co precursor solutions and nitrate salts. The samples are collected as 0.5 cm "bands".

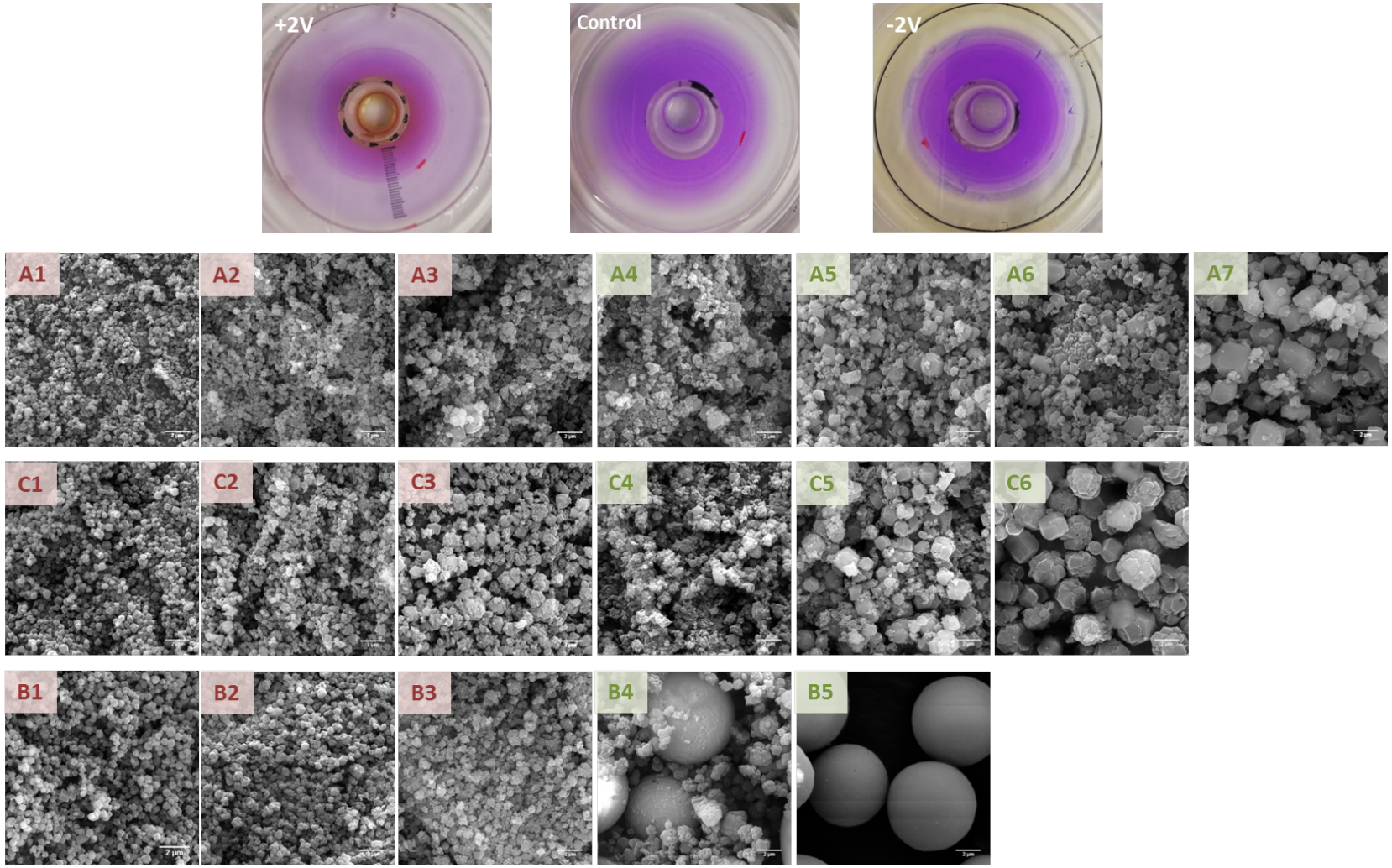

Figure A.27: Images of the three plates that were subjected to an electric field for four days after two days of reaction-diffusion. The system is Zn-Co mixed-metal ZIF-8 using 25% Co precursor solutions and nitrate salts. The samples are collected as 0.5 cm "bands". Samples labeled in red precipitated before the application of an external electric field, and those labeled in green precipitated after.

Appendix B

PXRD Patterns

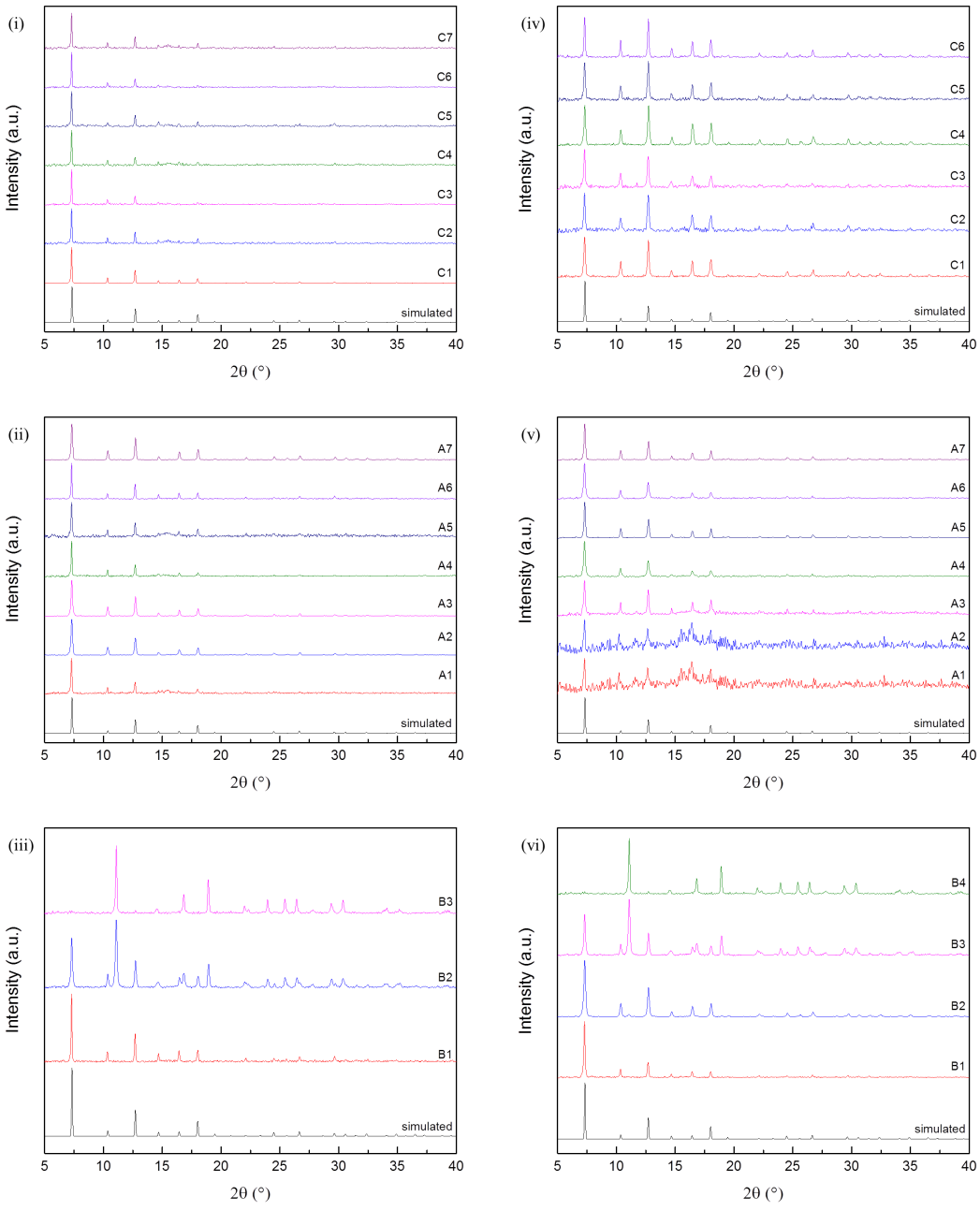

Figure B.1: PXRD patterns for ZIF-8 using sulfate salts (i, ii, iii - first column) and nitrate salts (iv, v, vi - second column) collected using the 0.5cm band method. C stands for control (first row), A stands for +2V (second row), and B stands for -2V (third row).

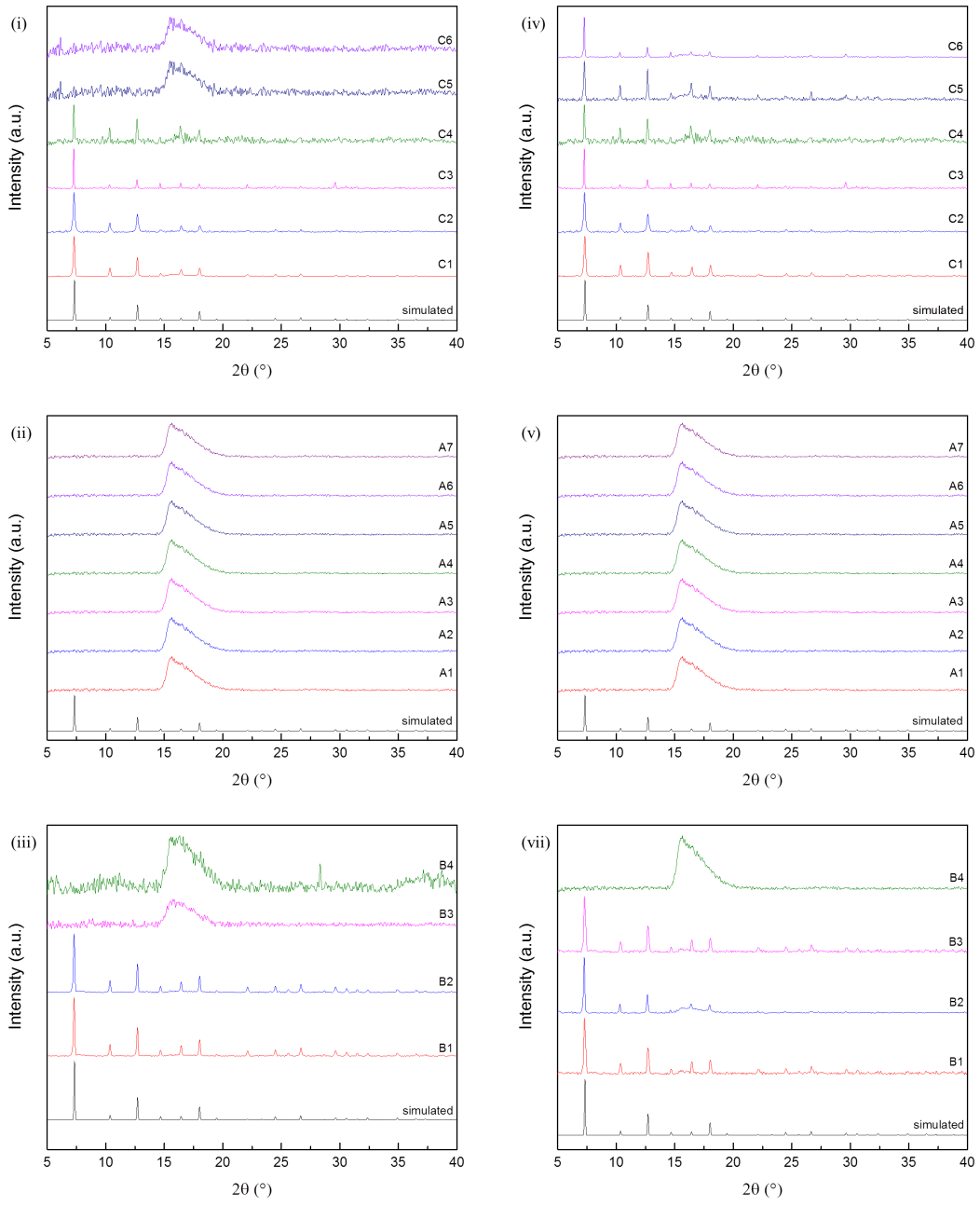

Figure B.2: PXRD patterns for ZIF-67 using sulfate salts (i, ii, iii - first column) and nitrate salts (iv, v, vi - second column) collected using the 0.5cm band method. C stands for control (first row), A stands for +2V (second row), and B stands for -2V (third row). The wide peak from 15 °till about 20 °is that of the background, which indicates that the samples are amorphous.

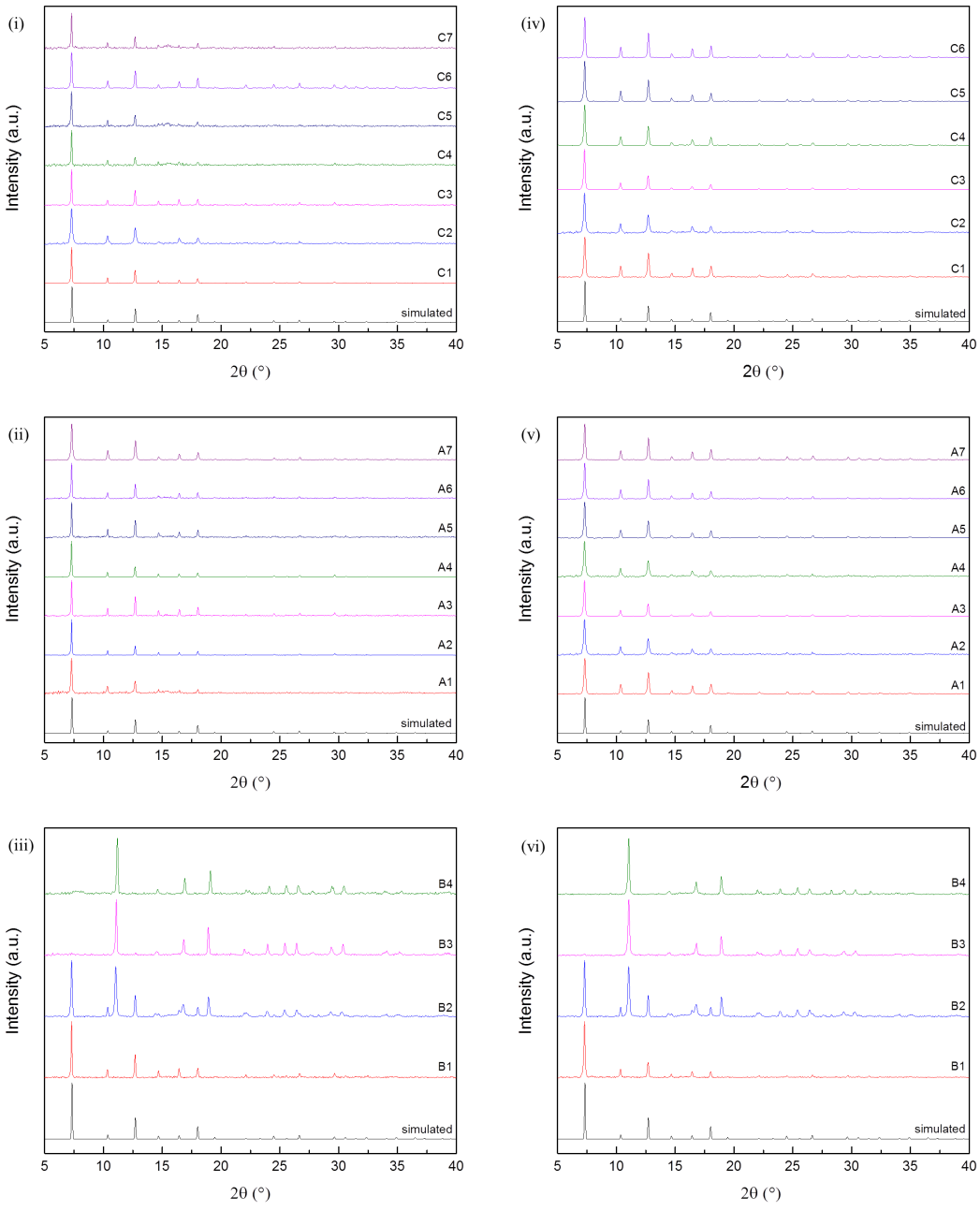

Figure B.3: PXRD patterns for Zn-Co mixed-metal ZIF-8 using sulfate salts (i, ii, iii - first column) and nitrate salts (iv, v, vi - second column) collected using the 0.5cm band method. C stands for control (first row), A stands for +2V (second row), and B stands for -2V (third row).

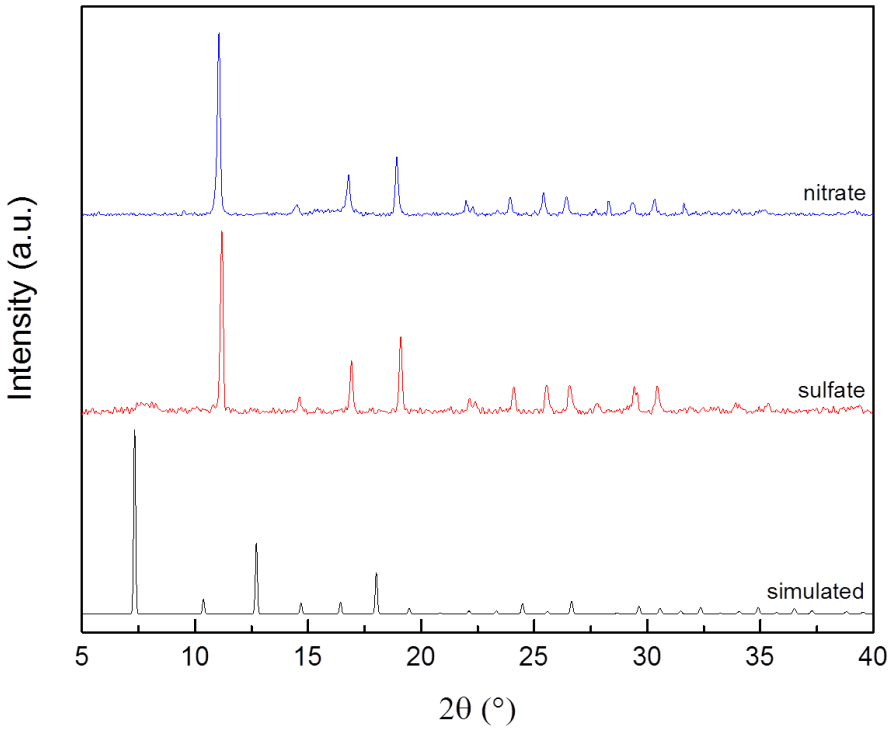

Figure B.4: PXRD patterns for the spherical co-precipitate that starts to appear in the second band of reactors subjected to -2V.

Bibliography

[1] I. R. Epstein and K. Showalter, "Nonlinear chemical dynamics: oscillations, patterns, and chaos," *The Journal of Physcial Chemistry*, vol. 100, pp. 12132–12147, 1996.

[2] I. R. Epstein, J. A. Pojman, and O. Steinbock, "Introduction: Self-organization in nonequilibrium chemical systems," *Chaos*, vol. 16, p. 037101, 2006.

[3] T. Antal, M. Droz, J. Magnin, Z. Rácz, and M. Zrinyi, "Derivation of the Matalon-Packter law for Liesegang patterns," *The Journal of Chemical Physics*, vol. 109, pp. 9479–9488, 1998.

[4] K. H. Stern, "The liesegang phenomenon," *ACS publications*, 1953.

[5] R. E. Liesegang, "Ueber einige eigenschaften von gallerten," *Naturwissenschaftliche Wochenschrift*, vol. 11, no. 30, pp. 353–362, 1896.

[6] W. Ostwald, *Lehrbuch der allgemeinen chemie*. W. Engelmann Leipzig, 1897.

[7] B. A. Grzybowski, *Chemistry in Motion: Reaction-Diffusion Systems for Micro- and Nanotechnology*. Wiley: West Sussex, 2009.

[8] S. LeDuc, *Théorie physico-chimique de la vie et générations spontanées.* Poinat, 1910.

[9] S. Sadek and R. sultan, "Liesegang patterns in nature: A diverse scenery across the sciences," *Precipitation Patterns in Reaction-Diffusion Systems*, vol. 1, pp. 1–43, 2010.

[10] K. Jablczynski, "Memoires presentes à la société chimique. Les anneaux de Liesegang," *Bulletin Société Chimie de France*, vol. 33, pp. 1592–1602, 1923.

[11] P. B. Mathur, "A diffusion mechanism for Liesegang rings. I. Spacing law," *Bulletin of the Chemical Society of Japan*, vol. 34, no. 3, pp. 437–440, 1961.

[12] R. Matalon and A. Packter, "The liesegang phenomenon. i. sol protection and diffusion," *Journal of Colloid Science*, vol. 10, no. 1, pp. 46–62, 1955.

[13] M. Droz, J. Magnin, and M. Zrinyi, "Liesegang patterns : Studies on the width law," *The Journal of Chemical Physics*, vol. 110, no. 19, p. 9618, 1999.

[14] H. Morse and G. Pierce, "Diffusion and supersaturation in gelatine," *Proceedings of the American Academy of Arts and Sciences*, vol. 38, no. 22, pp. 625–648, 1903.

[15] C. Wagner, "Mathematical analysis of the formation of periodic precipitations," *Journal of Colloid Science*, vol. 5, no. 1, pp. 85–97, 1950.

[16] S. Prager, "Periodic precipitation," *The Journal of Chemical Physics*, vol. 25, no. 2, pp. 279–283, 1956.

[17] Y. B. Zeldovich, G. Barenblatt, and R. Salganik, " On the quasiperiodic precipitation of sediment under mutual diffusion of two substances (Liesegang rings)," *Doklady, USSR Academy of Sciences*, vol. 140, no. 6, pp. 1281–1284, 1961.

[18] J. D. Murray, *Mathematical Biology: I. An Introduction*. Springer, third ed., 2002.

[19] S. K. Smoukov, I. Lagzi, and B. A. Grzybowski, " Independence of primary and secondary structures in periodic precipitation patterns," *The Journal of Physical Chemistry Letters*, vol. 2, no. 4, pp. 345–349, 2011.

[20] M. Flicker and J. Ross, " Mechanism of chemical instability for periodic precipitation phenomena," *The Journal of Chemical Physics*, vol. 60, no. 9, pp. 3458–3465, 1974.

[21] J. Ross, "Two topics in chemical instabilities: I periodic precipitation processes; ii resonances in oscillatory reactions and glycolysis," in *Nonlinear Phenomena in Chemical Dynamics* (C. Vidal and A. Pacault, eds.), (Berlin, Heidelberg), pp. 180–185, Springer Berlin Heidelberg, 1981.

[22] R. Sultan, "Propagating fronts in periodic precipitation systems with redissolution," *Physical Chemistry Chemical Physics*, vol. 4, no. 8, pp. 1253–1261, 2002.

[23] D. Feinn, P. Ortoleva, W. Scalf, S. Schmidt, and M. Wolff, "Spontaneous pattern formation in precipitating systems," *The Journal of Chemical Physics*, vol. 69, no. 1, pp. 27–39, 1978.

[24] S. Kai, S. C. Muller, and J. Ross, "Measurements of temporal and spatial sequences of events in periodic precipitation processes," *The Journal of Chemical Physics*, vol. 76, no. 3, pp. 1392–1406, 1982.

[25] H. K. Henisch, *Periodic precipitation: A microcomputer analysis of transport and reaction processes in diffusion media with software development.* Pergamon Press, 1991.

[26] D. S. Chernavskii, A. A. Polezhaev, and S. C. Muller, "A model of pattern formation by precipitation," *Physica D: Nonlinear Phenomena*, vol. 54, pp. 160–170, 1991.

[27] A. A. Polezhaev and S. C. Muller, "Complexity of precipitation patterns: Comparison of simulation with experiment," *Chaos: An Interdisciplinary Journal of Nonlinear Science*, vol. 4, no. 4, pp. 631–636, 1994.

[28] C. V. Raman and K. S. Ramaiah, "The wave-like character of periodic precipitates," *Proceedings of the Indian Academy of Science Section A*, vol. 9A, pp. 455–466, 1939.

[29] A. Volford, F. Izsak, M. Ripszam, and I. Lagzi, "Pattern formation and self organization in a simple precipitation system," *Langmuir*, vol. 23, no. 3, pp. 961–964, 2007.

[30] M. Dayeh, "Experimental and theoretical investigation of the transition from bands to 2d squares/hexagons and 3d turing patterns in the cadmium sulfide precipitation reaction-diffusion system," Master's thesis, American University of Beirut Faculty of Arts and Sciences Department of Chemistry, 2014.

[31] R. Zakhia Al Douaihy, M. Al-Ghoul, and M. Hmadeh, "Liesegang banding for controlled size and growth of zeolitic-imidazolate frameworks," *Small*, vol. 15, 05 2019.

[32] T. Isemura, "Studies of rhythmic precipitates.," *Bulletin of the Chemical Society of Japan*, vol. 14, pp. 179–237, 1939.

[33] M. A. Han, S. H. Jun, and Y. Kang, "Effect of electrolyte on the shapes of liesegang rings," *Journal of the Korean Chemical Society*, vol. 52, p. 356, 2008.

[34] S. Veil, *Les périodicites de structure.* Hermann, 1934.

[35] S. Y. Reigh, "Effect of an external electric field on the diffusion-influenced geminate reversible reaction of a neutral particle and a charged particle in three dimensions. iii. ground-state abcd reaction.," *The Journal of Chemical Physics*, vol. 139, no. 19, p. 194107, 2013.

[36] S. Dutta and D. S. Ray, "Effects of delay in a reaction-diffusion system under the influence of an electric field.," *Physical Review E, statistical nonlinear and soft matter physics*, vol. 77, no. 3.2, p. 36202, 2008.

[37] Z. Shreif, L. Mandalian, A. Abi-Haydar, and R. Sulta, "Taming ring morphology in 2d co(oh)2 liesegang patterns.," *Physical Chemistry Chemical Physics*, vol. 6, no. 13, pp. 3461–3466, 2004.

[38] I. Lagzi and F. Izsak, "Stochastic description of precipitate pattern formation in an electric field," *Physical Chemistry Chemical Physics*, vol. 5, pp. 4144–4148, 2003.

[39] I. Lagzi, "Formation of liesegang patterns in an electric field," *Physical Chemistry Chemical Physics*, vol. 4, no. 8, pp. 1269–1270, 2002.

[40] I. Bena, M. Droz, and Z. Rácz, "Formation of liesegang patterns in the presence of an electric field.," *The Journal of Chemical Physics*, vol. 122, p. 204502, 2005.

[41] R. Sultan and R. Halabieh, "Effect of an electric field on propagating co(oh)2 liesegang patterns.," *Chemical Physics Letters*, vol. 332, no. 32, pp. 331–338, 2000.

[42] M. Al-Ghoul and R. Sultan, "Front propagation in patterned precipitation. 2. electric effects in precipitation-dissolution patterning schemes.," *The Journal of Physical Chemistry A*, vol. 107, no. 8, pp. 81095–1101, 2003.

[43] I. Das, A. Pushkarna, and A. Bhattacharjee, "New results on light-induced spatial bifurcation and electrical field effect on chemical waves in the mercury(ii)chloridepotassium iodide system in gel media.," *The Journal of Physical Chemistry*, vol. 94, no. 26, pp. 8968–8973, 1990.

[44] A. P. S. Selvadurai, *Partial differential equations in mechanics 2: the biharmonic equation, Poisson's equation*. Springer, 2000.

[45] M. E. Davis, "Ordered porous materials for engineering applications," *Nature*, vol. 417, pp. 813–821, 2002.

[46] M. Eddaoudi, J. Kim, N. Rosi, D. Vodak, J. Watcher, M. O'Keeffe, and O. M. Yaghi, "Systematic design of pore size and functionality in isoreticular mofs and their application in methane storage," *science*, vol. 295, pp. 469–472, 2002.

[47] J. Y. Ying, C. P. Mehnert, and M. S. Wong, "Synthesis and applications of supramolecular templated mesoporous materials," *Angewandte Chemie International Edition*, vol. 38, pp. 56–77, 2004.

[48] K. S. Sing, "Reporting physisorption data for gas/solid systems with special reference to the determination of surface area and porosity," *Pure and Applied Chemistry*, vol. 57, pp. 603–619, 1985.

[49] S. R. Batten, B. F. Hoskins, and R. Robson, "Two interpenetrating 3d networks which generate spacious sealed-off compartments enclosing of the

order of 20 solvent molecules in the structures of zn(cn)(no3)," *Journal of the American Chemical Society*, vol. 117, pp. 5385–5386, 1995.

[50] B. F. Hoskins and R. Robson, "Design and construction of a new class of scaffolding-like materials comprising infinite polymeric frameworks of 3d-linked molecular rods. a reappraisal of the zinc cyanide and cadmium cyanide structures and the synthesis and structure of the diamond-related frameworks," *Journal of the American Chemical Society*, vol. 112, no. 4, pp. 1546–1554, 1990.

[51] S. Kitagawa, S. Kawata, Y. Nozaka, and M. Munakata, "Synthesis and crystal structures of novel copper(i) co-ordination polymers and a hexa-copper(i) cluster of quinoline-2-thione," *Journal of the Chemical Society, Dalton Transactions*, pp. 1399–1404, 1993.

[52] S. Kitagawa, S. Matsuyama, M. Munakata, and T. Emori, "Synthesis and crystal structures of novel one-dimensional polymers," *Journal of the Chemical Society, Dalton Transactions*, pp. 2869–2874, 1991.

[53] O. M. Yaghi and H. L. Li, "Hydrothermal synthesis of a metal-organic framework containing large rectangular channels," *Journal of the American Chemical Society*, pp. 10401–10402, 1995.

[54] G. B. Gardner, D. Venkataramani, J. S. Moore, and S. Lee, "Spontaneous assembly of a hinged coordination network," *Nature*, pp. 792–795, 1995.

[55] D. Riou and G. Ferey, "Hybrid open frameworks (mil-n). part 3 crystal structures of the ht and lt forms of mil-7: a new vanadium propylenediphosphonate with an open-framework. influence of the synthesis temperature on the oxidation state of vanadium within the same structural type," *The Journal of Material Chemistry*, vol. 8, pp. 2733–2735, 1998.

[56] M. P. Yan, *Crystal growth of the metal-organic framework ZIF-8*. PhD thesis, The University of Manchester, Faculty of Engineering and Physical Sciences, 2012.

[57] C. Wang, D. Liu, and W. Lin, "Metal-organic frameworks as a tunable platform for designing functional molecular materials," *Journal of the American Chemical Scociety*, vol. 135, pp. 13222–13234, 2013.

[58] M. O'Keeffe, M. A. Peskov, S. J. Ramsden, and O. M. Yaghi, "The reticular chemistry structure resource (rcsr) database of, and symbols for, crystal nets," *Accounts of chemical research*, vol. 41, no. 12, pp. 1782–1789, 2008.

[59] O. M. Yaghi, M. O'Keeffe, N. W. Ockwig, H. K. Chae, M. Eddaoudi, and J. Kim, "Reticular synthesis and the design of new materials," *Nature*, vol. 432, pp. 705–714, 2003.

[60] P. Deria, J. E. Mondloch, O. Karagiaridi, W. Bury, J. T. Hupp, and O. K. Farha, "Beyond post-synthesis modification: evolution of metal-organic frameworks via building block replacement," *Chemical society reviews*, vol. 43, no. 16, pp. 5896–5912, 2017.

[61] A. Phan, C. J. Doonan, F. J. Uribe-Romo, C. B. Knobler, M. O'Keefe, and O. M. Yaghi, "Synthesis, structure, and carbon dioxide capture properties of zeolitic imidazolate frameworks," *Accounts of Chemical Research*, vol. 43, no. 1, pp. 58–67, 2010.

[62] K. S. Park, Z. Ni, A. P. Côté, J. Y. Choi, R. Huang, F. J. Uribe-Rmom, H. K. Chae, M. O'Keeffe, and O. M. Yaghi, "Exceptional chemical and thermal stability of zeolitic imidazolate frameworks," *Proeedings of the National Academy of Sciences of the U.S.A.*, vol. 103, no. 27, pp. 10186–10191, 2006.

[63] B. Wang, A. P. Côté, H. Furukawa, M. O'Keeffe, and O. M. Yaghi, "Colossal cages in zeolitic imidazolate frameworks as selective carbon dioxide reservoirs," *Nature*, vol. 453, pp. 453–207, 2008.

[64] H. Hayashi, A. P. Côté, H. Furukawa, M. O'Keeffe, and O. M. Yaghi, "Zeolite a imidazolate frameworks," *Nature Materials*, vol. 6, pp. 501–506, 2007.

[65] R. Banerjee, A. Phan, B. Wang, C. Kobler, H. Furukawa, M. O'Keeffe, and O. M. Yaghi, "High-throughput synthesis of zeolitic imidazolate frameworks and application to co_2 capture," *Science*, vol. 316, pp. 939–943, 2008.

[66] A. Schejn, A. Aboulaich, L. Balan, V. Falk, J. Lalevée, G. Medjahdi, L. Aranda, K. Mozet, and R. Schneider, "Cu^{2+}-doped zeolitic imidazolate frameworks (zif-8): efficient and stable catalysts for cycloadditions and condensation reactions," *Catalysis Science and Technology*, vol. 5, no. 3, pp. 1829–1839, 2015.

[67] X. C. Huang, Y. Y. Lin, J. P. Zhang, and X. M. Chen, "Ligand-directed strategy for zeolite-type metal-organic frameworks: zinc(ii) imidazolates with unusual zeolitic topologies," *Angewandte Chemie International Edition*, vol. 45, no. 10, pp. 1557–1559, 2006.

[68] Y. Li, F. Liang, H. Bux, W. Yang, and J. Caro, "Zeolitic imidazolate framework zif-7 based molecular sieve membrane for hydrogen separation," *Journal of Membrane Science*, vol. 354, pp. 48–54, 2010.

[69] U. P. Tran, K. K. Le, and N. T. Phan, "Expanding applations of metal-organic frameworks: zeolitic imidazolate framework zif-8 as and efficient heterogeneous catalys for the knoevenagel reaction," *ACS Catalysis*, vol. 1, no. 2, pp. 120–127, 2011.

[70] S. R. Venna and M. A. Carreon, "Highly permeable zeolite imidazolate framework-8 membranes for co_2/ch_4 separation," *Journal of the American Chemical Society*, vol. 132, no. 1, pp. 76–78, 2009.

[71] S. A. Moggach, T. D. Bennett, and A. K. Cheetham, "The effect of pressure on zif-8: Increasing pore size with pressure and the formation of a high-pressure phase at 1.47 gpa," *Angewandte Chemie*, vol. 121, no. 38, pp. 7221–7223, 2009.

[72] D. Fairen-Jimenez, S. A. Moggach, M. T. Wharmby, P. A. Wright, S. Parsons, and T. Duren, "Opening the gate: Framework flexibility in zif-8 explored by experiments and simulations," *Journal of the American Chemical Society*, vol. 133, pp. 8900–8902, 2011.

[73] J. L. Tatarko, *The production, properties and applications of the zinc imidazolate, ZIF-8.* PhD thesis, The University of Louisville, 2015.

[74] Y. Ban, Y. Li, X. Liu, Y. Peng, and W. Yang, "Solvothermal synthesis of mixed-ligand metal-organic framework zif-78 with controllable size and morphology," *Microporous and Mesoporous Materials*, vol. 173, pp. 29–36, 2013.

[75] T. Yang and T. S. Chung, "Room-temperature synthesis of zif-90 nanocrystals and the derived nano-composite membranes for hydrogen separation," *Journal of Materials Chemistry A*, vol. 1, pp. 6081–6090, 2013.

[76] D. Peralta, G. Chaplais, A. Simon-Masseron, K. Barthelet, and G. D. Pirngruber, "Synthesis and adsorption properties of zif-76 isomorphs," *Microporous and Mesoporous Materials*, vol. 153, pp. 1–7, 2012.

[77] J. Cravillon, S. Munzer, S. Lohmeier, A. Feldhoff, K. Huber, and M. Wiebcke, "Rapid room-temperature synthesis and characterization of nanocrystals of a prototypical zeolitic imidazolate framework," *Chemistry of Materials*, vol. 21, pp. 1410–1412, 2009.

[78] S. Nune, P. Thallapally, A. Dohnalkova, C. Wang, J. Liu, and G. Exarhos, "Synthesis and properties of nano zeolitic imidazolate frameworks," *Chemical Communications*, vol. 46, pp. 4878–4880, 2010.

[79] J. Cravillon, R. Nayuk, S. Springer, A. Feldhoff, K. Huber, and M. Wiebcke, "Controlling zeolitic imidazolate framework nano and microcrystal formation: insight into crystal growth by time-resolved in situ static light scattering," *Chemistry of Materials*, vol. 23, pp. 2130–2141, 2011.

[80] C. S. Cundy and P. A. Cox, "The hydrothermal synthesis of zeolites: history and development from the earliest days to the present time," *Chemical Reviews*, vol. 103, pp. 663–702, 2003.

[81] C. S. Cundy and P. A. Cox, "The hydrothermal synthesis of zeolites: Precursors, intermediates and reaction mechanism," *Microporous Mesoporous Materials*, vol. 82, pp. 1–78, 2005.

[82] G. Ferey, "Hybrid porous solids: past, present, future," *Chemical Society Reviews*, vol. 37, pp. 191–214, 2008.

[83] P. M. Forster, N. Stock, and A. K. Cheetham, "A high-throughput investigation of the role of ph, temperature, concentration, and time on the synthesis of hybrid inorganic-organic materials," *Angewandte Chemie International Edition*, vol. 44, pp. 7608–7611, 2005.

[84] Y. Pan, Y. Liu, G. Zeng, L. Zhao, and Z. Lai, "Rapid synthesis of zeolitic imidazolate framework-8 nanocrystals in an aqueous system," *Chemical Communications*, vol. 47, pp. 2071–2073, 2011.

[85] A. F. Gross, E. Sherman, and J. J. Vajo, "Aqueous room temperature synthesis of cobalt and zinc sodalite zeolitic imidizolate frameworks," *Dalton Transactions*, vol. 41, pp. 5458–5460, 2012.

[86] J. Yao, M. He, K. Wang, R. Chen, Z. Zhong, and H. Wang, "High-yield synthesis of zeolitic imidazolate frameworks from stoichiometric metal and ligand precursor aqueous solutions at room temperature," *CrystEngComm*, vol. 15, pp. 3601–3606, 2013.

[87] F. Shieh, S. Wang, S. Leo, and K. C. W. Wu, "Water-based synthesis of zeolitic imidazolate framework-90 with a controllable particle size," *Chemistry A European Journal*, vol. 19, pp. 11139–11142, 2013.

[88] B. Chen, F. Bai, Y. Zhu, and Y. Xia, "A cost-effective method for the synthesis of zeolitic imidazolate framework-8 materials from stoichiometric precursors via aqueous ammonia modulation at room temperature," *Microporous and Mesoporous Materials*, vol. 193, pp. 7–14, 2014.

[89] E. R. Cooper, C. D. Andrews, P. S. Wheatley, P. B. Webb, P. Wormald, and R. E. Morris, "Ionic liquids and eutectic mixtures as solvent and template in synthesis of zeolite analogues," *Nature*, vol. 430, pp. 1012–1016, 2004.

[90] E. R. Parnham and R. E. Morris, "Ionothermal synthesis of zeolites, metal-organic frameworks, and inorganic-organic hybrids," *Accounts of Chemical Research*, vol. 40, pp. 1005–1013, 2007.

[91] B. Seoane, J. M. Zamaro, C. Téllez, and J. Coronas, "Insight into the crystal synthesis, activation and application of zif-20," *RSC Advances*, vol. 1, pp. 917–922, 2011.

[92] R. Rosa, C. Ponzoni, and C. Leonelli, "Direct energy supply to the reaction mixture during microwave-assisted hydrothermal and combustion synthesis of inorganic materials," *Inorganics*, vol. 2, pp. 191–210, 2014.

[93] B. Seoane, S. Castellanos, A. Dikhtiarenko, F. Kapteijn, and J. Gascon, "Multi-scale crystal engineering of metal-organic frameworks," *Coordination Chemistry Reviews*, vol. 307, pp. 147–187, 2016.

[94] J. H. Park, S. H. Park, and S. H. Jhung, "Microwave-syntheses of zeolitic imidazolate framework material, zif-8," *Journal of the Korean Chemical Society*, vol. 53, p. 553, 2009.

[95] A. Gedanken, "Using sonochemistry for the fabrication of nanomaterials," *Ultrasonics Sonochemistry*, vol. 11, pp. 47–55, 2004.

[96] K. S. Suslick, D. A. Hammerton, and R. E. Cline, "Sonochemical hot spot," *Journal of the Americn Chemical Society*, vol. 108, pp. 5641–5642, 1986.

[97] B. Seoane, J. M. Zamaro, C. Tellez, and J. Coronas, "Sonocrystallization of zeolitic imidazolate frameworks (zif-7, zif-8, zif-11 and zif-20)," *CrystEngComm*, vol. 14, pp. 3103–3107, 2012.

[98] A. Abou-Hassan, O. Sandre, and V. Cabuil, "Microfluidics in inorganic chemistry," *Angewandte Chemie International Edition*, vol. 49, no. 36, pp. 6268–6286, 2010.

[99] R. Ameloot, F. Vermoortele, W. Vanhove, M. Roeffaers, B. F. Sels, and D. E. De-Vos, "Interfacial synthesis of hollow metal-organic framework capsules demonstrating selective permeability," *Nature Chemistry*, vol. 3, no. 5, pp. 382–387, 2011.

[100] J. Puigmarti-Luis, M. Rubio-Martinez, U. Hartfelder, I. Imaz, D. Maspoch, and P. S. Dittrich, "Coordination polymer nanofibers generated by microfluidic synthesis," *Journal of the American Chemical Society*, vol. 133, no. 12, pp. 4216–4219, 2011.

[101] J. Puigmart-Luis, M. Rubio-Martinez, I. Imaz, B. Z. Cvetkovic, L. Abad, A. Perez del Pino, D. Maspoch, and D. B. Amabilino, "Localized, stepwise template growth of functional nanowires from an amino acid-supported framework in a microfluidic chip," *ACS nano*, vol. 8, no. 1, pp. 818–826, 2013.

[102] M. Faustini, J. Kim, G. Y. Jeong, J. Y. Kim, H. R. Moon, W. S. Ahn, and D. P. Kim, "Microfluidic approach toward continuous and ultrafast synthesis of metal-organic framework crystals and hetero structures in confined microdroplets," *Journal of the American Chemical Society*, vol. 135, no. 39, pp. 14619–14626, 2013.

[103] L. Paseta, B. Seoane, D. Julve, V. Sebastian, C. Tellez, and J. Coronas, "Accelerating the controlled synthesis of metal-organic frameworks by a microfluidic approach: a nanoliter continuous reactor," *ACS applied materials and interfaces*, vol. 5, no. 19, pp. 9405–9410, 2013.

[104] D. Yamamoto, T. Maki, S. Watanabe, H. Tanaka, M. T. Miyahara, and K. Mae, "Synthesis and adsorption properties of zif-8 nanoparticles using a micromixer," *Chemical engineering Journal*, vol. 227, pp. 145–150, 2013.

[105] BASF, U. Muller, H. Putter, M. Hesse, H. Wessel, M. Schubert, J. Huff, and M. Guzmann, "Method for electrochemical production of a crystaline porous metal organic skeleton material." Patent (WO2005049892), 2005.

[106] R. Ameloot, L. Stappers, J. Fransaer, L. Alaerts, B. F. Sels, and D. E. De-Vos, "Patterned growth of metal-organic framework coatings by electrochemical synthesis," *Chemistry of Materials*, vol. 21, no. 13, pp. 2580–2582, 2009.

[107] A. M. Joaristi, J. Juan-Alcani, P. Serra-Crespo, F. Kapteijn, and J. Gascon, "Electrochemical synthesis of some archetypical zn2+, cu2+, and al3+ metal organic frameworks," *Crystal Growth and Design*, vol. 12, no. 7, pp. 3489–3498, 2012.

[108] M. Klimakow, P. Klobes, A. Thunemann, K. Rademann, and F. Emmerling, "Mechanochemical synthesis of metal-organic frameworks: A fast and facile approach toward quantitative yields and high specific surface areas," *Chemistry of Materials*, vol. 22, pp. 5216–5221, 2010.

[109] A. Pichon, A. Lazuen-Garaya, and S. L. James, "Solvent-free synthesis of a microporous metal-organic framework," *CrystEngComm*, vol. 8, pp. 211–214, 2006.

[110] S. Tanaka, K. Kida, T. Nagaoka, T. Otaa, and Y. Miyake, "Mechanochemical dry conversion of zinc oxide to zeolitic imidazolate framework," *Chemical Communictions*, vol. 49, pp. 7884–7886, 2013.

[111] P. J. Beldon, L. Fabian, R. Stein, A. Thirumurugan, A. Cheetham, and T. Friscic, "Rapid room-temperature synthesis of zeolitic imidazolate frameworks by using mechanochemistry," *Angewandte Chemie International Edition*, vol. 49, pp. 9640–9643, 2010.

[112] Z. Xin, X. Chen, Q. Wang, Q. Chen, and Q. Zhang, "Nanopolyhedrons and mesoporous supra-structures of zeolitic imidazolate framework with high adsorption performance," *Microporous and Mesoporous Materials*, vol. 169, pp. 218–221, 2013.

[113] R. Issa and M. Hmadeh, "Synthesis and structural evolution of metal-organic frameworks by reaction-diffusion process at room temperature,"

Master's thesis, American University of Beirut Faculty of Arts and Sciences Department of Chemistry, 2017.

[114] D. Saliba, M. Ammar, M. Rammal, M. Al-Ghoul, and M. Hmadeh, "Crystal growth of zif-8, zif-67, and their mixed-metal derivatives," *J. Am. Chem. Soc.*, vol. 140, pp. 1812–1823, 2018.

[115] M. P. Attfield and P. Cubillas, "Crystal growth of nanoporous metal-organic frameworks," *Dalton Transactions*, vol. 41, pp. 3968–3878, 2012.

[116] G. Dhanaraj, K. Byrappa, V. Prasad, and M. Dudley, *Springer Handbook of Crystal Growth*. springer, 2010.

[117] G. R. Desiraju, J. J. Vittal, and A. Ramanan, *Crystal Engineering: A Textbook*. World Scientific, 2011.

[118] I. Sunagawa, *Crystals: Growth, Morphoology, Perfection*, ch. 3. Cambridge University Press, 2005.

[119] H. J. Lee, W. Cho, and M. Oh, "Fluorescent octahedron and rounded-octahedron coordination polymer particles," *CrystEngComm*, vol. 12, pp. 3959–3963, 2010.

[120] S. Jung and M. Oh, "Monitoring shape transformation from nanowires to nanocubes and size-controlled formation of coordination polymer particles," *Angewandte Chemie International Edition*, vol. 47, pp. 2049–2051, 2008.

[121] X. Cheng, A. Zhang, K. Hou, M. Liu, Y. Wang, C. Song, G. Zhang, and X. Guo, "Size and morphology controlled nh2-mil-53(al) prepared in dmf-water mixed solvents," *Dalton Transactions*, vol. 42, pp. 13698–13705, 2013.

[122] T. Chalati, P. Horcajada, R. Gref, P. Couvreur, and C. Serre, "Optimisation of the synthesis of mof nanoparticles made of flexible porous iron fumarate mil-88a," *Journal of Materials Chemistry*, vol. 21, pp. 2220–2227, 2011.

[123] X. Zhang, M. A. Ballem, M. Ahrén, A. Suska, P. Bergman, and K. Uvdal, "Nanoscale ln(iii)-carboxylate coordination polymers: temperature-controlled guest encapsulation and light harvesting," *Journal of the American Chemical Socitety*, vol. 132, pp. 10391–10397, 2010.

[124] K. Liu, Y. Zheng, G. Jia, M. Yang, Y. Huang, and H. You, "Facile synthesis of hierarchically superstructured praseodymium benzenetricarboxylate with controllable morphologies," *CrystEngComm*, vol. 13, pp. 452–458, 2011.

[125] E. H. Ryu, J. H. Lee, Y. S. Lee, J. M. Gu, S. Huh, and S. J. Lee, "Size-controlled cubic coordination polymer nanoparticles from chiral dipyridyl zn-salen," *Inorganic Chemistry Communications*, vol. 14, pp. 1648–1651, 2011.

[126] K. Wang, Z. Geng, M. Zheng, L. Ma, X. Ma, and Z. Wang, "Controllable fabrication of coordination polymer particles: A bridge between versatile organic building blocks and porous copper-based inorganic materials," *Crystal Growth and Design*, vol. 12, pp. 5606–5614, 2012.

[127] K. E. deKrafft, Z. Xie, G. Cao, S. Tran, L. Ma, O. Z. Zhou, and W. Lin, "Iodinated nanoscale coordination polymers as potential contrast agents for computed tomography," *Angewandte Chemie International Edition*, vol. 48, pp. 9901–9904, 2009.

[128] K. Liu, H. You, Y. Zheng, G. Jia, Y. Huang, M. Yang, Y. Song, L. Zhang, and H. Zhang, "Room-temperature synthesis of multi-morphological coordination polymer and tunable white-light emission," *Crystal Growth and Design*, vol. 10, pp. 16–19, 2010.

[129] K. Liu, Y. Zheng, G. Jia, M. Yang, Y. Song, N. Guo, and H. You, "Nano micro-scaled la(1,3,5-btc)(h2o)6 coordination polymer: Facile morphology-controlled fabrication and color-tunable photoluminescence properties by co-doping eu3+,tb3+," *Journal of Solid State Chemistry*, vol. 183, pp. 2309–2316, 2010.

[130] M. Gustafsson and X. Zou, "Crystal formation and size control of zeolitic imidazolate frameworks with mixed imidazolate linkers," *Journal of Porous Materials*, vol. 20, pp. 55–63, 2013.

[131] S. Shankar, R. Balgley, M. Lahav, S. R. Cohen, R. Popovitz-Biro, and M. E. van der Boom, "Metal-organic microstructures: From rectangular to stellated and interpenetrating polyhedra," *Journal of the American Chemical Society*, vol. 137, no. 1, pp. 226–231, 2015.

[132] C. Li, X. Yin, L. Chen, Q. Li, and T. Wang, "Synthesis of cobalt ion-based coordination polymer nanowires and their conversion into porous co3o4 nanowires with good lithium storage properties," *Chemistry - A European Journal*, vol. 16, pp. 5215–5221, 2010.

[133] W. Zhongchun, E. L. Leslie, W. Weishi, J. M. Craig, E. M. James, and A. S. John, "Monodisperse porphyrin nanospheres synthesized by coordination polymerization," *Nanotechnology*, vol. 19, pp. 395604–395610, 2008.

[134] X. Li, F. Cheng, S. Zhang, and J. Chen, "Shape-controlled synthesis and lithium-storage study of metal-organic frameworks zn4o (1,3,5-benzenetribenzoate) 2," *Journal of Power Sources*, vol. 160, pp. 542–547, 2006.

[135] G. Lu and J. T. Hupp, "Metal-organic frameworks as sensors: A zif-8 based fabry-perot device as a selective sensor for chemical vapors and gases,"

Journal of the American Chemical Society, vol. 132, no. 23, pp. 7832–7833, 2010.

[136] W. Ma, Q. Jiang, P. Yu, L. Yang, and L. Mao, "Zeolitic imidazolate framework-based electrochemical biosensor for in vivo electrochemical measurements," *Analytical Chemistry*, vol. 85, no. 15, pp. 7550–7557, 2013.

[137] S. Liu, Z. Xiang, Z. Hu, Z. Zheng, and D. Cao, "Zeolitic imidazolate framework-8 as a luminescent material for the sensing of metal ions and small molecules," *Journal of Materials Chemistry*, vol. 21, no. 18, pp. 6649–6653, 2011.

[138] S. Liu, L. Wang, J. Tian, Y. Luo, G. Chang, A. M. Asiri, A. O. Alyoubi, and X. Sun, "Application of zeolitic imidazolate frameworkâĂŘ8 nanoparticles for the fluorescence-enhanced detection of nucleic acids," *ChemPlusChem*, vol. 77, no. 1, pp. 23–26, 2011.

[139] S. Eslava, L. Zhang, S. Esconjauregui, J. Yang, K. Vanstreels, M. R. Baklanov, and E. Saiz, "Metal-organic framework zif-8 films as low-k dielectrics in microelectronics," *Chemistry of Materials*, vol. 25, no. 1, pp. 27–33, 2013.

[140] M. Law, L. E. Greene, J. C. Johnson, R. Saykally, and P. Yang, "Nanowire dyesensitized solar cells," *Nature Mat*, vol. 4, pp. 455–459, 2005.

[141] C.-Y. Sun, C. Qin, X.-L. Wang, G.-S. Yang, K.-Z. Shao, Y.-Q. Lan, Z.-M. Su, P. Huang, C.-G. Wanga, and E.-B. Wanga, "Zeolitic imidazolate framework-8 as efficient ph-sensitive drug delivery vehicle," *Dalton Transactions*, vol. 41, no. 23, pp. 6906–6909, 2012.

[142] I. B. Vasconcelos, T. G. d. Silva, G. C. G. Militao, T. A. Soares, N. M. Rodrigues, M. O. Rodrigues, N. B. d. Costa, R. O. Freire, and S. A. Junior, "Cytotoxicity and slow release of the anti-cancer drug doxorubicin from zif-8," *RSC Adv*, vol. 2, p. 9437, 2012.

[143] H. Ren, L. Zhang, J. An, T. Wang, L. Li, X. Si, L. He, X. Wu, C. Wang, and Z. Su, "Polyacrylic acid@zeolitic imidazolate framework-8 nanoparticles with ultrahigh drug loading capability for ph-sensitive drug release," *Chemical Communications*, vol. 50, no. 8, pp. 1000–1002, 2014.

[144] S. Bhattacharjee, M. S. Jang, H. J. Kwon, and W. S. Ahn, "Zeolitic imidazolate frameworks: Synthesis, functionalization,and catalytic/adsorption applications," *Catalysis Surveys from Asia*, vol. 18, no. 4, pp. 101–127, 2014.

[145] J. McEwen, J. D. Hayman, and A. O. Yazaydin, "A comparative study of co2, ch4 and n2 adsorption in zif-8, zeolite-13x and bpl activated carbon," *Chemical Physics*, vol. 412, pp. 72–76, 2013.

[146] S. I. Garces, J. Villarroel-Rocha, K. Sapag, S. A. Korili, and A. Gil, "Comparative study of the adsorption equilibrium of co2 on microporous commercial materials at low pressures," *Industrial and Engineering Chemistry Research*, vol. 52, pp. 6785–6793, 2013.

[147] H. Wu, W. Zhou, and T. Yildirim, "Hydrogen storage in a prototypical zeolitic imidazolate framework-8," *Journal of the American Chemical Society*, vol. 129, no. 17, pp. 5314–5315, 2007.

[148] H. Wu, W. Zhou, and T. Yildirim, "Methane sorption in nanoporous metal-organic frameworks and first-order phase transition of confined methane," *The Journal of Physical Chemistry C*, vol. 113, pp. 3029–3035, 2009.

[149] J. Perez-Pellitero, H. Amrouche, F. R. Siperstein, G. Pirngruber, C. Nieto-Draghi, G. Chaplais, A. Simon-Masseron, D. Bazer-Bachi, D. Peralta, and N. Bats, "Adsorption of co2, ch4, and n2 on zeolitic imidazolate frameworks: Experiments and simulations," *Chemistry a European Journal*, vol. 16, pp. 1560–1571, 2010.

[150] M. Zhou, Q. Wang, L. Zhang, Y. C. Liu, and Y. Kang, "Adsorption sites of hydrogen in zeolitic imidazolate frameworks," *The Journal of Physical Chemistry B*, vol. 113, pp. 11049–11053, 2009.

[151] Y. Liu, H. L. Liu, Y. Hu, and J. W. Jiang, "Development of a density functional theory in three-dimensional nanoconfined space: H2 storage in metal-organic frameworks," *The Journal of Physical Chemistry B*, vol. 113, pp. 12326–12331, 2009.

[152] B. Assfour, S. Leoni, and G. Seifert, "Hydrogen adsorption sites in zeolite imidazolate frameworks zif-8 and zif-11," *The Journal of Physical Chemistry C*, vol. 114, pp. 13381–13384, 2010.

[153] R. Banerjee, H. Furukawa, D. Britt, C. Knobler, M. O'Keeffe, and O. M. Yaghi, "Control of pore size and functionality in isoreticular zeolitic imidazolate frameworks and their carbon dioxide selective capture properties," *The Journal of the American Chemical Society*, vol. 131, pp. 3875–3877, 2009.

[154] H. Amrouche, S. Aguado, J. Perez-Pellitero, C. Chizallet, F. Siperstein, D. Farrusseng, N. Bats, and C. Nieto-Draghi, "Experimental and computational study of functionality impact on sodalite-zeolitic imidazolate frameworks for co_2 separation," *The Journal of Physical Chemistry C*, vol. 115, pp. 16425–16432, 2011.

[155] J. A. Thompson, N. A. Brunelli, R. P. Lively, J. R. Johnson, C. W. Jones, and S. Nair, "Tunable co2 adsorbents by mixed-linker synthesis and post-

synthetic modification of zeolitic imidazolate frameworks," *The Journal of Physical Chemistry C*, vol. 117, pp. 8198–8207, 2013.

[156] F. C. U.S. Department of Energy, Hydrogen and I. T. Program, "Multi-year research, development and demonstration plan," 2011.

[157] N. Chang, Z. Y. Gu, and X. P. Yan, "Zeolitic imidazolate framework-8 nanocrystal coated capillary for molecular sieving of branched alkanes from linear alkanes along with high-resolution chromatographic separation of linear alkanes," *Journal of the American Chemical Society*, vol. 132, pp. 13645–13647, 2010.

[158] J. Li, Y. Wu, Z. Li, B. Zhang, M. Zhu, X. Hu, Y. Zhang, and F. Li, "Zeolitic imidazolate framework-8with high efficiency in trace arsenate adsorption and removal from water," *The Journal of Physical Chemistry C*, vol. 118, no. 47, pp. 27382–27387, 2014.

[159] M. Jian, B. Liu, G. Zhang, R. Liu, and X. Zhang, "Adsorptive removal of arsenic from aqueous solution by zeolitic imidazolate framewok -8 nanoparticles," *Colloids and Surfaces A: Physicochemical and Engineering Aspects*, vol. 465, pp. 67–76, 2015.

[160] B. K. Jung, J. W. Jun, Z. Hasan, and S. HwaJhung, "Adsorptive removal of p-arsanilic acid from water using mesoporous zeolitic imidazolate framework-8," *Chemical Engineering Journal*, vol. 267, pp. 9–15, 2015.

[161] M. N. Shaharak, M. Ghahramaninezhad, and M. Eydifarash, "Zeolitic imidazolate framework-8 for efficient adsorption and removal of cr (vi) ions from aqueous solution," *Environmental Science and Pollution Research*, vol. 24, no. 10, pp. 9625–9634, 2017.

[162] K. Lin and H. A. Chang, "Efficient adsorptive removal of humic acid from waer using zeolitic imidazolate framework-8," *Water, Air, and Soil Pollution*, vol. 226, no. 2, p. 10, 2015.

[163] N. A. Khan, B. K. Jung, and S. H. Jhung, "Adsorption and removal of phthalic acid and diethyl phthalate from water with zeolitic imidazolate and metal-organic frameworks," *Journal of Hazardous Materials*, vol. 282, pp. 194–200, 2015.

[164] X. Yan, Y. Yang, C. Wang, X. Hu, M. Zhou, and S. Komarneni, "Surfactant-assisted synthesis of zif-8 nanocrystal for phthalic acid adsorption," *Journal of Sol-Gl Science and Technology*, vol. 80, no. 2, pp. 523–530, 2016.

[165] J. Q. Jiang, C. X. Yang, and X. P. Yan, "Zeolitic imidazolate framework-8 for fast asorption and removal of benzotriazoles from aqueous solution," *ACS Applied Materials and Interfaces*, vol. 5, no. 19, pp. 9837–9842, 2013.

[166] E. E. Sanna, Y. Pana, Z. Gaoa, S. Zhana, and F. Xiaa, "Highly hydrophobic zif-8 particles and application for oil-water separation," *Separation and Purification Technology*, vol. 206, pp. 186–191, 2018.

[167] Y. Li, K. Zhou, M. He, and J. Yao, "Synthesis of zif-8 and zif-67 using mixed-base and their dye adsorption," *Microporous and Mesoporous Materials*, vol. 234, pp. 287–292, 2016.

[168] Y. Feng, Y. Li, M. Xu, S. Liu, and J. Yao, "Fast adsorption of methyl blue on zeolitic imidazolate framework-8 and its adsorption mechanism," *RSC Advances*, vol. 6, no. 111, pp. 109608–109612, 2016.

[169] M. T. Thanh, T. V. Thien, V. T. T. Chau, P. D. Du, N. P. Hung, and D. Q. Khieu, "Synthesis of iron-doped zeolitic imidazolate framework-8 and its remasol deep lack rgb bye adsorption ability," *Journal of Chemistry*, no. 5045973, 2017.

[170] J. Abdi, M. Vossoughi, and N. M. M. anf I Alwmzadeh, "Synthesis of amine-modified zeolitic imidazolate framework-8: ultrasound-assisted dye removal and modeling," *Ultrasonics Sonochemistry*, vol. 39, pp. 550–564, 2017.

[171] P. K. Thallapally, C. A. Fernandez, R. K. Motkuri, S. K. Nune, J. Liub, and C. H. F. Pedenb, "Micro and mesoporous metal-organic frameworks for catalysis applications," *Dalton Transactions*, vol. 39, pp. 1692–1694, 2010.

[172] H. Y. Cho, J. Kim, S. N. Kim, and W. S. Ahn, "High yield 1-l scale synthesis of zif-8 via a sonochemical route," *Microporous and Mesoporous Materials*, vol. 169, pp. 180–184, 2013.

[173] T. Zhang, X. Zhang, X. Yan, L. Kong, G. Zhang, H. Liu, J. Qiu, and K. L. Yeung, "Synthesis of fe3o4@ zif-8 magnetic core-shell microspheres and their potential application in a capillary microreactor," *Chemical Engineering Journal*, vol. 228, pp. 398–404, 2013.

[174] R. Jin, Z. Bian, J. Li, M. Ding, and L. Gao, "Zif-8 crystal coatings on a polyimide substrate and their catalytic behaviours for the knoevenagel reaction," *Dalton Transactions*, vol. 42, pp. 3936–3940, 2013.

[175] C. M. Miralda, E. E. Macias, M. Zhu, P. Ratnasamy, and M. A. Carreon, "Zeolitic imidazole framework-8 catalysts in the conversion of co2 to chloropropene carbonate," *ACS Catalysis*, vol. 2, no. 1, pp. 180–183, 2012.

[176] J. Kim, S. N. Kim, H. G. Jang, G. Seo, and W. S. Ahn, "Co2 cycloaddition of styrene oxide over mof catalysts," *Applied Catalysis A: General*, vol. 453, pp. 175–180, 2013.

[177] M. Zhu, D. Srinivas, S. Bhogeswararao, Ratnasamy, and M. A. Carreon, "Catalytic activity of zif-8 in the synthesis of styrene carbonate from co2 and styrene oxide," *Catalysis Communications*, vol. 32, pp. 36–40, 2013.

[178] L. T. L. Nguyen, K. K. A. Le, and N. T. S. Phan, "A zeolite imidazolate framework zif-8 catalyst for friedel-crafts acylation," *Chinese Journal of Catalysis*, vol. 33, pp. 688–696, 2012.

[179] C. Chizallet, S. Lazare, D. Bazer-Bachi, F. Bonnier, V. Lecocq, E. Soyer, A. A. Q. AA, and N. Bats, "Catalysis of transesterification by a nonfunctionalized metal-organic framework: Acido-basicity at the external surface of zif-8 probed by ftir and ab initio calculations," *Journal of the American Chemical Society*, vol. 132, pp. 12365–12377, 2010.

[180] H. L. Jiang, B. Liu, T. Akita, M. Haruta, H. Sakurai, and Q. Xu, "Au@ zif-8: Co oxidation over gold nanoparticles deposited to metal-organic framework," *Journal of the American Chemical Society*, vol. 131, pp. 11302–11303, 2009.

[181] W. X. Wang, Y. W. Li, R. J. Zhang, D. H. He, H. L. Liu, and S. J. Liao, "Metal-organic framework as a host for synthesis of nanoscale co3o4 as an active catalyst for co oxidation," *Catalysis Communications*, vol. 12, pp. 875–879, 2011.

[182] D. Esken, S. Turner, O. I. Lebedev, G. V. Tendeloo, and R. A. Fischer, "Au@ zifs: stabilization and encapsulation of cavity-size matching gold clusters inside functionalized zeolite imidazolate frameworks, zifs," *Chemistry of Materials*, vol. 22, pp. 6393–6401, 2010.

[183] T. T. Isimjan, H. Kazemian, S. Rohani, and A. K. Ray, "Photocatalytic activities of pt/zif-8 loaded highly ordered tio_2 nanotubes," *Journal of Materials Chemistry*, vol. 20, pp. 10241–10245, 2010.

[184] M. B. J. Roeffaers, R. Ameloot, M. Baruah, H. Uji-i, M. Bulut, G. De-Cremer, U. Muller, P. A. Jacobs, J. Hofkens, B. F. Sels, and D. E. De-Vos, "Morphology of large zsm-5 crystals unraveled by fluorescence microscopy," *Journal of the American Chemical Scociety*, vol. 130, pp. 5763–5772, 2008.

[185] R. A. Schoonheydt, "Morphology of and catalysis in single crystals of zeolites," *Angewandte Chemie International Edition*, vol. 47, pp. 9188–9191, 2008.

[186] A. Umemura, S. P. Diring, S. Furukawa, H. Uehara, T. Tsuruoka, and S. Kitagawa, "Morphology design of porous coordination polymer crystals by coordination modulation," *Journal of the American Chemical Society*, vol. 133, pp. 15506–15513, 2011.

[187] Z. Berkovitch-Yellin, "Toward an ab initio derivation of crystal morphology," *Journal of the American Chemical Society*, vol. 107, pp. 8239–8253, 1985.

[188] R. Docherty, G. Clydesdale, K. J. Roberts, and P. Bennema, "Application of bravais-friedel-donnay-harker, attachment energy and ising models to predicting and understanding the morphology of molecular crystals," *Journal of Physics D: Applied Physics*, vol. 24, pp. 89–99, 1991.

[189] D. Zacher, R. Schmid, C. Wöll, and R. A. Fischer, "Application of bravais-friedel-donnay-harker, attachment energy and ising models to predicting and understanding the morphology of molecular crystals," *Angewandte Chemie International Edition*, vol. 50, pp. 176–199, 2011.

[190] N. Yanai, M. Sindoro, J. Yan, and S. Granick, "Electric field-induced assembly of monodisperse polyhedral metalâĹŠorganic framework crystals," *Journal of the American Chemical Society*, vol. 135, pp. 34–37, 2013.

[191] A. Ghoufi, K. Benhamed, L. Boukli-Hacene, and G. Maurin, "Electrically induced breathing of the mil-53(cr) metal-organic framework," *ACS Central Science*, vol. 3, pp. 394–398, 2017.

[192] R. Schmid, "An electric field induced breath for metal-organic frameworks a detailed theoretical study demonstrates a new stimulus to change pore shape and size in mil-53.," *ACS Central Science*, vol. 3, pp. 369–371, 2017.

[193] A. L. Kolesnikov, Y. A. Budkov, J. Mö|llmer, M. G. Kiselev, and R. Gläaser, "Metal-organic framework breathing in electric field: A theoretical study," *The Journal of Physical Chemistry C*, pp. 10333–10338, 2019.

[194] B. Tam and O. Yazaydin, "Design of electric field controlled molecular gates mounted on metal-organic frameworks," *Journal of Materials Chemistry A*, vol. 5, pp. 8690–8696, 2017.

[195] A. Knebel, B. Geppert, K. Volgmann, D. I. Kolokolov, A. G. Stepanov, J. Twiefel, P. Heitjans, D. Volkmer, and J. Caro, "Defibrillation of soft porous metal-organic frameworks with electric fields," *Science*, vol. 358, pp. 347–351, 2017.

[196] S. Namsani and A. O. Yazaydin, "Electric field induced rotation of halogenated organic linkers in isoreticular metal-organic frameworks for nanofluidic applications," *Molecular Systems Design and Engineering*, vol. 3, pp. 951–958, 2018.

[197] K. Zhou, B. Mousavi, Z. Luo, S. P. S. Chaemchuen, and F. Verpoort, "Characterization and properties of zn/co zeolitic imidazolate frameworks vs. zif-8 and zif-67," *Journal of Material Chemistry A*, vol. 5, pp. 952–957, 2017.

[198] V. V.Butova, E. A.Bulanova, V. A.Polyakov, A. A.Guda, A. M.Aboraia, V. V.Shapovalov, H. Y.Zahran, I. S.Yahia, and A. V.Soldatov, "The effect of cobalt content in zn/co-zif-8 on iodine capping properties," *Inorganica Chimica Acta*, vol. 492, no. 24, pp. 18–22, 2019.

[199] M. Jian, B. Liu, R. Liu, J. Qu, H. Wand, and X. Zhang, "Water-based synthesis of zeolitic imidazolate framework-8 with high morphology level at room temperature," *RSC Advances*, vol. 5, no. 60, pp. 48433–48441, 2015.

[200] H. H. Perrin, "Dissociation constants of organic bases in aqueous solution." Supplement, London: International Union of Pure and Applied Chemistry, 1972.

[201] L. Gálfi and Z. Rácz, "Properties of the reaction front in an a+b-c type reaction-diffusion process," *Physical Review A - Atomic, Molecular, and Optical Physics*, vol. 38, no. 6, pp. 3151–3154, 1988.

[202] Q. Shi, Z. Chen, Z. Song, J. Li, and J. Dong, "Synthesis of zif-8 and zif-67 by steam-assisted conversion and an investigation of their tribological behaviors," *Angewandte Chemie International Edition*, vol. 50, no. 3, pp. 672–675, 2011.

[203] B. Chen, F. Bai, Y. Zhu, and Y. Xia, "A cost-effective method for the synthesis of zeolitic imidazolate framework-8 materials from stoichiometric precursors via aqueous ammonia modulation at room temperature," *Microporous and Mesoporous Materials*, vol. 193, pp. 7–14, 2014.

[204] R. Z. Douaihy and M. Hmadeh, "Controlled synthesis and size distribution of zeolitic imidazolate framework crystals via the reaction-diffusion framework," Master's thesis, American University of Beirut Faculty of Arts and Sciences Department of Chemistry, 2018.

[205] G. A. Al-Akhrass, M. Ammar, H. El-Rassy, and M. Al-Ghoul, "Self-assembled lanthanum hydroxide microspheres within a reaction-diffusion framework: synthesis, characterization, control and application," *RSC Advances*, vol. 6, pp. 3433–3439, 2016.

[206] H. Fei, J. F. Cahill, K. A. Prather, and S. M. C. n, "Tandem postsynthetic metal ion and ligand exchange in zeolitic imidazolate frameworks," *Inorganic Chemistry*, vol. 52, pp. 4011–4016, 2013.

[207] J. K. Zareba, M. Nyk, and M. Samoc, "Co/zif-8 heterometallic nanoparticles: Control of nanocrystal size and properties by a mixed-metal approach," *Crystal Growth and Design*, vol. 16, pp. 6419–3425, 2016.

[208] Z. J. Zhou, X. P. Li, Z. Liu, Z. R. Li, X. R. Huang, and C. Sun, "Electric field-driven acid-base chemistry: Proton transfer from acid (hcl) to base

(nh3/h2o)," *The Journal of Physical Chemistry A*, vol. 115, pp. 1418–1422, 2011.

[209] S. N. Eustis, D. Radisic, K. H. Bowen, R. A. Bachorz, M. Haranczyk, G. K. Schenter, and M. Gutowski, "Electron-driven acid-base chemistry: Proton transfer from hydrogen chloride to ammonia," *Science*, vol. 319, no. 5865, pp. 936–939, 2008.